Theses and Dissertations

Summer 2010

Carbon dioxide adsorption on nanomaterials

Pragati Galhotra
University of Iowa

Recommended Citation

Galhotra, Pragati. "Carbon dioxide adsorption on nanomaterials." PhD (Doctor of Philosophy) thesis, University of Iowa, 2010.
http://ir.uiowa.edu/etd/670.

CARBON DIOXIDE ADSORPTION ON NANOMATERIALS

by

Pragati Galhotra

An Abstract

Of a thesis submitted in partial fulfillment of the
requirements for the Doctor of Philosophy degree
in Chemistry in
the Graduate College of
The University of Iowa

July 2010

Thesis Supervisor: Professor Vicki H. Grassian

ABSTRACT

In this study, CO_2 adsorption in the presence and absence of co-adsorbed H_2O was investigated on different nanomaterials including nanocrystalline NaY zeolite (nano NaY), ZnO, MgO and γ-Al_2O_3 nanoparticles as well as mixed phase aluminum nanowhiskers. In the case of nano NaY, FTIR spectra show that a majority of CO_2 adsorbs in the pores of these zeolites in a linear complex with the exchangeable cation. Most interesting is the formation of carbonate and bicarbonate on the external surface of nano NaY zeolites, suggesting unique sites for CO_2 adsorption on the surface of these small nanomaterials. Adsorption of ^{18}O-labeled carbon dioxide and theoretical quantum chemical calculations confirms the assignment of these different species. For aluminum oxyhydroxide nanowhiskers and gamma alumina in the absence of co-adsorbed water, CO_2 reacts with surface hydroxyl groups to yield adsorbed bicarbonate as well as some carbonate. $C^{18}O_2$ adsorption confirms these assignments. In the case of nanoparticulate ZnO, CO_2 adsorption under dry conditions results in formation of carbonate, bicarbonates as well as carboxylates. However, in the presence of co-adsorbed water, only carbonate species is formed. ^{18}O-labeled carbon dioxide adsorption and theoretical quantum chemical calculations confirm the vibrational assignment for these different species. Mixed isotope studies with $H_2^{16}O$ + $C^{18}O_2$ and $H_2^{18}O$ + $C^{16}O_2$ suggest that there is extensive exchange between oxygen in adsorbed water and oxygen atoms in gas-phase carbon dioxide. CO_2 adsorption on MgO surfaces, under dry conditions results in formation of carbonate and bicarbonates. Implications for the use of these nanomaterials in carbon dioxide uptake and storage are discussed.

Abstract Approved: _____

Thesis Supervisor

_____

Title and Department

_____

Date

CARBON DIOXIDE ADSORPTION ON NANOMATERIALS

by

Pragati Galhotra

A thesis submitted in partial fulfillment
of the requirements for the Doctor of
Philosophy degree in Chemistry
in the Graduate College of
The University of Iowa

July 2010

Thesis Supervisor: Professor Vicki H. Grassian

Graduate College
The University of Iowa
Iowa City, Iowa

CERTIFICATE OF APPROVAL

_____

PH.D. THESIS

_____

This is to certify that the Ph.D. thesis of

Pragati Galhotra

has been approved by the Examining Committee
for the thesis requirement for the Doctor of Philosophy
degree in Chemistry at the July 2010 graduation.

Thesis Committee: _____
Vicki H. Grassian, Thesis Supervisor

_____
Sarah C. Larsen

_____
Leonard R. MacGillivray

_____
Edward G. Gillan

_____
Paul D. Kleiber

Dedicated to
My Maternal Grandfather and Grandmother

stories. I still remember his overjoyed eyes when I did a good job. Though he is no longer with us, he would have been proud at this achievement.

My Father - I would like to thank my father, for being there for me always and for encouraging me with the words - "chak de phattey" (Punjabi for "Keep it up!"). These words made me feel like a warrior. I would also like to thank him for moving to a bigger city just for our sake!

My Mother- My mother is my strength and my role model. She helped me in my preliminary steps for getting admission to the PhD program. She trusted my capabilities and let me come to this faraway country to fulfill my dreams. I am also thankful to her for teaching me important lessons of life with her own experience. These lessons are invaluable assets of my life.

My Sister, who I could tease and talk to at any time of the day or night. She was always there for me. In spite of being years younger to me, she would often have her words of wisdom for me. I want to thank her for her patience in listening to me when I would have no one else to confide in.

My Brother, who would call me at midnight, forgetting the time zone difference between India and USA. His teasing and jokes made my tough and lonely times tolerable.

My Maternal Aunt - For being a friend, a guide and for always being supportive.

My Maternal Uncle- For the career guidance whenever it was needed!

Last but not the least; I am thankful to my fiancé and now my husband Gautam Kalita. Not only was PhD my dream, at times I felt it was also his dream to have a PhD in the family. I am thankful to him for being supportive, patient and caring. My words cannot express the appreciation for the unconditional love and support he has given me.

I am thankful to all my friends for their friendship and support. I made many new friends and I thank them all for all the good times we had and for keeping my spirits high.

I thank God for letting me have this opportunity, giving me strength and looking after me.

I would also like to thank the following people in the Chemistry department at the University of Iowa - Janet Kugley, Earlene Erbe, Sharon Robertson, Frank Turner, Peter Hatch, Timothy Koon and Andrew Lynch. A special thanks to Jackie Jensen, who has always supported me as I rode the crests and troughs of a graduate life.

TABLE OF CONTENTS

LIST OF TABLES

Table

LIST OF FIGURES

Figure

CHAPTER I

INTRODUCTION

Geological evidence suggests that the temperature of the Earth has been varying repeatedly in the past. The Figure below by Intergovernmental Panel on Climate Change (IPCC), shows how the temperature has increased since 1860.[1] Many scientific reports suggest that human intervention has caused Earth's current temperature and climate changes, and this is a matter of immense concern.
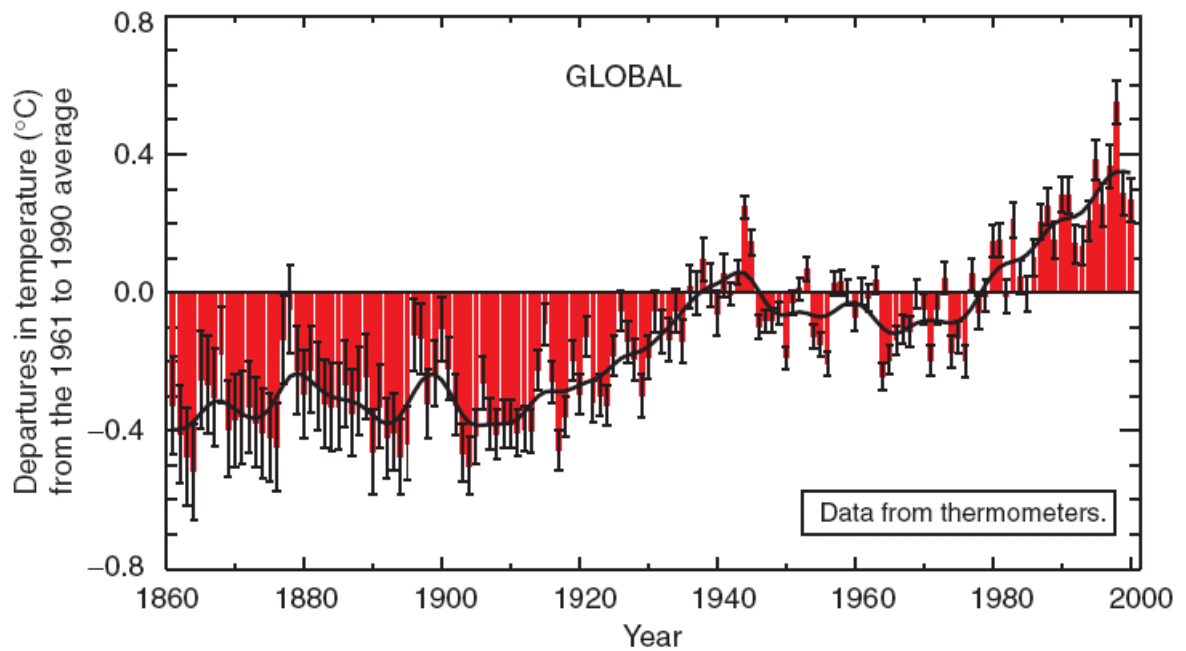
Figure 1.1: Global average surface temperature over the past 140 years.[1]

1.1 Greenhouse Gases and Human Activities

The term "Greenhouse Effect" was first coined by French physicist Joseph Fourier.[2] The greenhouse effect is the absorption of infrared radiation by the atmospheric gases resulting in the trapping of heat, which results in heating of Earth's surface.[3] Greenhouse gases contribute significantly to climate change. According to the IPCC, the increase in the global temperature is a result of increased concentrations of greenhouse gases caused by human activity such as fossil fuel burning, industrialization and deforestation.

1.2 Important Greenhouse Gases

Carbon dioxide, methane, water, chlorofluorocarbons (CFCs) and nitrous oxide are the primary greenhouse gases. At this point, it is interesting to note that since 1927 to the year 2006, the CO_2 (carbon dioxide) emissions released from industry and the burning of fossil fuel have increased from 1 billion tons per year to 8 billion tons per year,[4] suggesting that during this time-period tons of pollutant gases have been released into the environment as a result of human activities.

Carbon dioxide is the fourth most abundant gas in the atmosphere[5] and is uniformly distributed over our planet Earth's surface with a concentration of about 385 ppm.[6] Although CO_2 is naturally present in the Earth's atmosphere, its concentration has been rising gradually. Since the industrial revolution, the concentration of CO_2 has increased by 40%.[7] To understand the connection between CO_2 concentrations and global temperatures, Charles David Keeling commenced a systematic measurement of atmospheric CO_2 in 1958, at Mauna Loa at Hawaii and Antarctica.[8] The linear increase in the concentration of CO_2 during the past few decades can be seen below in the graph

from Mauna Loa observatory. Though water is a natural greenhouse gas, the greenhouse effect of water is not a concern as concentration of water does not change much with human activities.[9] Since 1860, there has been a 4.3% annual growth in the atmospheric level of CO_2 gas due to human reliance on oil, coal and other such fossil fuels used for heating and transportation.[9]

ATMOSPHERIC CO2 AT MAUNA LOA OBSERVATORY
Concentration (parts per million)
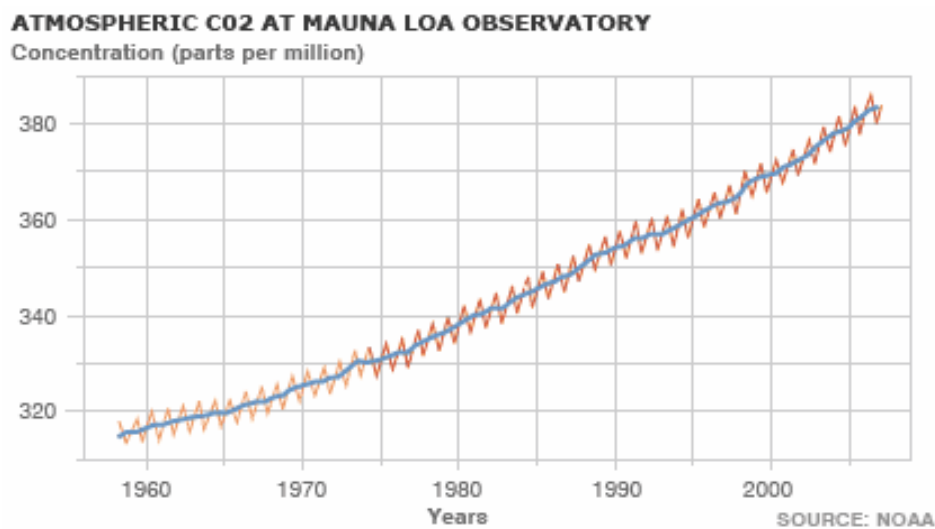
Figure 1.2: Mean annual carbon dioxide concentrations recorded at Mauna Loa in Hawaii.[10]

Figure 1.3 summarizes the global mean radiative forcing due to various atmospheric constituents. A positive radiative forcing results in warming of the atmosphere, and a negative forcing results in cooling of the atmosphere.[11] CO_2 has a high positive radiative forcing of 1.66 Wm^{-2}. Subsequently, the increasing emissions of CO_2 coupled with the high positive radiative forcing as noted above tends to warm the atmosphere even further.[11]

1.3 Evidence and Consequences of Global Warming

There is numerous recent evidence of global warming. The Arctic Sea ice has thinned by 40% in recent decades. The ice sheets of the planet are shrinking.[12-15] Even the

RADIATIVE FORCING COMPONENTS

RF Terms		RF values (W m^{-2})	Spatial scale	LOSU
Long-lived greenhouse gases	CO$_2$	**1.66** [1.49 to 1.83]	Global	High
	N$_2$O / CH$_4$ / Halocarbons	**0.48** [0.43 to 0.53] **0.16** [0.14 to 0.18] **0.34** [0.31 to 0.37]	Global	High
Ozone	Stratospheric / Tropospheric	**-0.05** [-0.15 to 0.05] **0.35** [0.25 to 0.65]	Continental to global	Med
Stratospheric water vapour from CH$_4$		**0.07** [0.02 to 0.12]	Global	Low
Surface albedo	Land use / Black carbon on snow	**-0.2** [-0.4 to 0.0] **0.1** [0.0 to 0.2]	Local to continental	Med - Low
Total Aerosol — Direct effect		**-0.5** [-0.9 to -0.1]	Continental to global	Med - Low
Total Aerosol — Cloud albedo effect		**-0.7** [-1.8 to -0.3]	Continental to global	Low
Linear contrails		**0.01** [0.003 to 0.03]	Continental	Low
Solar irradiance		**0.12** [0.06 to 0.30]	Global	Low
Total net anthropogenic		**1.6** [0.6 to 2.4]		

Radiative Forcing (W m^{-2}): -2 -1 0 1 2

©IPCC 2007: WG1-AR4

Figure 1.3: Global mean radiative forcing due to different atmospheric components anthropogenic as well as natural. Blue bars indicate a negative forcing and red bars indicate a positive forcing. Different greenhouse gases and components are shown in different colors.[11]

mountainous snow is melting. Overall, the world's glaciers are retreating which induce sea levels to rise.[16] There has been an escalation in the number of severe weather events

such as wild fires, heat waves and tropical storms. The oceans and trees are thought to have absorbed and are continually absorbing the additional CO_2 which is being released into the atmosphere. The absorption of this extra CO_2 by the oceans has lowered their pH. Marine ecosystems are continuously being damaged by ocean acidification, evident by the shrinking of marine life. Coral reefs are extremely sensitive to climate stress and are disappearing.

1.4 Long Term Effects

It is evident by now that CO_2 is continually being emitted into the atmosphere and is becoming a cause of our concern. Our concern is increased, as CO_2 is associated with high positive radiative forcing. Carbon dioxide has a long lifetime and according to the literature based on models, 20–35% of the CO_2 remain in the atmosphere after equilibration with the ocean, which takes 2-20 centuries.[17] This is then followed by further neutralization by formation of $CaCO_3$, which again occurs on long timescales of 3000 to 7000 yrs.[17] Considering all the above aspects of CO_2, it is evident that we are deteriorating the climate not only for us but also for the future generations.

1.5 Future

The various consequences of global warming (especially CO_2 increase), without intervention, could be numerous such as

1) The first and foremost impact of global warming is an increase in global temperatures. The IPCC predicts that by 2100, temperatures are likely to rise by 1.8 ^{o}C-4 ^{o}C, although the possible range is 1.1 ^{o}C-6.4 ^{o}C.[18]

2) The direct result of warming climate will be further melting of glaciers and snow cover. This decline will result in reducing water availability; especially in places where snow capped mountains are the water source.

3) The melting of ice has a direct correlation with rising sea levels. The coastal regions will be at an increased risk of flooding.

4) The other effect of increasing CO_2 concentrations, which we are seeing during recent times, is a rise in ocean acidity. It has been recently suggested that by 2100, the ocean pH is likely to fall to about 7.8, which will drastically impact marine life and organisms.[18]

5) All these effects will also be coupled with an increasing number of weather extremes. Areas prone to droughts and floods will likely experience an escalation in such drastic events. There will be development of stronger hurricanes, wildfires and other serious natural calamities, which we have already started experiencing.

6) The climatic changes will lead to serious implications on food production. Crop yields could increase in some areas such as East and Southeast Asia (20%), but decrease in others such as Central and South Asia (30%).[18]

7) According to the new report, "Adaptation of Forests and People to Climate Change – A Global Assessment", by the International Union of Forest Research Organizations (IUFRO), forests have been increasingly affected by the climate change. Growing atmospheric CO_2 concentrations can further induce forest mortality, and forests will release higher carbon dioxide quantities and result in even warmer temperatures. [19]

8) A mass extinction of many species from the ecosystem, particularly those with low capacity to adapt (the marine life) is predicted. Warming could lead to creation of oceanic dead zones, i.e. depletion of oxygen in the world's oceans. Climate Change Report - 2007

by IPCC on "Climate Change Impacts, Adaptation and Vulnerability" suggests the 20-30% of species are likely to be at high risk of irreversible extinction.[18]

To summarize, the climate change will not only affect the plant and animal species but also will eventually affect lives of millions of people. [18]

1.6 Management

Because carbon dioxide is a very important factor contributing to global warming, carbon dioxide storage and conversion have attained great importance in the scientific community and the public. One of the main strategies for CO_2 management is the direct capture of CO_2 from the source of emission. This can be then followed by longer time scale sequestration strategies similar to storing radioactive waste in large tanks underground. The other strategy is its adsorption on reactive substrates like zeolites and metal oxides and conversion to industrially useful products such as carbonates, bicarbonates, methanol, formic acid etc.

As the sequestration of CO_2 is important, understanding the atmospheric chemistry is equally important. CO_2 is released into the atmosphere in large quantities so it is also important to study the chemistry of CO_2 in the atmosphere, especially with the atmospheric aerosols.

1.7 Atmospheric Aerosol

The atmosphere is composed of various constituents. Aerosols are airborne particles composed of liquid and solids of different particle sizes (nanometers to micrometers in diameter).[20-22] The atmospheric aerosol is a complex mixture of a number

of different compounds that include inorganic, organic and also elemental carbon.[23-25] The surfaces of atmospheric aerosols can act as an important source of major heterogeneous atmospheric reactions, and it is very important to understand it thoroughly. The reactivity of CO_2 on these surfaces may be improved or diminished and may also depend on the amount of relative humidity in the atmosphere. Therefore, it becomes even more interesting to study the reactivity of carbon dioxide on aerosol particles in the presence and absence of relative humidity.

1.7.1 Mineral Dust Aerosol

At all times in the atmosphere, mineral dust is suspended, and on an average about 20 trillion grams of dust is in Earth's atmosphere.[26-30] Dust begins with erosion; the lighter particles stay suspended for a period of time and can be transported to far flung areas whereas the heavier dust particles fall down sooner due to gravitational pull.[26, 31] The dust storm events seem to escalate in areas where there is deforestation and strong winds.[32] Though the chemical composition of dust is complex and varies depending on the source region, it is generally comprised of metal oxides, zeolites, carbonates, and clays.[33-38] The mobility of dust is an important part of Earth's climate and it can affect the climate of Earth in a number of ways, such as affecting the cloud development, the amount of sunlight and rainfall.[39-44] In addition, dust aerosol can serve as a reaction surface for reactive gases such as CO_2, SO_2, NO_2 and others thus affecting atmospheric chemistry, which can in turn alter the atmospheric balance. There has been an increase in such processes in the atmosphere recently.[45, 46] Lately, we are hearing of multiple

instances of appearances of orange/red dust clouds over China and Australia that are a cause of concern as these can be potentially dangerous.

1.7.1.1 Zeolites

Zeolites are crystalline, porous aluminosilicates that are extensively used in catalysis, chemical separations and as adsorbents.[47] Zeolites are present in small amounts in atmospheric aerosols. Nanocrystalline zeolites are a class of zeolite materials with particle sizes below 100 nm. Due to their small size, nanocrystalline zeolites have unique properties such as high internal and external surface areas, high concentration of reactive sites on the external surface and enhanced diffusional properties. Zeolites can be ideal for the mass scale sequestering and/or conversion of CO_2 to more useful products. Recent studies indicate that there is a potential to use nanocrystalline zeolites in a number of environmental applications.[47-51] Faujasite zeolites (e.g. NaY) are considered promising environmental catalysts because of their cation exchange capacity and acid–base properties, and nanocrystalline NaY zeolites have shown enhanced performance for the selective catalytic reduction of NO_x ($NO_x = NO + NO_2$) with urea. [51, 52]

1.7.1.2 Metal Oxides

Mineral dust aerosol in the atmosphere consists of different types of metal oxides. Metal oxides are of great importance as an environmental interface. They act as heterogeneous catalysts where surface reactions of carbon dioxide can be carried out.[34, 53-58] In addition to understanding the atmospheric chemistry, adsorbing CO_2 on metal oxide can be a route for the conversion of CO_2 to useful industrial materials. In this thesis, there

is a lot of focus on the reactions of metal oxides with carbon dioxide in the presence and absence of relative humidity (co-adsorbed water).

Aluminum oxide is an important metal oxide. It is an abundant metal in the Earth's crust and is a significant component in the mineral dust aerosol. In the atmosphere, it exists in the form of different oxides, hydroxides and clays. Natural Al_2O_3 exists in different phases namely alpha, chi, kappa, gamma, delta, theta and eta. Similarly, there are numerous hydroxides of alumina such as gibbsite, boehmite, diaspore, nordstrandite and bayerite.[59-61] Aluminum oxides and hydroxides are abundant in the atmosphere, which make them ideal candidates to study atmospheric reactions with major atmospheric gases and especially CO_2. Therefore the reaction chemistry that occurs at the oxide interface needs to be understood. The adsorption of CO_2 on gamma alumina under dry condition has been extensively studied before. Busca and Lorenzelli suggest that the reaction of hydroxylated metal oxide surfaces with carbon dioxide results in the formation of adsorbed bicarbonates, carbonates (monodentate, bidentate, bridged and polydentate), and formates as well as bent CO_2 species.[62-68] However, not much has been studied about the adsorption of CO_2 on the aluminum hydroxide surfaces. It will be therefore interesting to compare the adsorption of CO_2 on aluminum oxide and aluminum hydroxide surfaces.

Zinc is another important naturally occurring mineral on Earth and exists in the form of important minerals such as sulfide, carbonate, oxide and other important minerals.[69] The applications of zinc oxide powder in industry are numerous. Recent studies of CO_2 adsorption on ZnO surface have shown the formation of an unusual tridentate carbonate species with the two O atoms of the CO_2 molecule being almost

equivalently bound to two different Zn surface atoms.[70] Though there have been numerous IR spectroscopic studies of CO_2 adsorption on zinc oxide surfaces, this is the first study to investigate the co-adsorption of carbon dioxide and water on the zinc oxide interface. Thus, in this study the role of co-adsorbed water on the adsorption chemistry of CO_2 on the zinc oxide surface is studied. To provide insights into the molecular structure of the carbonate, bicarbonate and carboxylate product formation as a result of reaction of CO_2 with the metal oxide surface, quantum chemical calculations were done.

Another metal oxide, which is equally important in the Earth's crust, is MgO; therefore it is essential to study CO_2 adsorption on it. It is also used for numerous application in catalysis, refractory material industries, paint, and superconductors.[71-73] Recently, MgO is also considered as a promising sorbent for chemisorption of various pollutants. Moreover alkaline earth-based oxide materials have received increased attention as adsorbents for CO_2.[74-76] In the case of MgO, stoichiometric amounts of CO_2 can be taken up according to the reaction: $MgO + CO_2 \rightarrow MgCO_3$. In this thesis, MgO nanomaterials with different surface areas are compared for their CO_2 sorption capacities.

1.8 Thesis Overview and Objectives

A range of experimental techniques were first used to analyze the nanomaterial samples used in this study for CO_2 adsorption. These methods include X-Ray Diffraction, ICP-OES, BET surface area analysis, Transmission Electronic Spectroscopy (TEM), and Scanning Electron Microscopy (SEM). All the samples were first characterized and after that the samples were analyzed for CO_2 adsorption using FTIR (Fourier transmission Infrared spectroscopy). As and when required, several other complementary collaborative

theoretical techniques were used to comprehend the adsorption of CO_2 on these samples. All these experiments as well as theoretical techniques used, have been discussed thoroughly in Chapter II.

In Chapter III, the adsorption of CO_2 on nanomaterial zeolite samples was investigated. The size effects and the affect of relative humidity were analyzed. It was also interesting to observe how the exchangeable cation affects bond lengths and frequencies of the adsorption. Theoretical quantum chemical calculations were performed in collaboration with Dr. Navea Juan using metal hydroxide cluster models to assist in the assignment of the vibrational frequencies and bond lengths of adsorbed species on the surface.

In Chapter IV, the adsorption of CO_2 on different alumina surfaces was studied. It was interesting to observe how the coordination of aluminum changed the product formation. For aluminum in tetrahedral sites, bicarbonate species are exclusively formed whereas for aluminum in octahedral coordination formed carbonate species mainly. The results suggest the important role played by the coordination of aluminum in product determination.

Chapter V comprises the study of CO_2 adsorption in the presence and absence of co-adsorbed water on the zinc oxide nanomaterial surface using transmission FTIR spectroscopy. Under dry conditions, CO_2 reacts with the surface hydroxyl groups to form adsorbed carbonate and bicarbonate as well as carboxylate. In the presence of water, spectroscopic studies confirm that CO_2 and water react on the surface of zinc oxide to form surface adsorbed carbonate species. Isotope FTIR studies were conducted which demonstrate an extensive exchange between oxygen atoms of adsorbed CO_2 and

adsorbed H_2O. To further aid the experimental vibrational assignments, quantum chemical calculations were performed in collaboration with Dr. Jonas Baltrusaitis using the zinc oxide surface.

Lastly, in Chapter VI, size and surface area effects are studied. The adsorption of CO_2 on MgO resulted in formation of surface physically adsorbed CO_2 and carbonate as well as bicarbonate product. Out of these products, the carbonate species was the most stable one. The adsorption of CO_2 on commercially available MgO material was compared with the high surface area synthesized MgO. The high surface area material showed enhanced product formation, as expected.

Conclusions are summarized in Chapter VII. This comprises general conclusions, which are drawn from the research. The results presented also provide an insight into the CO_2 reaction chemistry on the mineral dust aerosol in the atmosphere. Moreover, a comparison of various materials based on their CO_2 adsorption capacity, both by physical adsorption and chemical adsorption (by the formation of carbonates and bicarbonates as well as carboxylate species), is made.

CHAPTER II

EXPERIMENTAL METHODS

A number of experimental techniques and methods were utilized in this research study and are discussed in details in this chapter. Though Fourier transform infrared (FT-IR) spectroscopy was used most extensively for the research, other techniques were used in conjunction to characterize the nanomaterials. The custom-built FT-IR apparatus used is described in detail here and has been discussed before in the literature.[52] Other techniques used for characterization of the nanomaterials were X-Ray diffraction (XRD), Scanning electron microscopy (SEM), Transmission electron microscopy (TEM), Inductively coupled plasma optical emission spectroscopy (ICP-OES) and Brunauer, Emmett, and Teller Surface area analyzer (BET). When required, quantum calculations were done to support the research conclusions, which are also discussed in this chapter.

2.1 Transmission FT-IR Spectroscopy Experiments

2.1.1 Experimental Setup for Transmission FT-IR Studies

A Mattson Infinity Gold FTIR spectrometer with a liquid nitrogen-cooled narrow band mercury–cadmium–telluride (MCT) detector was used to probe the CO_2 adsorption on nanomaterials. The set up consists of a stainless steel infrared sample cell that is placed inside the sample compartment of the spectrometer. This stainless steel cell has external dimensions of approximately 7 cm x 7 cm x 7 cm (length x width x height) and internal volume of 319 mL as shown in Figure 2.1 This cell is equipped with two BaF_2 windows for infrared measurements which were sealed by O-rings in the IR cell. Inside
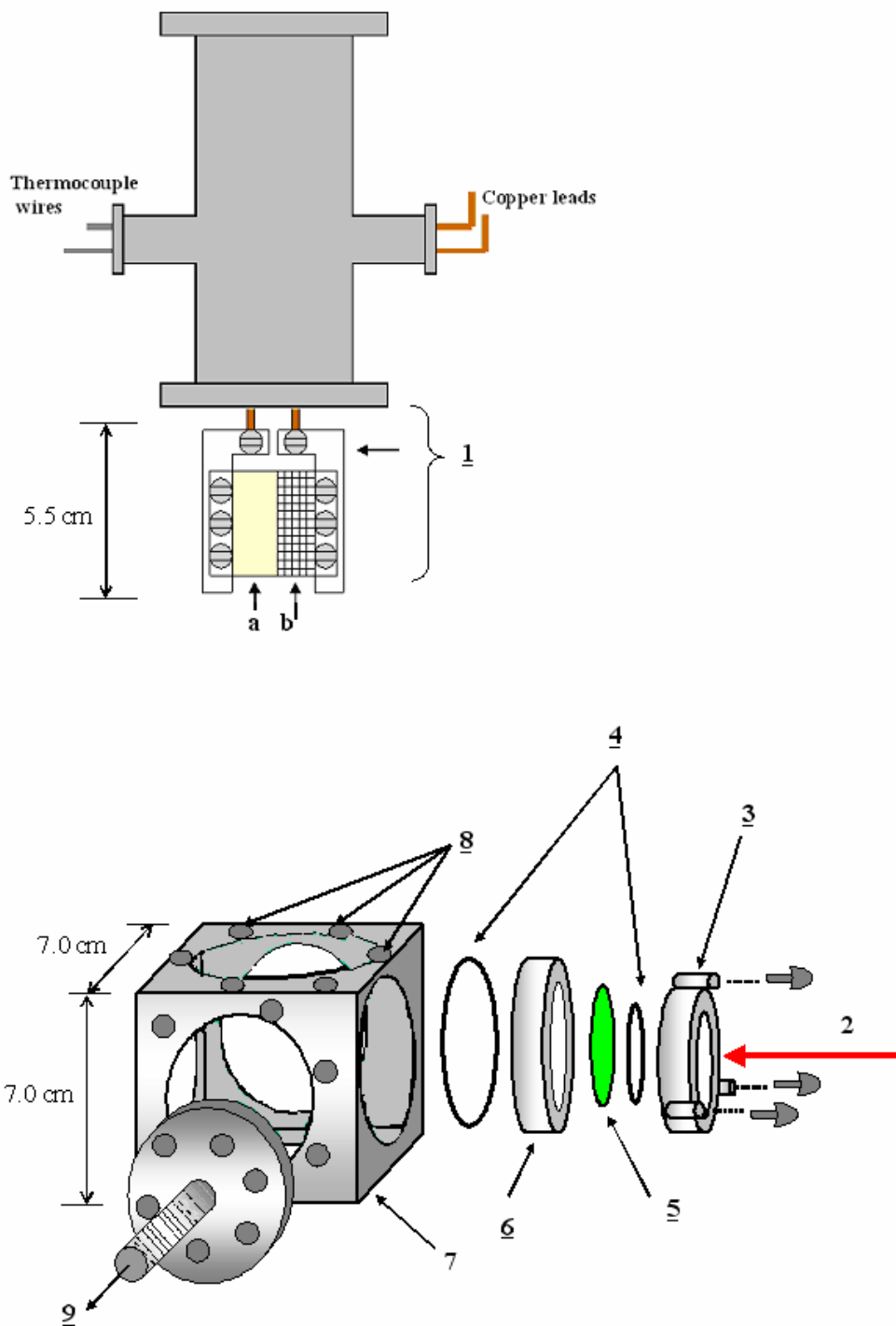
Figure 2.1: Schematic of the IR cell used for transmission FT-IR studies: 1. Photoetched tungsten grid held by sample holder jaws (a) the sample side and (b) blank grid side; 2. Infrared incident light; 3. Aluminum screws and holder for the BaF_2 windows; 4. O-rings to hold the BaF_2 windows; 5. BaF_2 window; 6. Stainless steel holder; 7. Stainless steel infrared cube; 8. Holes for clamping the sample holder; 9. Gas or vapor inlet/outlet towards the gas handling system.[77]

the IR cell is the sample holder that consists of a 2.5 cm x 2.5 cm photoetched tungsten grid held in place by nickel jaws. The nickel jaws are connected to the copper leads so that the sample can be resistively heated. Thermocouple wire is attached directly to the tungsten grid and is used to determine the sample temperature. The sample holder is then placed inside the stainless steel cube that sits on a linear translator, as shown in Figure 2.2. The linear translator allows the sample grid to be translated forward as well as backward with respect to the infrared beam. Such a set up permits the detection of gas-phase and adsorbed species under identical reaction conditions. The IR reaction cell is connected to the premix chamber, which in turn is connected to a vacuum/gas handling system. Through the gas handling system, known amount of gases (CO_2) or vapors (water vapor) can be premixed in the premix chamber before being introduced in the reaction cell. The volume of the total system is 1197 mL (sample cell + premix chamber + gas manifold). The volume of premix chamber and the gas manifold together is 878 mL. Two absolute pressure transducers (MKS instruments) were used to monitor the pressures of gases introduced. These operate in different ranges of pressure; 0.001 to 10.00 Torr and 0.1 to 1000 Torr. The IR cell compartment is put in the dry air purge throughout. The purge air is cleaned and generated by air generators. The IR cell, premix chamber and the gas handling system can be differentially pumped under a vacuum of a turbo and mechanical pump, in combination, that are used to evacuate the overall system pressure down to around 1 x 10^{-6} Torr. Finally commercial WinFirst software is used to record the FT-IR spectra collected by the spectrometer.
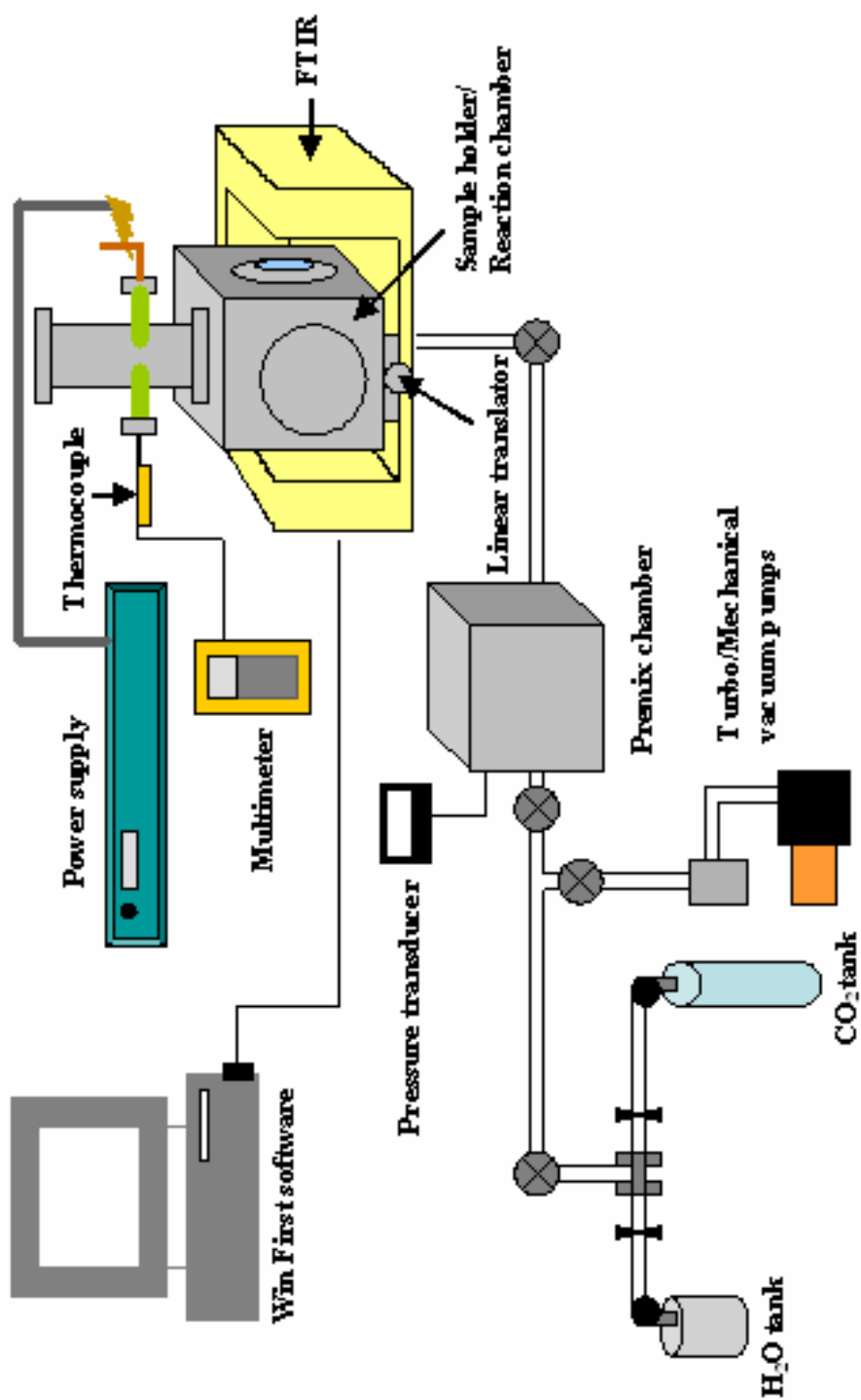
Figure 2.2: Schematic representation of the experimental setup for transmission FT-IR studies.[78]

2.1.2 Protocol for FT-IR Experiments

The IR sample holder sits on the linear translator that allows in situ evaluation of both the sample and gas-phase. This instrumental set up allows detection of gas-phase (Figure 2.3(a)), the surface sample with adsorbates (Figure 2.3 (b)), and also the sample surface (Figure 2.3 (c)). This can be followed by taking a difference spectrum to obtain information of adsorbed species (Figure 2.3 (d)). The subtraction of the clean sample spectrum (BaY zeolite surface is used as an example here) from the spectrum of sample (BaY zeolite) with adsorbed species gives the spectrum for the adsorbed species. The gas-phase (here CO_2) spectrum can be obtained by ratioing the blank side of the grid under gas exposure to the one without it. Thus a spectral manipulation allows both the gas-phase and the surface to be studied at the same time. All the IR spectra were recorded at approximately 296 K. Each spectrum was obtained by averaging 256 scans at an instrument resolution of 4 cm^{-1} or otherwise specified. Each absorbance spectrum shown represents a single beam scan referenced to the appropriate single beam scan of the clean zeolites or the blank grid, unless otherwise noted. Timed experiments can be done by running a macro program. The macro automatically records IR spectra of the gas-phase or sample surface at regular time intervals. The FT-IR instrumental parameters and macro programs are given in Appendix A.

2.1.3 Sample Preparation for FT-IR Studies

A mass of 10-20 mg of the sample was either coated (mixed with water) or pressed onto the photoetched tungsten grid (Figure 2.1). The samples were either evacuated only or heated along with evacuation. Heating temperatures were decided with

2.2 X-Ray Diffraction

Powder X-Ray diffraction measurements were performed using a Bruker D-5000 q-q diffractometer with a Cu Kα source and a Kevex energy-sensitive detector. This was used to determine the purity of samples as well as the different phases that were present.

2.3 Scanning Electron Microscopy

Scanning electron microscopy (SEM, Hitachi S-4000) was used to determine particle morphology and particle size of the nanomaterials. Particles were either sprinkled or a dilute solution of sample in water or methanol was dropped onto an aluminum stub. The sample was coated with gold under argon atmosphere. Sample imaging was done using an accelerating voltage of 15 kV, which was followed by computer software to generate images of the respective samples.

2.4 Transmission Electron Microscopy

Transmission electron microscopy was used to determine the particle size distribution of nanomaterials. JEOL JEM-1230 with a Gatan ultrascan camera was used to acquire images. The nanoparticles were deposited on copper TEM grids. An accelerating voltage of 40-120 kV was used for sample imaging. Finally a computer software was used to generate a particle size distribution.

2.5 Surface Area Measurements

Quantachrome Nova 4200e surface area analyzer was used to determine the surface areas for the samples, using a seven-point N_2-BET (Brunauer, Emmett and Teller) adsorption isotherm. For each surface area measurement, approximately 0.2 g of sample was taken. Prior to surface area measurements, the individual samples were either evacuated or heated in heating jackets overnight. For zeolites, the external surface area and total surface area was measured before and after removing the template from the synthesized zeolite sample. The heating temperature used was determined based on factors such as phase/size transition temperature and other factors as discussed previously.

2.6 Inductively Coupled Plasma Optical Emission Spectroscopy

The Si/Al/Ba ratio of the Y zeolite samples was determined by a Perkin Elmer Plasma 400 Inductively Coupled Plasma Atomic Emission Spectrometer (ICP/AES) spectrometer. Samples were first digested by dilute HF acid followed by neutralization in $NaBO_3$. Four standard calibration solutions with known silicon (aluminum, sodium, and copper) concentrations were prepared.[79] A working curve was then generated, from which the silicon, aluminum, sodium and barium concentrations in various zeolite sample solutions were obtained.[79]

2.7 Quantum Chemical Calculations

Quantum chemical calculations were performed in order to better understand the influence of adsorption on the structure and vibrational frequencies of physisorbed

carbon dioxide and chemisorbed products (formation of carbonate, bicarbonate and carboxylate species).

2.7.1 Adsorption of CO_2 on Zeolite Nanomaterials

Both energy optimization and vibrational frequency calculations were performed with the hybrid Becke (B3) exchange and the Lee, Yang, and Parr (LYP) correlation (B3LYP) functionals in combination with the Los Alamos ECP and double-ζ level of theory (LanL2DZ) as implemented in the GAUSSIAN 03 package.[80] Calculations were done using different gas-phase cluster structures with two different cations, Na^+ and Ba^{2+}. In order to have a formally neutral cluster, the hydroxyl complexes of the corresponding cations were used. In addition, carbonate and bicarbonate possible products were investigated with B3LYP LanL2DZ, and the geometry optimization was conducted using carbonate and bicarbonate models as the neutral clusters $BaCO_3$; Na_2CO_3; $BaOH(CO_3H)$ and; $Na(CO_3H)$.

2.7.2 Adsorption of CO_2 on ZnO Nanomaterials

Quantum calculations were performed for adsorption of CO_2 on ZnO. All molecules and clusters were optimized within the Density Functional Theory approximation [81] using spin restricted calculations with B3LYP functional[82-84] as implemented in Turbomole and TZVP basis set [85, 86] with multipole accelerated resolution of identity approximation[87] (MARIJ-B3LYP/ TZVP). No symmetry constraints were imposed during the geometry optimization. Vibrational frequencies were calculated after the optimization at the same level of theory to confirm that the optimized geometry was a

minimum in the potential energy surface. No negative vibrational frequencies were observed for minimum structures. Geometry optimization and frequency calculations were performed using Turbomole 6.1 package running on a Linux workstation.[88] All structures were visualized using commercially available Chemcraft software.[89]

2.8 Reagents and Materials

2.8.1 Zeolites

Three different zeolite nanomaterials were used in this study, namely commercial zeolite, NaY (Sigma-Aldrich), synthesized BaY and synthesized nano NaY. BaY was prepared from NaY (Sigma-Aldrich) using standard ion-exchange procedures as described previously.[52] Briefly, the sample preparation of nano NaY is described in Chapter III. A Hitachi S- 4000 scanning electron microscope was used to obtain images of these nanomaterials. The crystal sizes of NaY, BaY and synthesized nano NaY were determined to be 1000 nm, 1000 nm and 38 nm respectively. The surface area of these nanomaterials was determined using the BET surface area analyzer. The external surface area has been determined to be ca. 1 m^2/g, 1 m^2/g and 106 m^2/g, respectively.[90] Physical properties and source of these samples are summarized in Table 2.1. The Si/Al ratio determined for NaY and nano NaY is 2.0 and 1.8, respectively, as measured by inductively coupled plasma optical emission spectroscopy (ICP-OES). In BaY the Ba/Al ratio was determined by ICP/OES to be 0.65.

2.8.2 Metal Oxide Powders

The physical properties of different metal oxide samples used are also summarized in Table 2.1 along with the zeolites. Two types of aluminum based oxides were used. γ-Al_2O_3 with a surface area of 195 m^2/g was purchased from Nanostructured and Amorphous Materials, Inc. (Houston, TX). Alumina whiskers, from Sigma-Aldrich (St. Louis, MO), was a mixture of boehmite and bayerite with a surface area of 320 m^2/g. Another metal oxide, ZnO, was received from Meliorum Technologies, Inc. (Rochester, NY) and determined to have a low surface area of 15 ± 1 m^2/g and size of 5 nm. A JEOL JEM-1230 transmission electron microscope was used to obtain images of the nanoparticulate metal oxides. Two other metal oxide samples, MgO, were used in this study. Both commercially available and lab synthesized MgO samples were used. The synthesis of 9 nm MgO is explained in details in Chapter VI. For comparison studies, a low surface area (35 m^2/g) MgO sample was purchased from Sigma-Aldrich (St. Louis, MO). X-ray diffraction patterns of the powders confirmed the crystalline phases of these samples.

2.8.3 Gases

Research-grade purity carbon dioxide ($C^{16}O_2$) was purchased from Airgas. $C^{18}O_2$ (minimum 97 atom % ^{18}O), ^{18}O labeled carbon dioxide, was purchased from ISOTEC. Both the gases were used directly without any purification.

2.8.4 Liquid Reagents

Water vapor was taken from the headspace of different glass bulbs. Distilled H_2O used was Optima grade and was purchased from Fisher Scientific Inc. Distilled H_2O was purified by freeze, pump thaw cycles and was also degassed prior to use. ^{18}O labeled water, $H_2^{18}O$ was purchased from ISOTEC (minimum 95 atom % ^{18}O) and used as received. Prior to use ^{18}O labeled water ($H_2^{18}O$) was transferred to a glass bulb under nitrogen atmosphere.

Table 2.1: Summary of nanomaterials used in this thesis study.

Nanomaterial Surface	Size (nm)	Surface Area (m^2/g)	Source
NaY	1000	655	Sigma-Aldrich
BaY	1000	332	Synthesized
Nano NaY	38	523	Synthesized
Alumina Whiskers	4x2800	320	Sigma-Aldrich
10 nm Alumina	10	195	Nanostructured and Amorphous Materials
ZnO	23	15	Melorium Technologies
Synthesized MgO	9	121	Synthesized
Commercial MgO	36	35	Sigma-Aldrich

CHAPTER III

CARBON DIOXIDE ($C^{16}O_2$ AND $C^{18}O_2$) ADSORPTION IN ZEOLITE Y MATERIALS: EFFECT OF CATION, ADSORBED WATER AND PARTICLE SIZE

3.1 Abstract

In this study, CO_2 adsorption in the presence and absence of co-adsorbed H_2O was investigated in zeolite Y. Several different zeolite Y materials were investigated including commercial NaY, commercial NaY ion-exchanged with Ba^{2+} and nanocrystalline NaY; herein referred to as NaY, BaY and nano NaY. Following heating of these zeolites to 573 K and cooling to room temperature, CO_2 was adsorbed as a function of pressure. FTIR spectra show that a majority of CO_2 adsorbs in the pores of these three zeolites (NaY, BaY and nano NaY) in a linear complex with the exchangeable cation, as indicated by the intense absorption band near 2350 cm^{-1}, assigned to the v_3 asymmetric stretch of adsorbed CO_2. Most interesting is the formation of carbonate and bicarbonate on the external surface of nano NaY zeolites as indicated by the presence of several broad absorptions bands in the 1200 -1800 cm^{-1} region suggesting unique sites for CO_2 adsorption on the surface of the nanomaterial. For the other two zeolite materials investigated, bicarbonate formation is only evident in BaY zeolite in the presence of co-adsorbed water. Adsorption of ^{18}O-labeled carbon dioxide and theoretical quantum chemical calculations confirm these assignments and conclusions.

3.2 Introduction

Carbon dioxide (CO_2) is the fourth most abundant gas in the atmosphere uniformly distributed over the Earth's surface with a concentration of about 385 ppm.[6] Globally the CO_2 concentration has increased by more than 40% since the Industrial Revolution and is continuously increasing.[7] As CO_2 plays an important role in global warming, it has become necessary to think about new approaches and novel ideas for CO_2 management. Some of the strategies to reduce its concentration include reducing emission from vehicles and industries, using alternate sources of energy (wind energy, tidal energy, and solar energy), gas capture and adsorption, sequestration and recycling similar to radioactive waste and adsorbing it on reactive substrates such as metal oxides. Recent studies indicate that zeolites have the potential to adsorb, store and convert CO_2 into more useful products.[91-95]

Zeolites can perhaps be ideal for the mass scale sequestering and/or conversion of CO_2 to more useful products. Zeolites are crystalline, porous aluminosilicates that are extensively used in catalysis, chemical separations and as adsorbents.[47,48] Nanocrystalline zeolites are a class of zeolite materials with particle sizes below 100 nm. Due to their small size, nanocrystalline zeolites have unique properties such as both high internal and external surface areas, high concentration of reactive sites on the external surface and enhanced diffusional properties.[47,48] Recent studies have shown that nanocrystalline zeolites have potential use in a number of environmental applications.[47-52] Faujasite zeolites (e.g. NaY) are considered promising environmental catalysts because of their cation exchange capacity and acid–base properties, and nanocrystalline NaY zeolites

have shown enhanced performance for the selective catalytic reduction of NO_x (NO_x = $NO + NO_2$) with urea.[52]

In this study, adsorption of $C^{16}O_2$ and $C^{18}O_2$ was investigated on synthesized nanocrystalline NaY zeolite (nano NaY) as well as commercially available zeolite catalysts (NaY, BaY) under both dry conditions and in the presence of co-adsorbed water. FTIR spectroscopy was used to probe adsorbed CO_2. In particular, we present in this study: *(i)* experimental data for CO_2 adsorption in three zeolite Y materials including isotope data to support vibrational mode assignments; *(ii)* CO_2 adsorption in a new type of zeolite, nanocrystalline zeolites with particle size below 100 nm, where unique carbon dioxide adsorption sites are observed due to the high external surface area and; *(iii)* experimental data which probes the impact of adsorbed water on the reactivity of the three zeolites investigated (NaY, BaY and nano NaY). Besides the isotope data, quantum chemical calculations are used to aid in the mode assignments. It is shown here that zeolite Y adsorbs CO_2 both molecularly, in a linear bonded complex, as well as through the formation of carbonates and bicarbonates depending upon the zeolite and experimental conditions, i.e. in the presence and absence of co-adsorbed water, the exchangeable cation and the zeolite particle size.

3.3 Experimental and Theoretical Methods

3.3.1 Zeolite Materials

Commercial zeolite, NaY (Aldrich) and synthesized nano NaY[50] were used for these studies. The crystal sizes were ~1 nm and 38 nm for NaY (Aldrich) and nano NaY, respectively. Figure 3.1 shows scanning electron micrographs of these two different
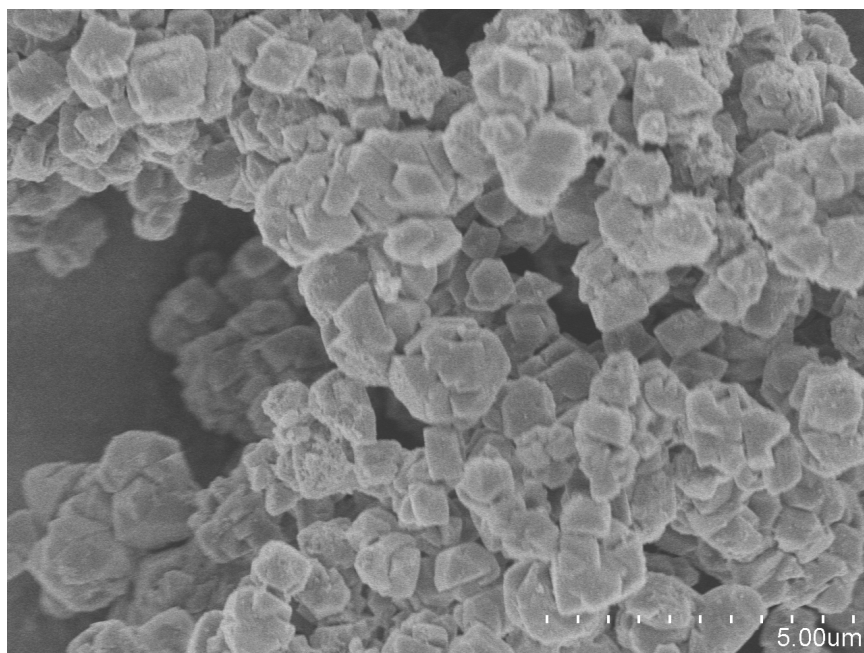
(a)
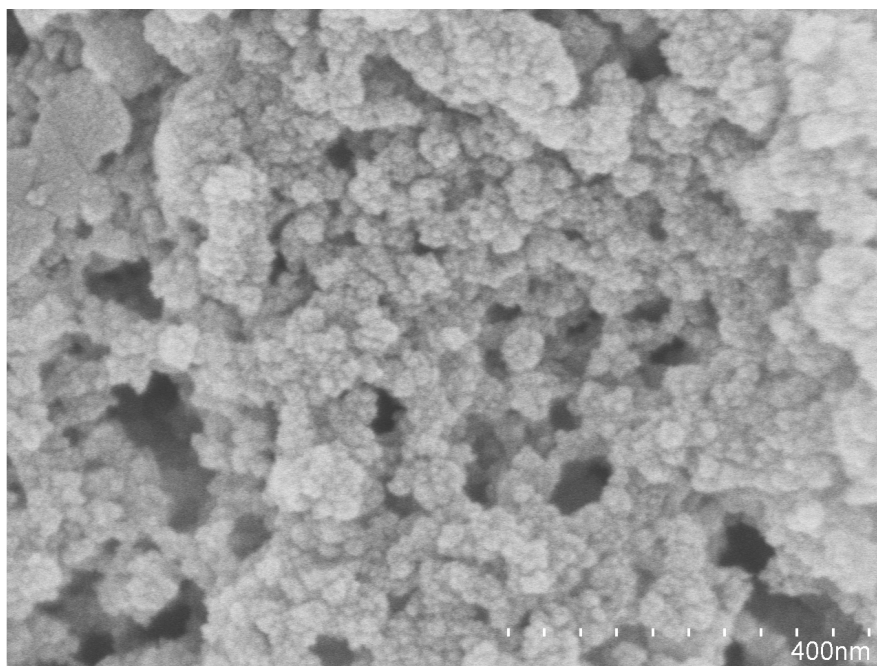
(b)

Figure 3.1: Different zeolite materials used in the study. (a) NaY (Aldrich) and (b) nano NaY.[94]

zeolite samples. The most important difference between the two samples is particle size and the difference in external surface area. The external surface area for the two sizes has been determined to be *ca.* 1 m^2/g and 106 m^2/g, respectively.[79] As discussed previously, the external surface area for the 38 nm nano NaY is 100 times greater than the commercial sample. The external surface provides for additional reaction sites and functionality in these nanocrystalline zeolite materials. The Si/Al ratio determined for NaY (Aldrich) and nano NaY is 2.0 and 1.8, respectively, as measured by inductively coupled plasma optical emission spectroscopy (ICP-OES).

BaY was prepared from NaY (Aldrich) using standard ion-exchange procedures as described previously.[90] Briefly, aqueous 0.5 M $BaCl_2$ solution was added to NaY and stirred with heating to 363 K for 24 h. The resulting solution was washed with deionized water and filtered until the filtrate was free of chloride ions. The Ba/Al ratio was determined by ICP/OES to be 0.65.

3.3.2 Transmission FTIR Spectroscopy

In situ transmission FT-IR spectroscopy was employed to investigate the adsorption of CO_2 in zeolite materials. The infrared sample cell used here has been described previously.[51] The Mattson Galaxy 6000 infrared spectrometer is equipped with a narrowband MCT detector. It consists of a stainless steel IR cell equipped with two BaF_2 windows for infrared measurements and is connected to a vacuum/gas handling system. Inside the IR cell is the sample holder that consists of a photoetched tungsten grid held in place by nickel jaws. Approximately 12 mg of zeolite sample was mixed with a few drops of methanol and sonicated for 20 minutes. This preparation resulted in

the formation of a suspension. The suspension was then coated onto half of the tungsten grid and allowed to dry. The IR cell was then placed inside the stainless steel cube that sits on a linear translator inside the FTIR sample compartment. The samples were heated overnight under vacuum at 513 K or higher to remove adsorbed water. Reactant gases were introduced into the reaction cell through the gas handling system. In the dry experiments, i.e. in the absence of co-adsorbed water, the zeolite was equilibrated for around 30 minutes with carbon dioxide prior to a spectrum being recorded. Carbon dioxide and water were also co-adsorbed into the zeolite. In these experiments, water vapor (1% RH) was introduced into the reaction cell and allowed to equilibrate followed by evacuating the cell for an hour to remove any gas-phase water in the reaction cell. Carbon dioxide was then adsorbed at different pressures at a temperature of 298 K. The exact pressures are given in the figure captions. Each spectrum was obtained by averaging 256 scans at an instrument resolution of 4 cm^{-1}. Each absorbance spectrum shown represents a single beam scan referenced to the appropriate single beam scan of the clean zeolites or the blank grid, unless otherwise noted. It should be noted that the zeolite absorbs strongly below 1300 cm^{-1} and can result in a sloping background in this region as a result of poor spectral subtraction.

3.3.3 Quantum Chemical Calculation of Carbon Dioxide,
Bicarbonate and Carbonate Complexes

In order to better understand the influence of adsorption on the structure and vibrational frequencies of carbon dioxide, several quantum chemical calculations were performed. All the electronic structures minimizations and vibrational calculations were performed using density-functional method, with the hybrid Becke (B3) exchange and the

Lee, Yang, and Parr (LYP) correlation (B3LYP) functionals in combination with the Los Alamos ECP and double-ζ level of theory (LanL2DZ) as implemented in the GAUSSIAN 03 package.[80]

As it has been previously shown that the primary interaction between carbon dioxide and zeolites is with the exchangeable cation,[96-100] calculations were done using different gas-phase cluster structures with two different cations, Na^+ and Ba^{2+}. In order to have a formally neutral cluster, the hydroxyl complexes of the corresponding cations have been used. The electrostatic contribution from the hydroxyl counter ion (OH) serves as a good model to resemble the interaction between the cation and the zeolite oxygen atoms. Figure 3.2 shows the minimized structures for the different models: (a) and (b) show the CO_2 complex the corresponding metal hydroxide, Na(OH) and $Ba(OH)_2$. In addition, carbonate and bicarbonate possible products have also been investigated with B3LYP LanL2DZ, and the geometry optimization for carbonate and bicarbonate models are shown in Figure 3.2 as the neutral clusters (c) $BaCO_3$; (d) Na_2CO_3; (e) $BaOH(CO_3H)$ and; (f) $Na(CO_3H)$.

To aid in the interpretation of the experimental data, calculations were performed for both $C^{16}O_2$ and $C^{18}O_2$ on different carbon dioxide isotopes. These fundamental vibrational frequencies on gas-phase carbon dioxide have been reported in previous studies using B3LYP/6-31G(d) level of theory.[101] Here, in order to determine the effect of the basis set used, fundamental vibrational frequencies were determined for $C^{16}O_2$ and the labeled $C^{18}O_2$ at B3LYP LanL2DZ level of theory. In addition, the frequencies of the clusters were calculated using the basis set 6-311+G(d,p) for Na^+ coordinated to CO_2, as well as several other ions coordinated to CO_2, to determine the effect of the LAN2DZ

basis set on the frequencies. Differences in the frequencies calculated between the two basis sets were determined to be small ($\leq$ 2%), which is in good agreement with previously reported studies.[102]

It is important to note that because all the calculated frequencies correspond to the vibrational modes of the molecule in gas-phase, the experimentally observed frequencies of the adsorbed species may be slightly different than those in the calculated spectra. Furthermore, the calculated harmonic frequencies tend to differ from experimental values due to a combination of anharmonicity effects, electron density correlation effects and basis set deficiencies. In order to best correct for these, an empirical scaling has been applied based on the harmonic frequencies calculated and the observed experimental data for gas-phase carbon dioxide. The scaling factor used to correct the calculated CO_2 frequencies was obtained from averaging the calculated-to-experimental ratio of the different vibrational modes for the isolated CO_2 molecule that are infrared active: the asymmetric stretching ν_3 and the doubly degenerated ν_2 bending modes (the symmetric stretching ν_1 is only Raman active).[103-105] The averaged scaling factor was determined using also the experimental and calculated values for the isotopic labeled $C^{18}O_2$. Thus, the frequencies of the CO_2 vibrational modes have been scaled using an empirical scaling factor of 0.95. The scaling factor facilitates the assignments of the vibrational frequencies measured using FTIR spectroscopy.

3.4 Results and Discussion

*3.4.1 Quantum Chemical Calculations of Carbon Dioxide,
Bicarbonate and Carbonate Complexes*

CO_2 interactions with hydroxyl metal clusters were calculated, with the surface being modeled as $M_n(OH)$ (*M* correspond to the ion exchange, Ba^{2+} or Na^+), as illustrated in Figure 3.2. The OH counter ion modified the electron density associated with the carbon dioxide molecule and the cation (M^{n+}) of interest, thus resembling the influence of a local zeolite structure in a simplified fashion. It can be seen that for the minimized structures shown in Figure 3.2 (a) and (b), the interaction with the cation causes an increase in the length of the C-O bond adjacent to the cation, subsequently decreasing the length of the other C-O bond. As discussed below, this change in molecular symmetry gives rise to an infrared active symmetric ν_1 vibrational mode. The calculated bond lengths for carbon dioxide are identical for both structures containing either Na^+ or Ba^{2+}. In particular, the bond lengths calculated for the clusters are calculated as:

$$\frac{dC-O^{Na^+}}{dC-O} = \frac{dC-O^{Ba^{2+}}}{dC-O} = 1.003 \tag{1}$$

Importantly, from the perspective of this study, the ν_1 vibrational mode becomes IR active as a result of the interaction with the cation and the asymmetry in the bond lengths. Fundamental vibrational frequencies calculated for unlabeled and ^{18}O labeled gas
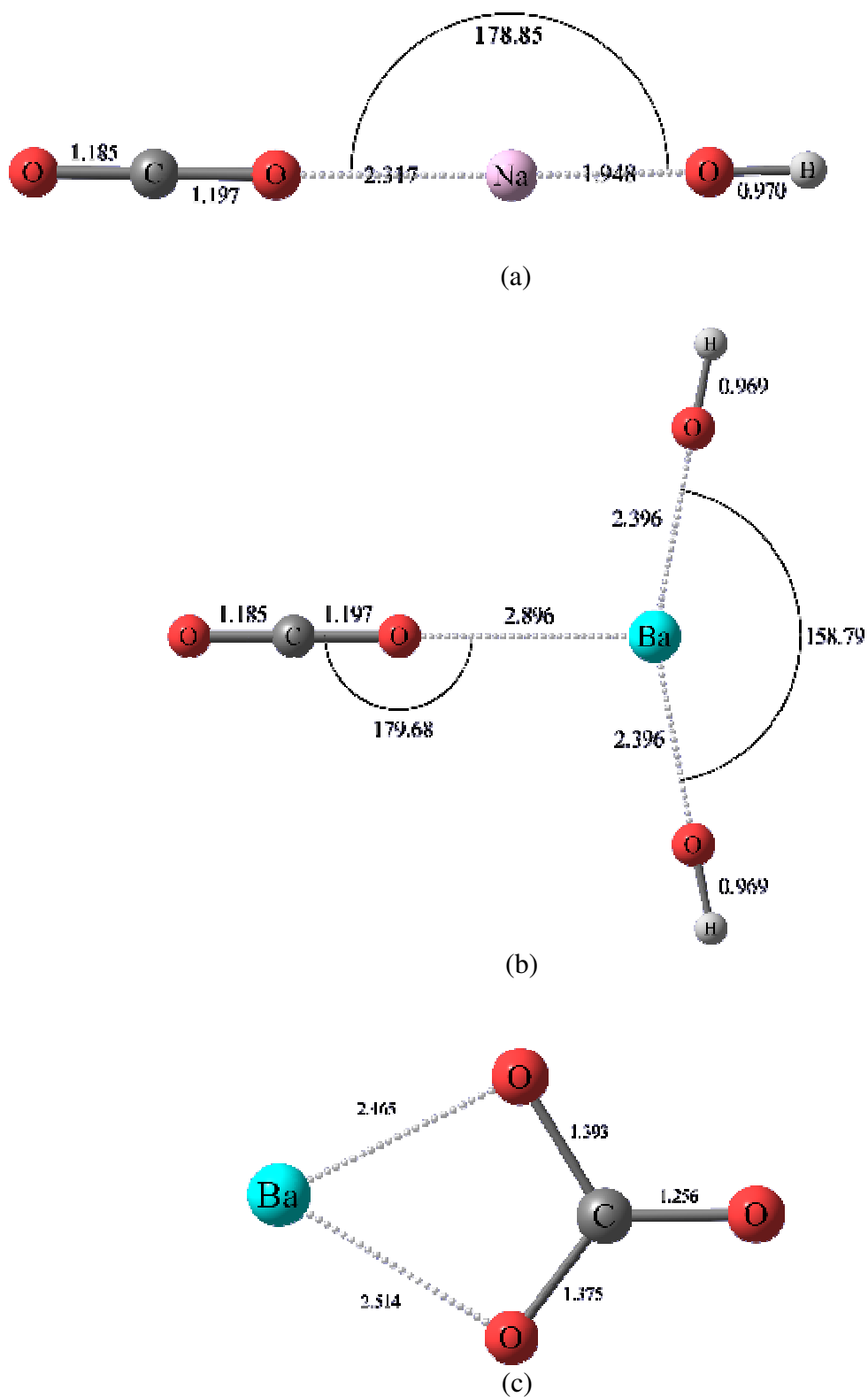
Figure 3.2: Energy minimized structures for (a) (OH)Na···O-C-O; (b) (OH)$_2$Ba···O-C-O; and energy minimized structures for carbonate and bicarbonate complexes with Ba^{2+} and Na$^+$: (c) BaCO$_3$; (d) Na$_2$CO$_3$; (e) Ba(OH)CO$_3$H; and (f) (OH)NaCO$_3$H.
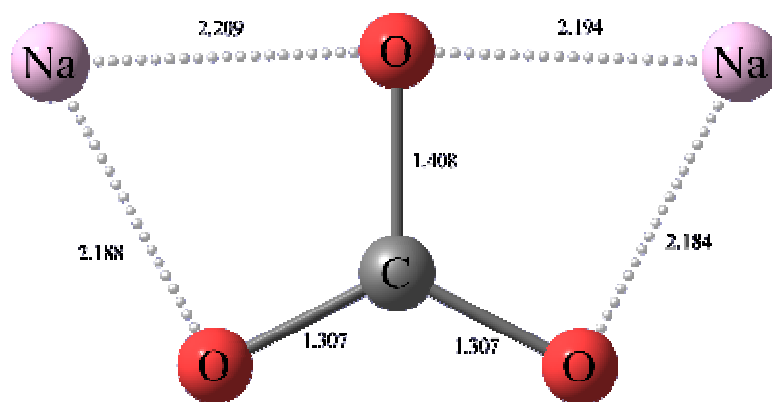
(d)
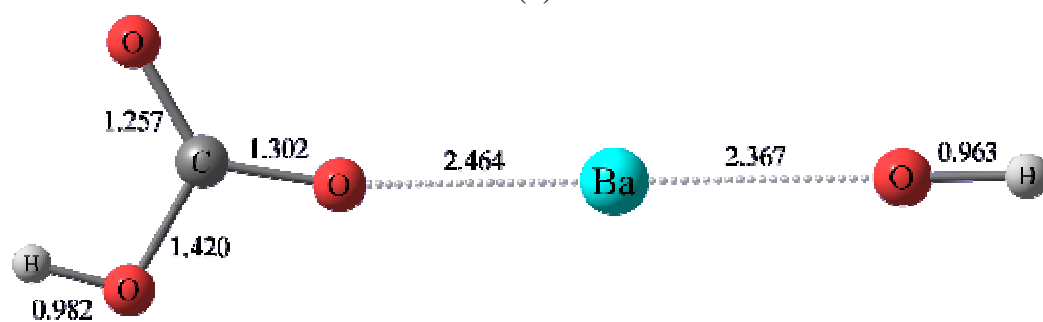
(e)
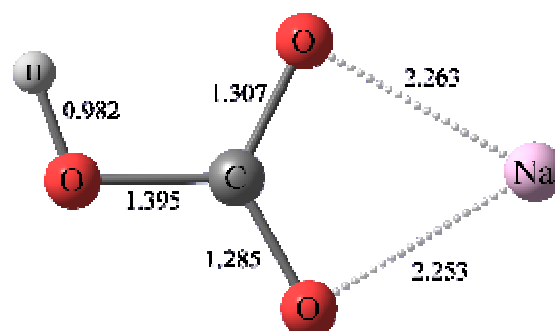
(f)

(Figure 3.2 continued)

phase CO_2 and CO_2 clusters (3.2 (a) and (b)) are given in Tables 3.1 and 3.2, respectively, along with their relative intensities. The reported frequencies are calculated at the same level of theory and scaled to a proper scaling factor, as discussed previously in the Experimental Section.

Compared with the asymmetric stretch of carbon dioxide (Table 3.1), ν_3, and the Raman active ν_1, both vibrational frequencies show a surface influence. In addition, Table 3.1 shows the calculated frequencies for the equivalent-energy in-plane and out-of-plane CO_2 bending vibrational modes (ν_2). Upon interaction with the surface, this doubly degenerated CO_2 bending mode (ν_2) of the isolated molecule is separated into two different vibrations attributed to the change of symmetry of the molecule: an in-plane bending mode, $\nu_2(O\text{-}C\text{-}O)a$, and an out-of-plane bending mode, $\nu_2(O\text{-}C\text{-}O)b$. For the models shown in Figure 3.2, the symmetry is approximately maintained in most cases, although the contrast between these two bending modes becomes more pronounced. This energy difference in the ν_2 bending modes is more obvious in the $(OH)_2Ba\cdots O\text{-}C\text{-}O$ cluster, where an in-plane bending mode could be further distinguished from an out-of-plane bending mode due to cluster geometry. On a zeolite frame, this symmetry distortion will resemble the ion-exchange solvating zeolite ring. The CO_2 ν_3 vibrational frequency difference upon interaction with $Na(OH)$ and $Ba(OH)_2$ is about 2 cm^{-1}. In addition, there is a transition dipole moment now for the ν_1 symmetric frequency mode, otherwise inactive for gas-phase CO_2.

Figure 3.2 also shows the minimized structures for carbonate and bicarbonate possible adsorbed products associated with both ion-exchanges examined and using the same level of theory. The vibrational frequency calculations for carbonate/bicarbonate
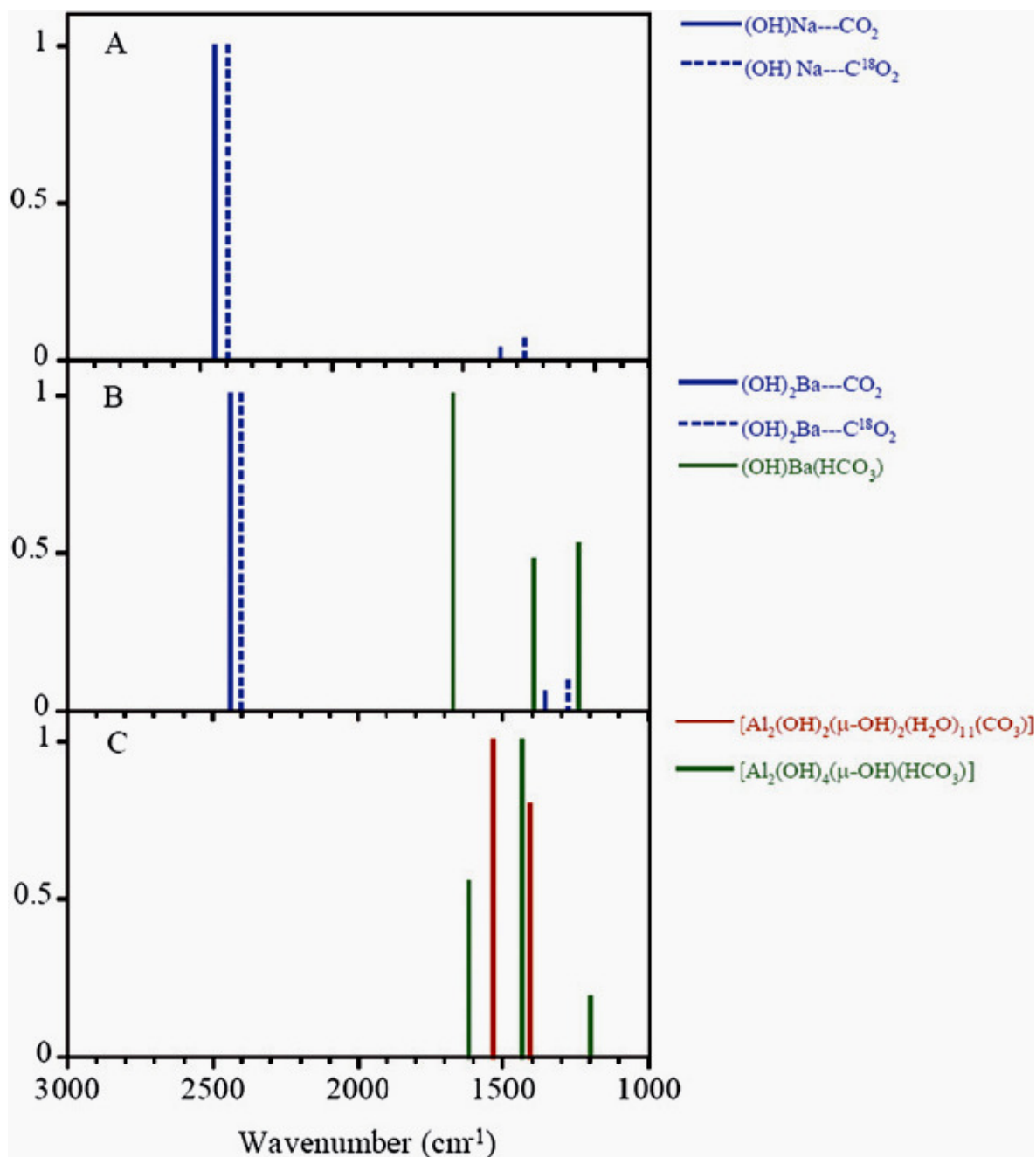
Figure 3.3: (A) represents the calculated spectra of (OH)Na clustered with CO_2 unlabeled (solid blue line) and labeled (dashed blue line); (B) represents the calculated spectra of $(OH)_2Ba$ clustered with CO_2 unlabeled (solid blue line) and labeled (dashed blue line) and the calculated spectra of $(OH)Ba(HCO_3)$ cluster (green solid line); (C) represents the vibrational modes for aluminum oxide carbonate complexes (red line) and aluminum oxide bicarbonate complexes (green line) as reported in literature.[106]

adsorbed to the surface show three bands, where the two higher frequencies correspond to the v_3 degenerate upon interaction with the surface and subsequent loss of symmetry; v_3 is, therefore, split into v_3(O-C-O)a and v_3(O-C-O)b bands. Table 3.2 gives the calculated v_1 and v_3 vibrational frequencies for carbonate. Frequencies were scaled using the 0.95 scaling factor, as discussed previously in the Experimental Section. In addition, it is important to point out that the presence of water solvating molecules decrease the interaction between the carbonate/bicarbonate species with the surface, which affects the geometry of the molecule. Consequently, the frequency difference for the v_3(O-C-O)a and v_3(O-C-O)b modes decreases as the carbonate/ bicarbonate interaction with the ions decrease.[100]

Table 3.1: Calculated frequencies (cm^{-1}) for the vibrational modes of $C^{16}O_2$ and $C^{18}O_2$.

Vibrational Mode	$C^{16}O_2$	$C^{18}O_2$
v_1	1335	1258
v_2	647	637
v_3	2408	2363

This is reflected in the frequencies for the v_3(O-C-O)a and v_3(O-C-O)b stretching modes. Vibrational frequency calculations of the isolated bihydrated barium carbonate cluster, $Ba(CO_3)_2 \cdot (H_2O)_2$, show that the v_3(O-C-O)$_a$ and v_3(O-C-O)$_b$ bands are 1124 and 1630 cm^{-1} respectively. This represents a reduction in the magnitude of the band split (Δv_3) from 615 cm^{-1} under dry conditions to 506 cm^{-1} in the presence of two solvating water molecules; this difference between the isolated $Ba(CO_3)_2$ and the $Ba(CO_3)_2 \cdot (H_2O)_2$ is

Table 3.2: Calculated scaled vibrational frequencies[a] for linear CO_2 complexes, {(OH)Na/CO_2 and (OH) Ba/CO_2} and carbonate and bicarbonate complexes {Na_2CO_3, $BaCO_3$, $Na(HCO_3)$ and $Ba(OH)(HCO_3)$}.

Vibrational Modes	(OH)Na$\cdots$CO$_2$	(OH)$_2$Ba$\cdots$CO$_2$
ν_1	1356 [a]	1354
	(1268) [b]	(1276)
ν_2(O-C-O)a	643	645
	(634)	(636)
ν_2(O-C-O)b	643	641
	(632)	(631)
ν_3	2442	2439
	(2393)	(2402)

Vibrational Modes	Na$_2$CO$_3$	BaCO$_3$
ν_1	945	892
ν_3(O-C-O)a	1263	1010
ν_3(O-C-O)b	1583	1625

Vibrational Modes	Na(HCO$_3$)	Ba(OH)(HCO$_3$)
ν_1	1001	1241
ν_3(O-C-O)a	1409	1395
ν_3(O-C-O)b	1790	1668

[a] Calculated scaled vibrational frequencies in cm^{-1} for $C^{16}O_2$ complexes.

[b] Values in parentheses represent the calculated scaled vibrational frequencies[a] for the analogous $C^{18}O_2$ complexes.

attributed to the carbonate ion relaxing to a "less coordinated" state and confirms previous observations on different surfaces.[101, 106] If carbonate/bicarbonate species are produced, analogous ν_3(O-C-O)a and ν_3(O-C-O)b bands are expected to be observed in the experimental infrared data.

Figure 3.3 summarizes and provides in stick format the vibrational frequencies calculated from several of the cluster models. These data are used as a guide for the interpretation of the experimental data. It is clear from Fig. 3.3 that bicarbonate products have an intense band below 1500 cm^{-1}. In addition, Fig. 3.3C shows calculated frequencies for vibrational modes of carbonate and bicarbonate coordinated to aluminum oxide binuclear clusters. These frequencies are taken from Baltrusaitis et al. and are used to interpret the data for nanocrystalline zeolites spectra (vide infra).[101, 106]

3.4.2 Transmission FTIR Spectroscopy of Carbon Dioxide
Adsorbed in NaY, BaY and Nano NaY Under Dry
Conditions

Figure 3.4(a), 3.4(b), 3.4(c) shows the IR spectra collected upon adsorption of $C^{16}O_2$ in all three zeolites, NaY, BaY and nano NaY. Adsorption of carbon dioxide on all the three surfaces results in the formation of an intense adsorption band in the 2350 cm^{-1} region and formation of other smaller peaks both at higher and lower wavenumber regions. All the peaks grow in intensity with increasing carbon dioxide pressures. These peaks have been discussed in detail below as a comparison for the three surfaces.

Before moving on to the comparison, we discuss here the intense absorption band at 2351 cm^{-1}, which is assigned to the asymmetric stretching mode (ν_3) of CO_2. Figure 3.4(d) shows the CO_2 adsorption on NaY zeolite as a function of pressure in the blown up

spectral region between 2000 and 2600 cm^{-1}. The ν_3 peak is shifted from the gas-phase value of 2347 cm^{-1} as suggested by the calculations due to the interaction with the exchangeable cation. This band increases in intensity as a function of $C^{16}O_2$ pressure. As the equilibrium pressure (P_{eq}) of $C^{16}O_2$ increases, two smaller bands grow in on the low and high frequency side of the ν_3 peak. These bands are most distinct at the highest CO_2 pressures. Comparison with previous reports of carbon dioxide adsorption in zeolite materials suggests that absorptions at 2405 cm^{-1} and 2288 cm^{-1} are due to the combination modes of the ν_3 mode with the framework M---O stretching modes of the zeolite as observed for NaZSM.[107, 108]

Figure 3.5 shows an expanded spectral region, from 1200 to 4000 cm^{-1} for $C^{16}O_2$ adsorbed in all the three zeolites at a pressure of 20 Torr. As seen in Figure 3.5, several more bands are present in the spectrum. A sharp peak is observed near 1382 cm^{-1} due to the symmetric stretch of CO_2. As already noted, in the gas-phase this peak is IR inactive. However, this peak becomes IR active when CO_2 is adsorbed in the zeolite due to interaction with the exchangeable cation, and the symmetry is lowered upon interaction because of two unequal bond lengths of the C—O bond, as also indicated by theoretical calculation, giving rise to an IR active mode. Additional bands are observed in the spectrum and are assigned to other vibrational modes of adsorbed carbon dioxide, some of which are overtones and some are combination bands. One of them is a small peak observed around 1276 cm^{-1} for these zeolites, which is a combination band arising from Fermi resonance between the Raman-active ν_1 symmetric vibration and the overtone of the bending mode ν_2 ($2\nu_2$). As already discussed, due to the reduction in symmetry of carbon dioxide on interaction with the zeolite surface this mode becomes IR active as
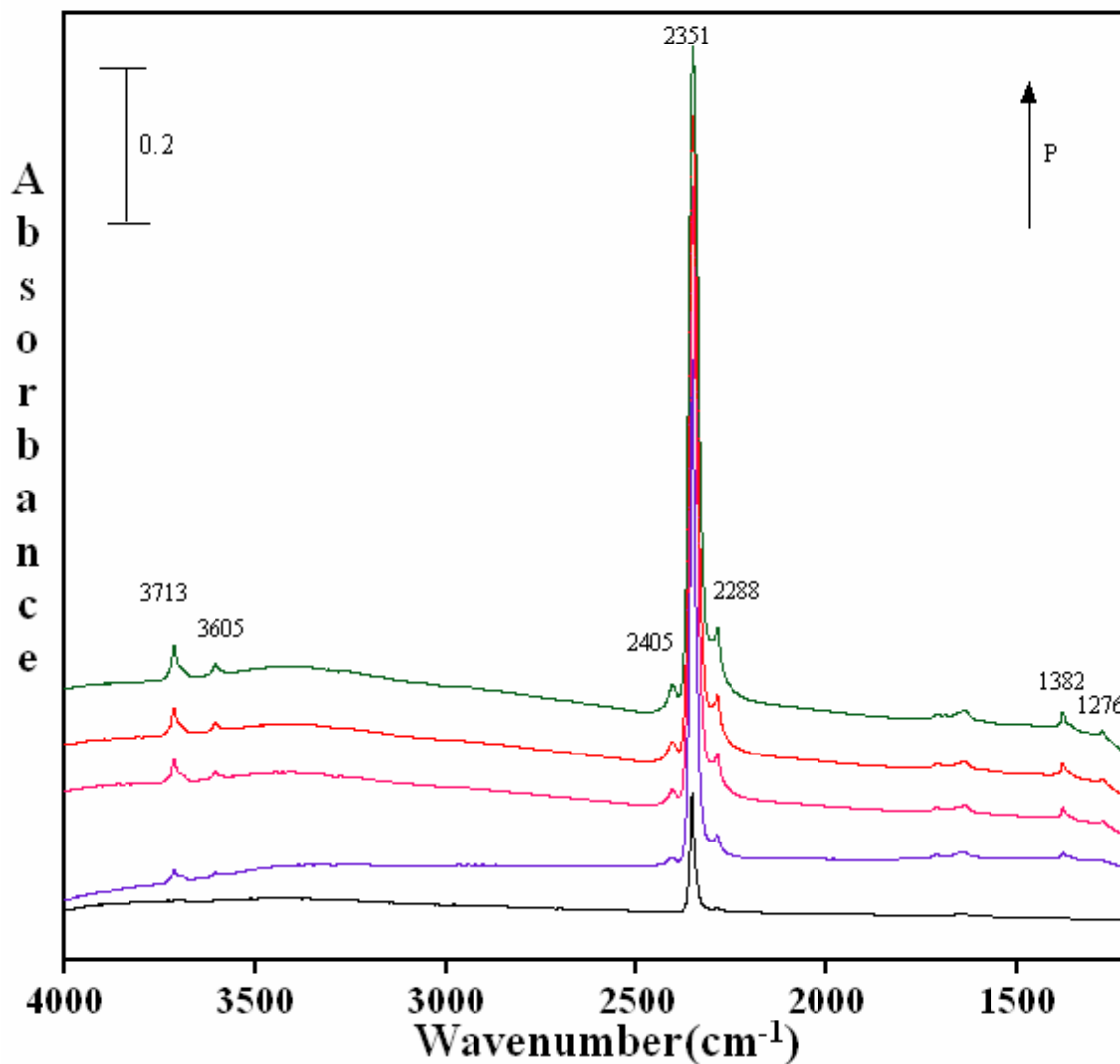
Figure 3.4 (a)

Figure 3.4: (a) FTIR spectra of adsorbed $C^{16}O_2$ in dry commercial NaY zeolite as a function of pressure (P = 1.030, 5.200, 10.6, 14.2 and 20 Torr).; (b) FTIR spectra of adsorbed $C^{16}O_2$ in BaY zeolite as a function of pressure (P = 1.018, 5.012, 10.5, 14.2 and 19.8 Torr).; (c) FTIR spectra for of adsorbed $C^{16}O_2$ as a f(P) on nano NaY. (P_{eq} = 1.015, 5.203, 10.6, 14.4 and 19.8 Torr); (d) FTIR spectra of adsorbed $C^{16}O_2$ in dry commercial NaY zeolite as a function of pressure. The spectral region showing the ν_3 mode of adsorbed carbon dioxide region.
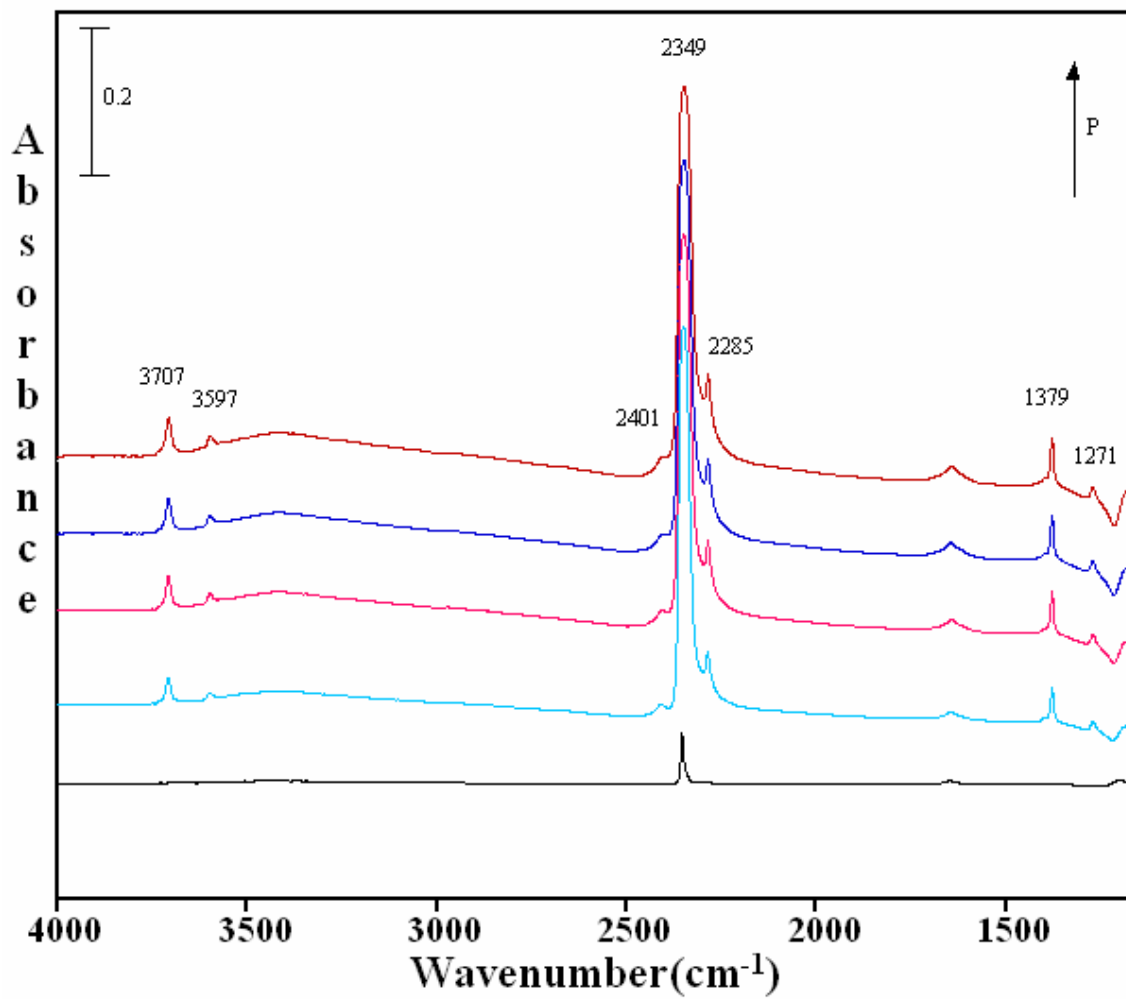
Figure 3.4 (b)

(Figure 3.4 continued)
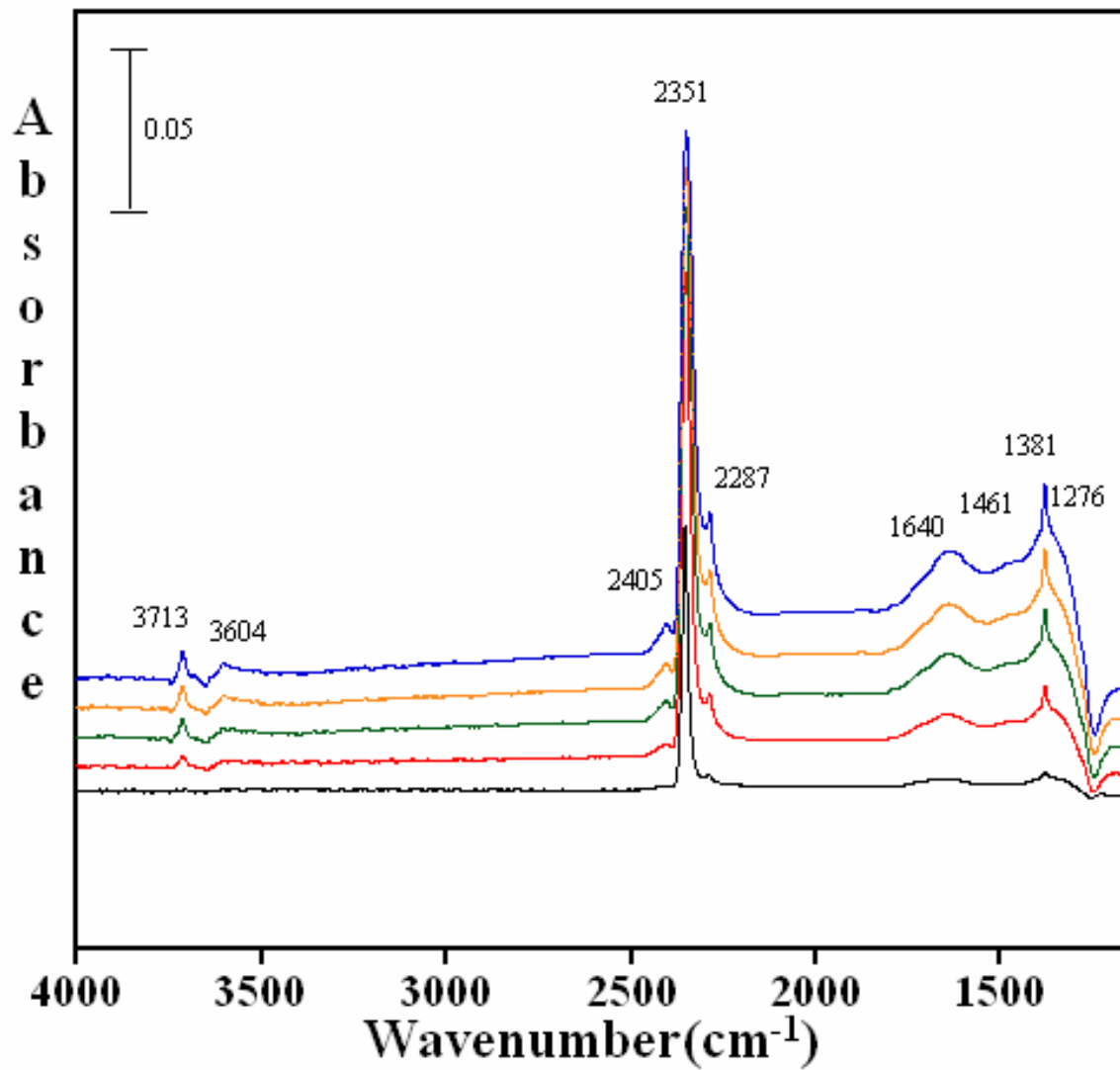
Figure 3.4 (c)

(Figure 3.4 continued)
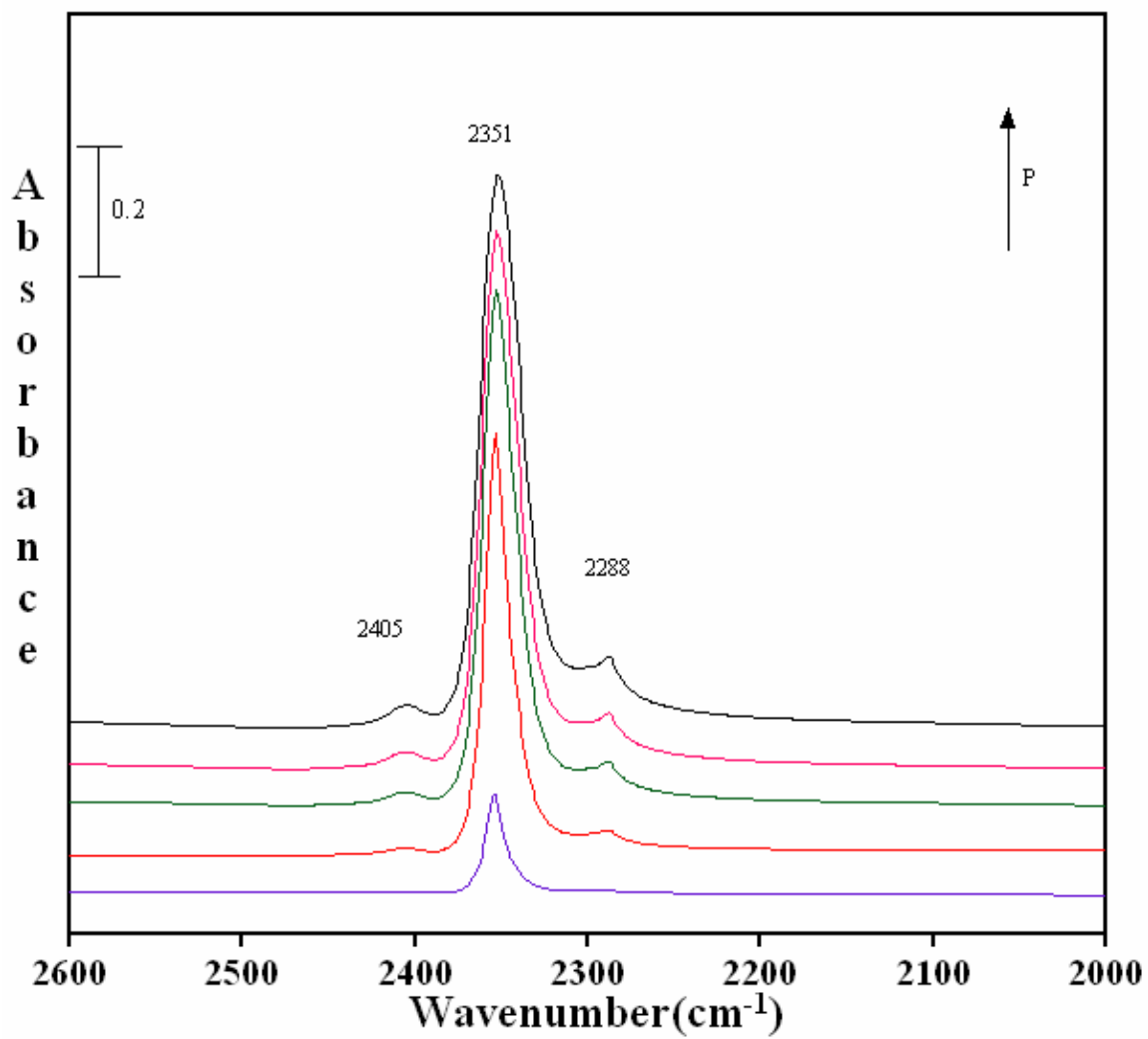
Figure 3.4 (d)

(Figure 3.4 continued)

well. The combination bands of $\nu_3 + \nu_1$ and $\nu_3 + 2\nu_2$ at 3713 and 3605 cm^{-1} are also present and have been reported earlier in the literature.[108] These experimental frequencies are summarized in Table 3.3.

In addition to C^{16}O$_2$ adsorption in NaY, Figure 3.5 shows C^{16}O$_2$ adsorption in BaY and nano NaY zeolites. Interestingly, the ν_3 vibrational mode for the commercially available NaY as well as nanocrystalline NaY zeolite is observed at exactly the same wavenumber but for BaY it appears at a slightly different frequency. As can be seen, the experimental ν_3 frequency appears at 2351 cm^{-1}, 2349 cm^{-1} and 2351 cm^{-1} for NaY, BaY and nano NaY, respectively. This relatively small shift in the ν_3 mode for the BaY zeolite as compared to the NaY zeolites is in agreement with the calculations.

Besides the intense ν_3 vibrational band, a number of other vibrational bands are observed in the BaY and nano NaY spectra that are associated with C^{16}O$_2$ adsorbed inside the zeolite cage. These include the ν_1 symmetric vibration and several combination and overtone vibrations.[107] The vibrational frequencies for these modes are given in Table 3.3. Of particular interest are the differences observed in these spectra for the different zeolite materials. In comparing the 1200 to 1800 cm^{-1} spectral region for the NaY and nano NaY zeolites, there is evidence for additional bands observed in nano NaY spectra. Figure 3.6 shows the IR spectra collected upon adsorption of C^{16}O$_2$ in nano NaY zeolite as a function of pressure in the spectral region between 1200 and 4000 cm^{-1}. In particular, for nano NaY there are several broad features near 1640, 1461 and 1381 cm^{-1}. As the carbon dioxide equilibrium pressure increases, one can with clarity distinguish these broad features. The FWHM (full width half maximum) for these peaks are greater than the other absorption bands in the spectrum by more than 20 cm^{-1}. Although the peak

at 1381 cm^{-1} has some contribution to the symmetric stretching mode as already discussed, there is a broad band underlying the sharper feature.

Based on earlier studies, these new absorption bands are proposed to be due to the formation of bicarbonate and carbonate species on extra framework aluminum (EFAL) sites [47, 51] known to be present on the external surface of nanocrystalline zeolites. As has been shown previously, nanocrystalline zeolites not only possess high surface area but in fact have a high concentration of reactive surface sites because of the increased external surface area due to the smaller particle size. EFAL sites are the most notably active catalytic sites in nanocrystalline zeolites that cause these zeolites to demonstrate higher activity as compared to commercial zeolites with large particle size. For example, it has been previously shown that molecules, e.g. NO_2, can adsorb to these sites yielding surface complexes unique to nanocrystalline NaY zeolite.[52] We propose here that these EFAL sites play a similar role in the adsorption of CO_2 in the nanocrystalline NaY zeolite and result in the formation of carbonate and bicarbonate species.

Baltrusaitis et al.[101, 106] have calculated the vibrational frequencies of bicarbonate and carbonate in binuclear aluminum oxide cluster complexes and have shown these to be in good agreement with the experimental IR frequencies measured for these same species adsorbed on aluminum oxide surfaces. The results of these calculations are summarized in Figure 3.3C. It is proposed that the absorption bands seen in the spectral region from 1200 to 1800 cm^{-1} are a result of carbon dioxide uptake on the EFAL sites, and the formation of carbonate and bicarbonate species on these sites can be explained as being similar to that observed on aluminum oxide surfaces. Bicarbonate species formation can be explained by the reaction mechanism (Scheme 2) already proposed.[106]

Table 3.3: Summary of experimental vibrational frequencies[a] for adsorbed $C^{16}O_2$ (and $C^{18}O_2$)[b] and carbonate/bicarbonate in different zeolites materials under dry conditions as well as in presence of co-adsorbed water.

Vibrational Modes	Gas Phase[108]	NaY	NaY/H_2O[c]	BaY	BaY/H_2O[c]	Nano NaY	Nano NaY/H_2O[c]
CO_2 linear complexes							
ν_1	1388.3	1382	1382	1379	1382	1381	1381
ν_2	667.3	-	-	-	-	-	-
ν_3	2347.3	2351 (2318)	2351	2349 (2318)	2349 (2315)	2351 (2319)	2351 (2316)
$\nu_3+\nu_1$	-	3713 (3632)	3712	3707 (3626)	3710	3713	3714
$\nu_3+2\nu_2$	-	3605 (3527)	3605	3597 (3520)	3604	3604	3604
$2\nu_2$	-	1276 (1227)	1276	1271 (1222)	1268	1276	-
$\nu_3+\nu(M{-}O)$	-	2405 (2289)	2403	2401 (2367)	2400 (2349)	2405 (2382)	2402
$\nu_3-\nu(M{-}O)$	-	2288 (2253)	2288	2285 (2253)	2285 (2249)	2287 (2253)	2287 (2252)
Carbonate and Bicarbonate							
ν_1	-	-	-	-	-	1640 (1631)	1639
ν_3(O-C-O)a		-	-	-	1448 (1439)	1461 (1368)	1408
ν_3(O-C-O)s		-	-	-	1382 (1377)	1381 [d]	1381 [d]

[a] Experimental frequencies in cm^{-1}.

[b] $C^{18}O_2$ (1 Torr) frequencies in parentheses.

[c] In the presence of co-adsorbed water.

[d] This absorption band is broad and underneath the sharper feature in the spectrum (see Figure and text for details).
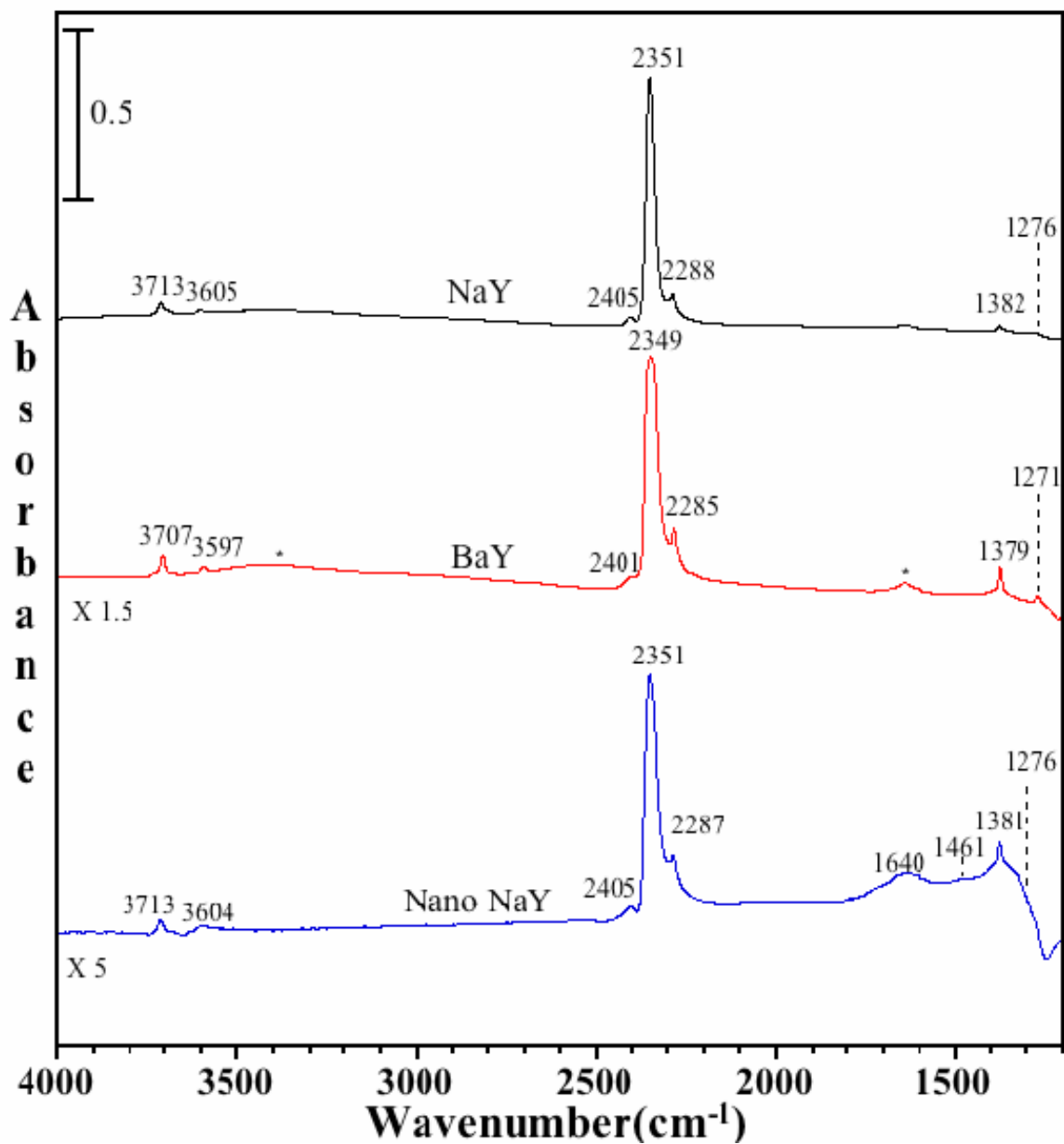
Figure 3.5: FTIR spectra of adsorbed $C^{16}O_2$ on dry NaY, BaY and nano NaY zeolite at a CO_2 pressure of 20 Torr and temperature of 296 K. The asterisks in the BaY spectrum denote absorptions due to the stretching and bending modes of a small amount of adsorbed water.

According to this mechanism, CO_2 is pre-adsorbed on the surface of the zeolite and is followed by intermolecular proton transfer by the neighboring hydroxyl groups of the extra framework aluminum sites (EFAL), represented by M, resulting in bicarbonate

formation. Similar reactions are likely to occur on the EFAL sites on the nanocrystalline external surface.[101, 106]

As isotope-labeling experiments can provide additional information about the adsorbed species, adsorption of ^{18}O- labeled CO_2 on all zeolites was also investigated. It

(2)
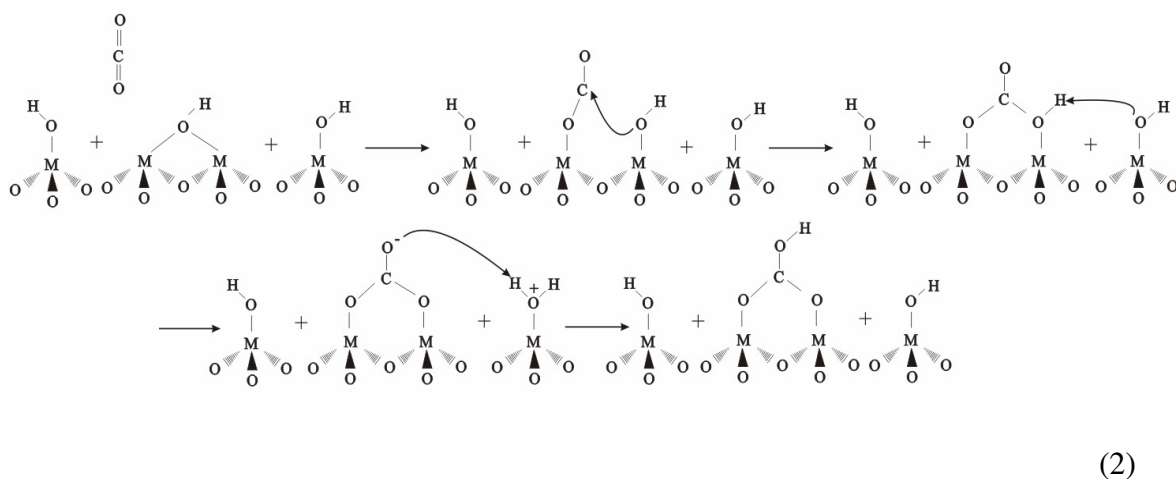
is important to note that the pressure of carbon dioxide used in these isotope studies is 1 Torr for both $C^{16}O_2$ and $C^{18}O_2$. An example of the spectra collected for the isotope data is shown in Figure 3.6. The spectra shown are for carbon dioxide adsorption in BaY zeolite with $C^{18}O_2$ and $C^{16}O_2$. It is seen that there are some shifts in the peak positions to lower wavenumbers for $C^{18}O_2$, as expected. These shifts are consistent with the quantum chemical calculations for CO_2 interaction with the cation, as shown in complex (3.2(a)) and (3.2(b)), as well as in the calculated frequencies.
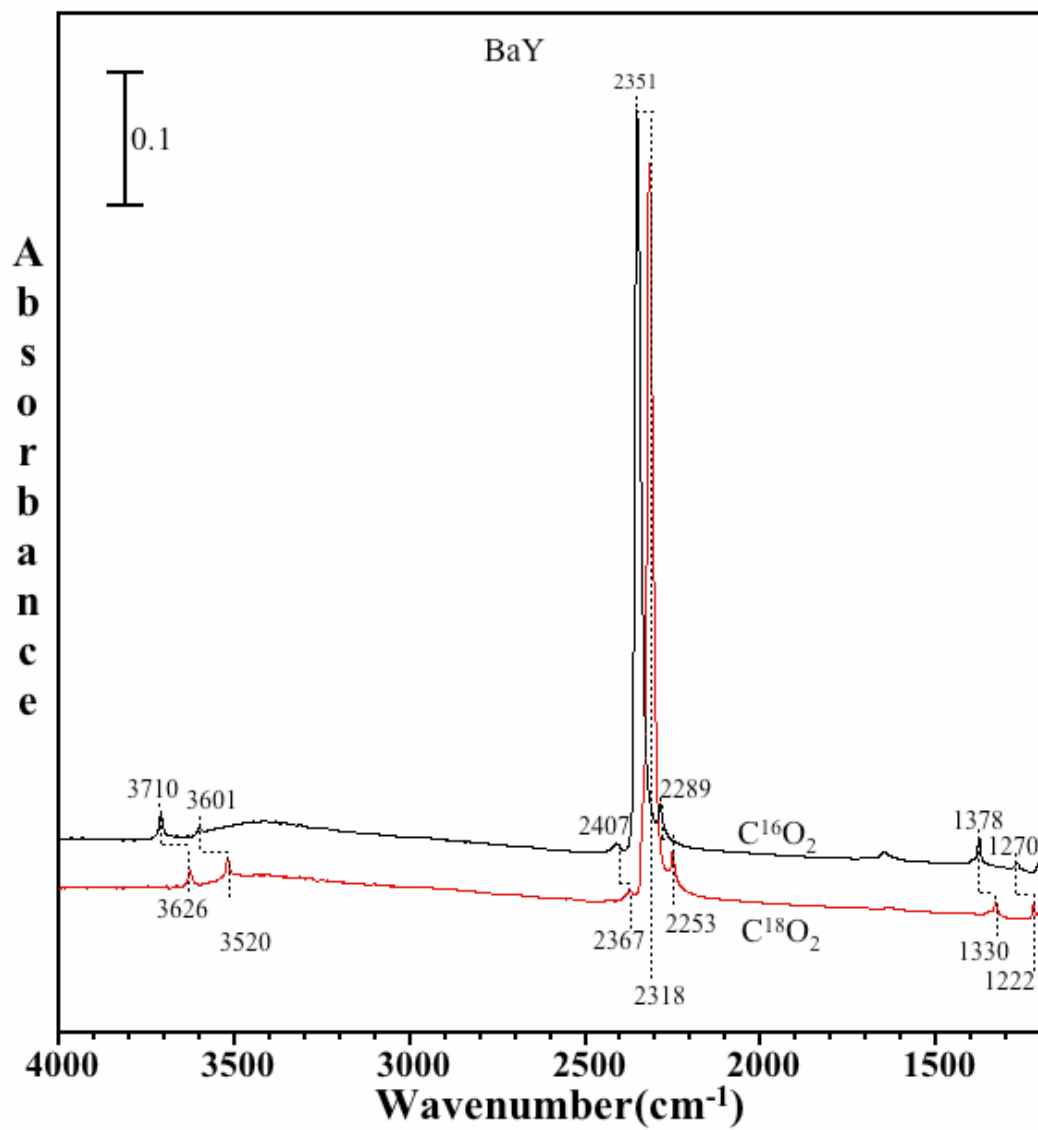
Figure 3.6: FTIR spectra of adsorbed $C^{16}O_2$ (black) and adsorbed $C^{18}O_2$ (red) on BaY zeolite at a pressure of 1 Torr and temperature of 296 K.

3.4.3 Transmission FTIR Spectroscopy of Carbon Dioxide Adsorbed in NaY, BaY and Nano NaY in the Presence of Co-Adsorbed Water

CO$_2$ adsorption was carried out on zeolite surfaces, as a function of increasing

pressure of CO$_2$ after pre-adsorbing water in the zeolite at 1% relative humidity.
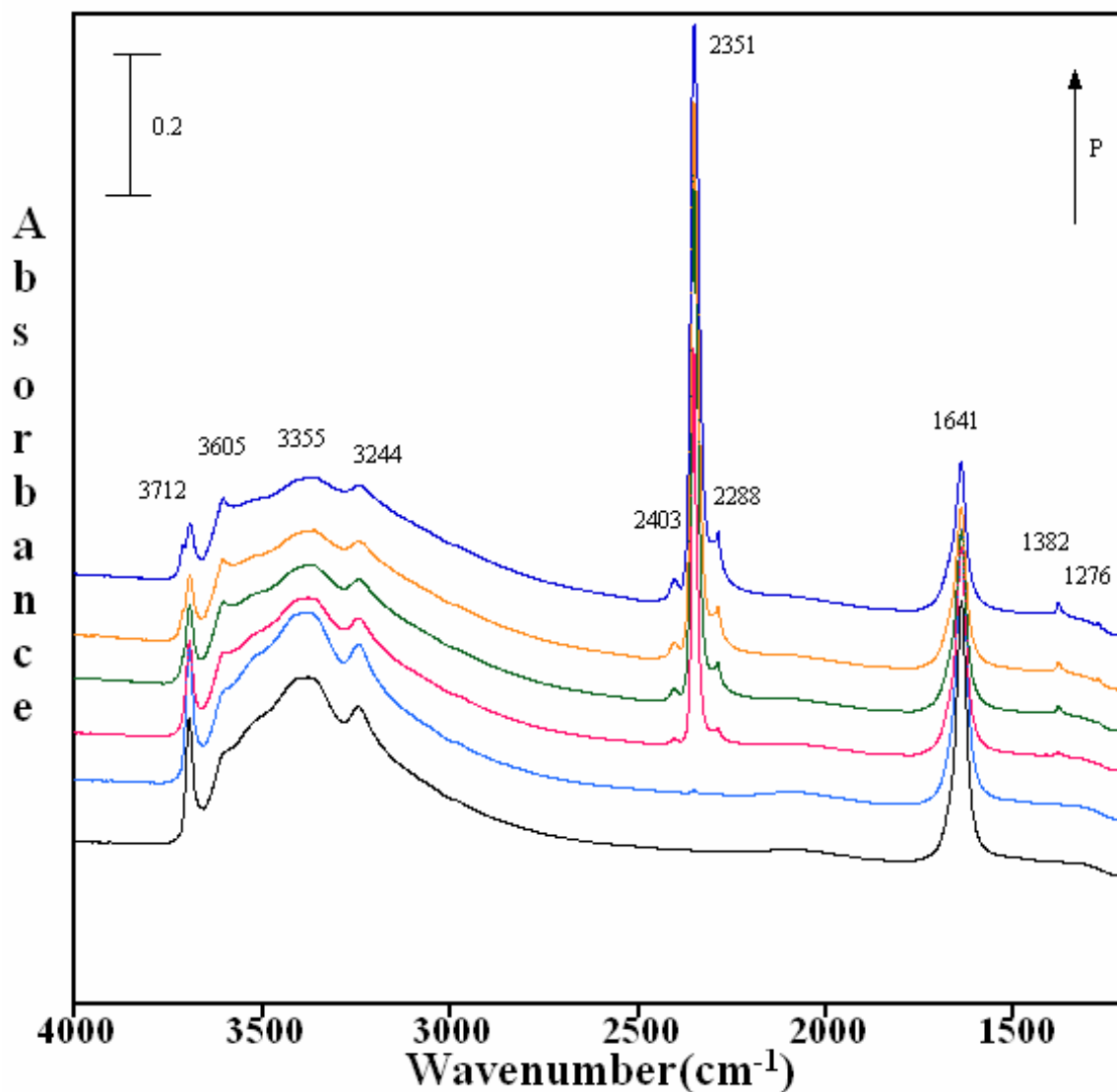
Figure 3.7 (a)

Figure 3.7: (a) FTIR spectra of adsorbed $C^{16}O_2$ in wet commercial NaY zeolite as a function of increasing pressure of CO_2; (b) FTIR spectra of adsorbed $C^{16}O_2$ in wet BaY zeolite as a function of pressure; (c) FTIR spectra for of adsorbed $C^{16}O_2$ as a f(P) in wet nano NaY.
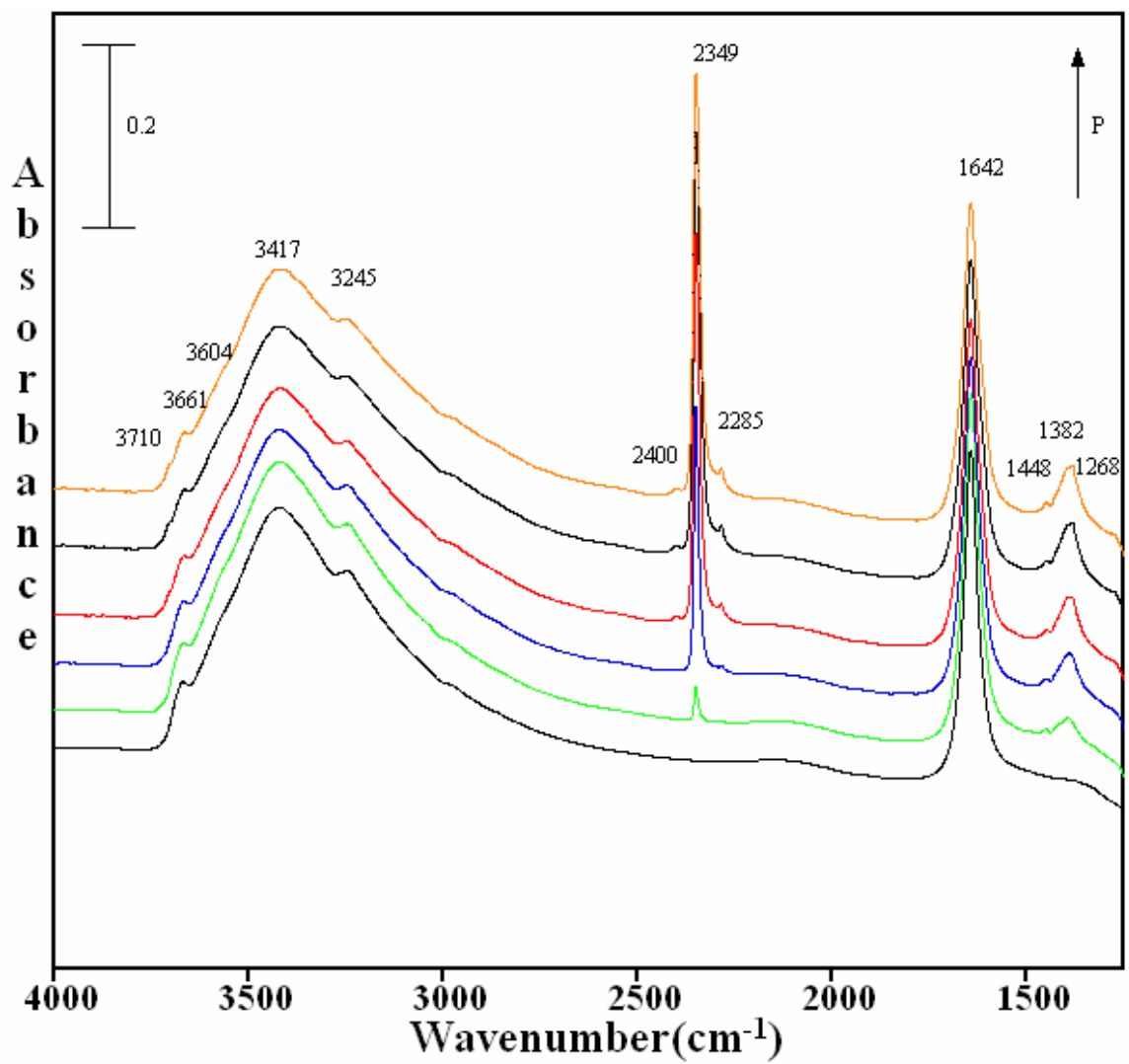
Figure 3.7 (b)

(Figure 3.7 continued)
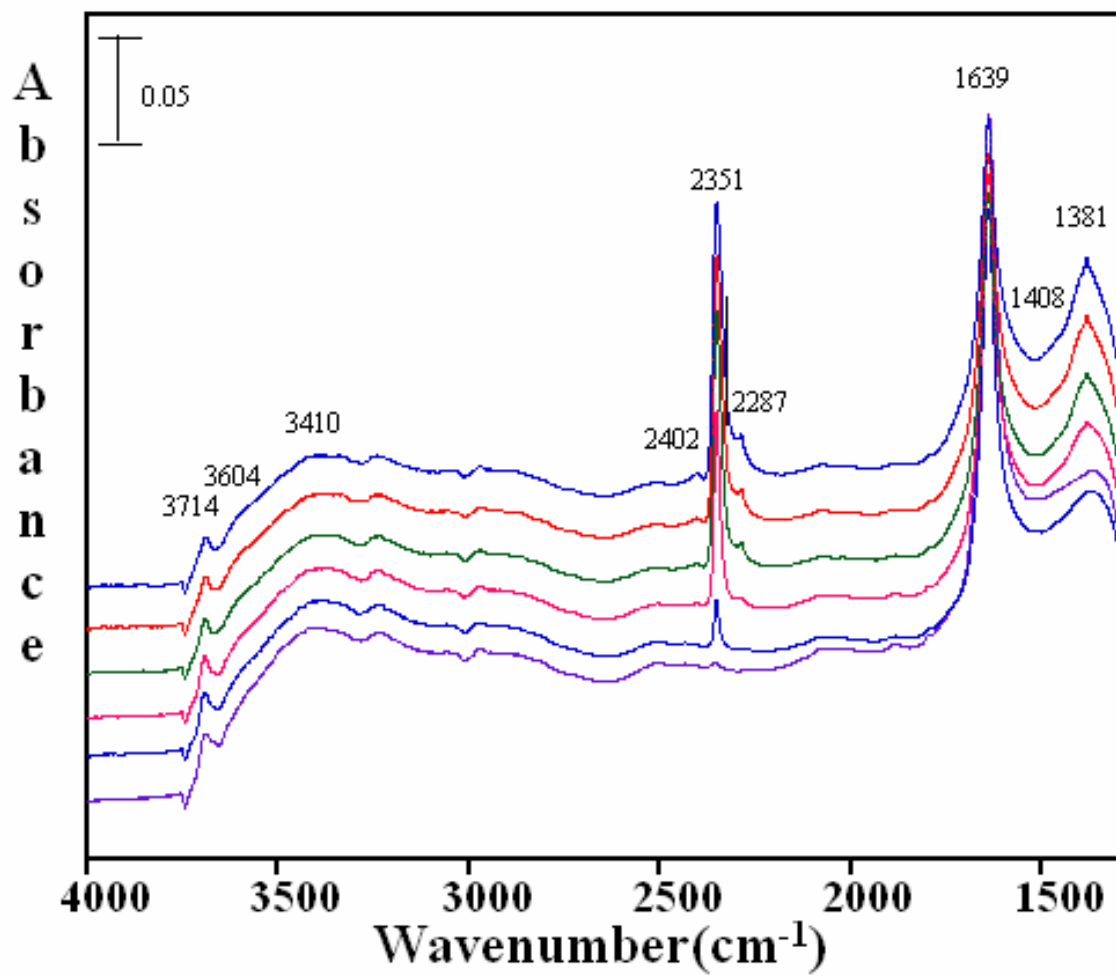
Figure 3.7 (c)

(Figure 3.7 continued)
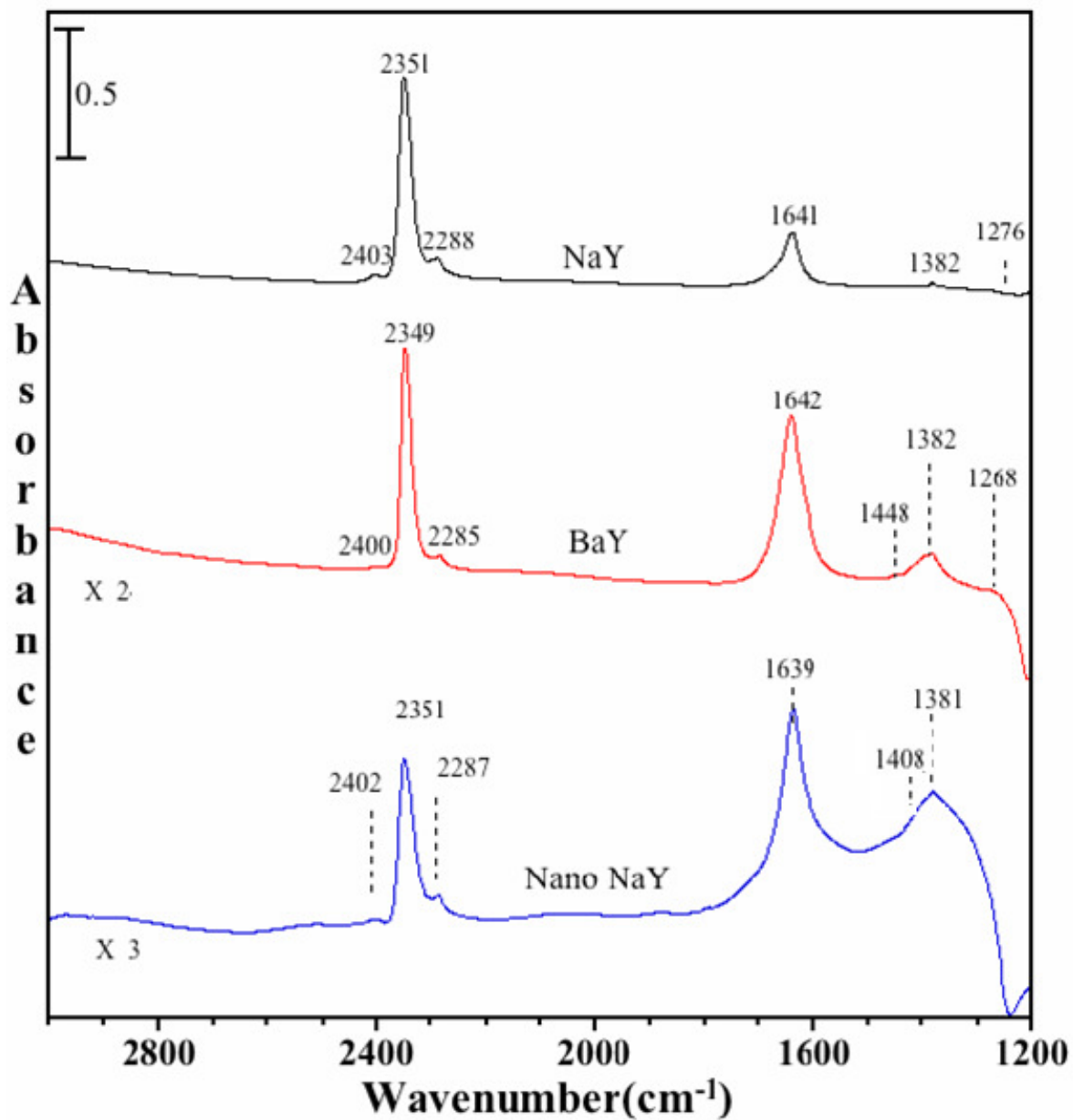
Figure 3.8: FTIR spectra of adsorbed $C^{16}O_2$ in the presence of co-adsorbed water in NaY, BaY and nano NaY zeolite at a CO_2 pressure of 20 Torr and temperature of 296 K.

Following the introduction of 1% RH at 296 K, the gas-phase water was pumped out leaving adsorbed water in the zeolite pores. Figure 3.7(a), 3.7(b), 3.7(c) shows the IR

spectra collected upon adsorption of $C^{16}O_2$ in wet surfaces of all the three zeolites. Evidence for adsorbed water is seen in all the spectra with an absorption band near 1640 cm^{-1} and 3300 cm^{-1} due to the bending and stretching modes of adsorbed water. These spectra are discussed along with their comparison for CO_2 adsorption below.

Figure 3.8 shows the FTIR spectra collected upon adsorption of $C^{16}O_2$ and co-adsorbed water on NaY, BaY and nano NaY zeolite. In all the three zeolites, peaks due to molecularly adsorbed CO_2 were observed similar to what is observed for CO_2 adsorption in the dry zeolite. The frequencies of these absorption bands are given in Table 3.3. However, there is an overall decrease in the integrated absorbance of these bands for experiments with co-adsorbed water suggesting that adsorption of water blocks the zeolite pores. For example, at similar pressures, in the presence of water there is *ca.* 20% decrease in the integrated area of the ν_3 band of adsorbed carbon dioxide. This decrease in integrated area suggests that co-adsorbed water inhibits carbon dioxide adsorption and blocks sites for adsorption.

As noted previously, we are interested in the differences in carbon dioxide adsorption in the different zeolite materials. For these experiments, in the presence of co-adsorbed water, BaY shows new absorption bands in the region below 1500 cm^{-1}. Besides the absorption band at 1642 cm^{-1} due to adsorbed water, several other broad bands also become present. A broad band at around 1448 cm^{-1}, with a FWHM (full width half maximum) of around 45 cm^{-1} appears upon adsorption of CO_2 in the presence of co-adsorbed water, the band at 1379 cm^{-1} is also quite broad. We suggest that these absorptions, some of which might be hidden under the intense bending mode of adsorbed water, are due to the presence of bicarbonate. Water most likely activates BaY zeolite for
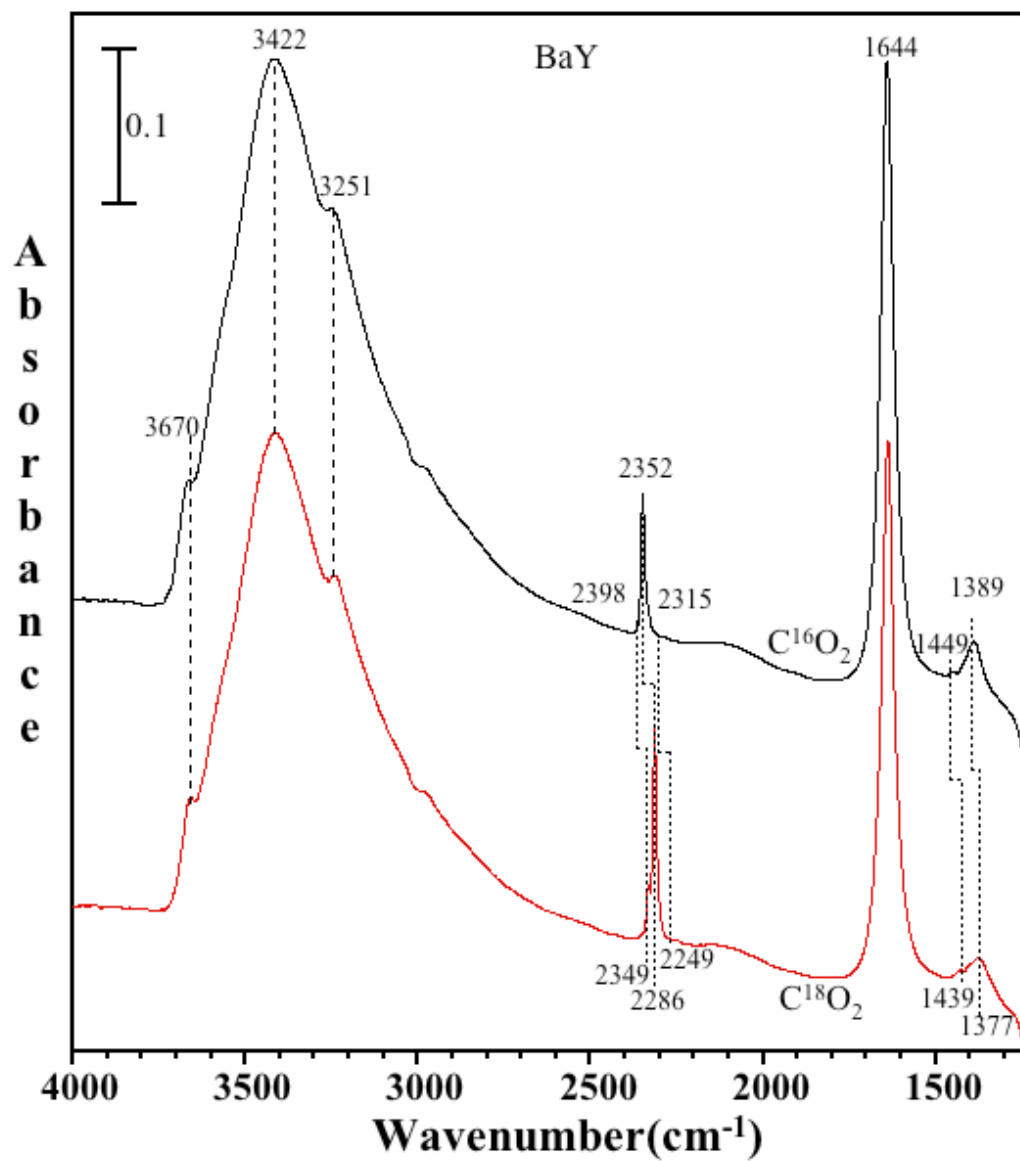
Figure 3.9: FTIR spectra of adsorbed $C^{16}O_2$ (black) and adsorbed $C^{18}O_2$ (red) in the presence of co-adsorbed water on BaY zeolite at a pressure of 1 Torr and temperature of 296 K.

the formation of bicarbonate species. The reason for this difference lies in the

exchangeable ion, where the polarizability of Ba^{2+} (in BaY zeolite) is greater than that of

Na^+ cation (in NaY zeolite). Figure 3.9 shows the spectra of both $C^{16}O_2$ and $C^{18}O_2$ on BaY zeolite in the presence of co-adsorbed water. The $C^{18}O_2$ and $C^{16}O_2$ pressure is 1 Torr in both the cases. Upon absorption of ^{18}O-labeled carbon dioxide on wet zeolites surfaces, a red shift is observed in all peaks with the exception of the peaks from adsorbed water, further providing evidence that carbonate is formed in BaY in the presence of co-adsorbed water.

3.5 Conclusions

The adsorption of CO_2 was carried out on zeolite Y materials (NaY, BaY and nano NaY) both under dry conditions as well as in presence of co-adsorbed water. Quantum chemical calculations were also performed. Both the theoretical calculations and experimental data provide complementary information and lead to a better understanding of adsorbed CO_2 in these zeolite materials. Although CO_2 adsorbs molecularly, as in a linear bonded complex, in all three zeolites, differences are observed between the various zeolite materials with the formation of carbonates and bicarbonates depending upon the experimental conditions, dry versus wet, the exchangeable cation and, very interestingly, the zeolite particle size. This carbonate/bicarbonate species formation on the external surface sites of nano NaY zeolite upon CO_2 adsorption, suggests that nanocrystalline zeolite adsorption sites are efficient in the conversion of carbon dioxide. These studies show that zeolites can store carbon dioxide in the internal pores. Also, we have seen the bicarbonate formation in BaY zeolite when adsorbed water was also present, which suggests that water activates BaY active sites for the formation of bicarbonate species. Further studies should investigate how zeolites may be used to

convert carbon dioxide to more useful products such as methanol. Because of the high external surface area and active sites present on the external surface, nanocrystalline zeolites, in particular, may be useful zeolite materials in CO_2 recycling and conversion processes.

3.6 Acknowledgements

CHAPTER IV

FTIR SPECTROSCOPY COMBINED WITH ISOTOPE LABELING TO INVESTIGATE ADSORBED BICARBONATE AND CARBONATE FORMATION FOLLOWING REACTION OF CARBON DIOXIDE WITH ALUMINUM BASED OXIDE SURFACES

4.1 Abstract

In this study, FTIR spectroscopy along with isotope-labeling experiments is used to investigate carbon dioxide adsorption on aluminum based surfaces. In particular, CO_2 adsorption on mixed phase nanoparticulate rod shaped alumina whiskers (boehmite and bayerite) is compared with spherical 10 nm alumina (gamma Al_2O_3) at 296 K. The reaction of carbon dioxide with these oxide based surfaces result in the formation of both adsorbed bicarbonate and carbonate species. In the case of alumina whiskers, there was an extensive carbonate formation whereas for 10 nm alumina mainly bicarbonate product formation is observed. This can be explained on the basis of coordination geometry of these surfaces. This difference in the aluminum coordination (octahedral vs. tetrahedral) in both the nanomaterials is highlighted as these sites play a significant role in their reactivity and product formation.

4.2 Introduction

As discussed earlier, carbon dioxide is the fourth most abundant gas in the atmosphere, uniformly distributed over the Earth's surface with a concentration of about 385 ppm.[6] CO_2 plays an important role in global warming; therefore, carbon dioxide

storage and conversion are topics of great importance to the scientific community and the public. Recent studies indicate that nanomaterials have the potential to adsorb and convert CO_2 into more useful products. In addition, studying such (metal oxide-CO_2) systems can give us an insight into the atmospheric chemistry at such interfaces. Therefore, the surface reactions of carbon dioxide are of significance for many reasons; both for sequestering and environmental perspective.

Aluminum oxides and hydroxides are important environmental interfaces. [7, 54, 55, 109] Therefore, the reaction chemistry that occurs at the oxide interface needs to be understood. Bauxite is an important source of aluminum; aluminum not only exists as simple oxides but also as hydrates of alumina. As discussed previously, natural Al_2O_3 exists in many phases namely alpha, chi, kappa, gamma, delta, theta and eta. Similarly gibbsite, boehmite, diaspore, nordstrandite and bayerite are the principal hydrates of alumina.[59-61] The surface structure of these oxides and hydroxide nanomaterials is related to bulk crystal structure and thus it is determined by the arrangement of the Al^{3+} ions in the oxygen lattice. This also means that the type and number of hydroxyl groups which are preferentially exposed as surface sites depends on the crystal planes and structure.[110] In the case of bayerite and boehmite (γ -AlO_2H and $Al(OH)_3$) Al^{3+} ions occupy most of the octahedral holes in the ccp O^{2-} array and thus possess the octahedral coordination mainly. Whereas, in the structure of aluminum oxide (γ - Al_2O_3), Al^{3+} ions occupy both octahedral and tetrahedral holes of the ccp O^{2-} array.[111-114]

Alumina is an amphoteric oxide and it not only possesses acidic sites but also basic sites. CO_2 adsorption on basic sites usually forms carbonate species, and CO_2 adsorption on comparatively acidic sites forms bicarbonate pecies.[61, 64, 115-118] Literature

studies of CO_2 adsorption on metal oxide surfaces under dry condition, on metal oxides surfaces, result in the formation of adsorbed carbonates, bicarbonates, and formates as well as bent CO_2 species.[61-66, 115, 116, 119] Recently, Baltrusaitis et al. performed quantum chemical calculations along with FTIR isotope-labeling experiments to provide information about the overall adsorption mechanism of CO_2 on the metal oxide surface and the molecular structure of the adsorbed products, which resulted in the formation of bicarbonate species.[106] Under dry conditions, the adsorption of CO_2 on aluminum oxide surfaces has been well studied whereas the adsorption of CO_2 at the different aluminum based interfaces has not been studied in details.

In this study, adsorption of CO_2 was investigated on aluminum based nanomaterials under dry conditions. FTIR spectroscopy was used to probe adsorbed CO_2. In particular, we present in this study: FTIR experimental data for CO_2 adsorption in two different unique high external surface area nanoscale aluminum surface materials, namely alumina whiskers and 10 nm alumina, including isotope data to support vibrational mode assignments. Differences are observed between the different materials investigated, with the formation of carbonates and bicarbonates depending upon the coordination geometry of aluminum. The Lewis acid Al^{3+} sites play an important role in the preferential product determination. As a step towards better understanding the surface chemistry of these hydroxylated metal oxide surfaces under ambient conditions, we have investigated the adsorption of carbon dioxide on these nanomaterials.
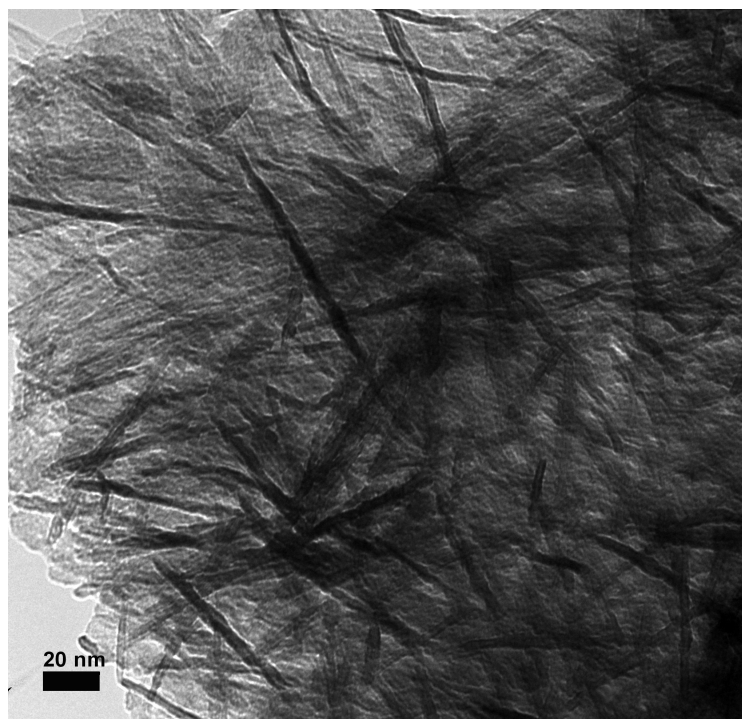
(a)
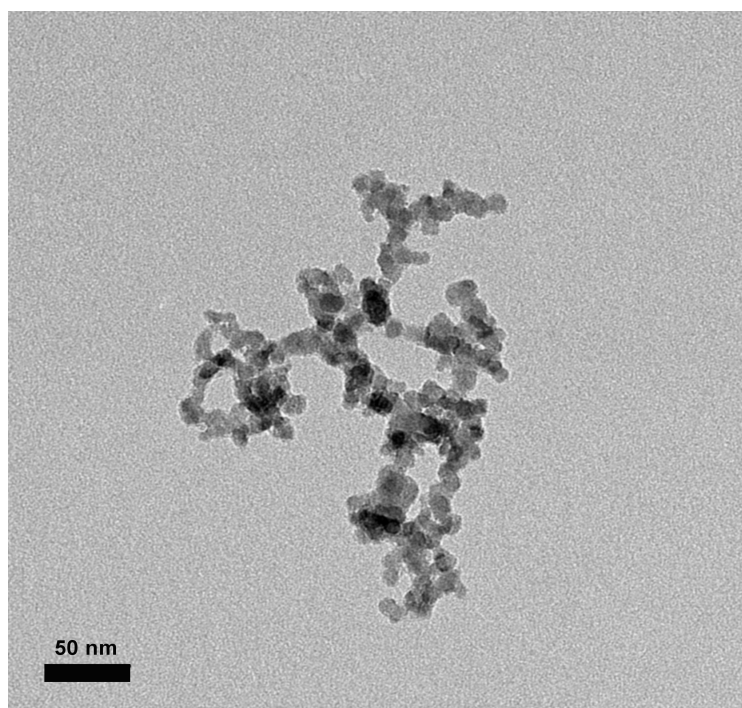
(b)

Figure 4.1: TEM images of aluminum based materials used in the study. (a) alumina whiskers and (b) 10 nm alumina.
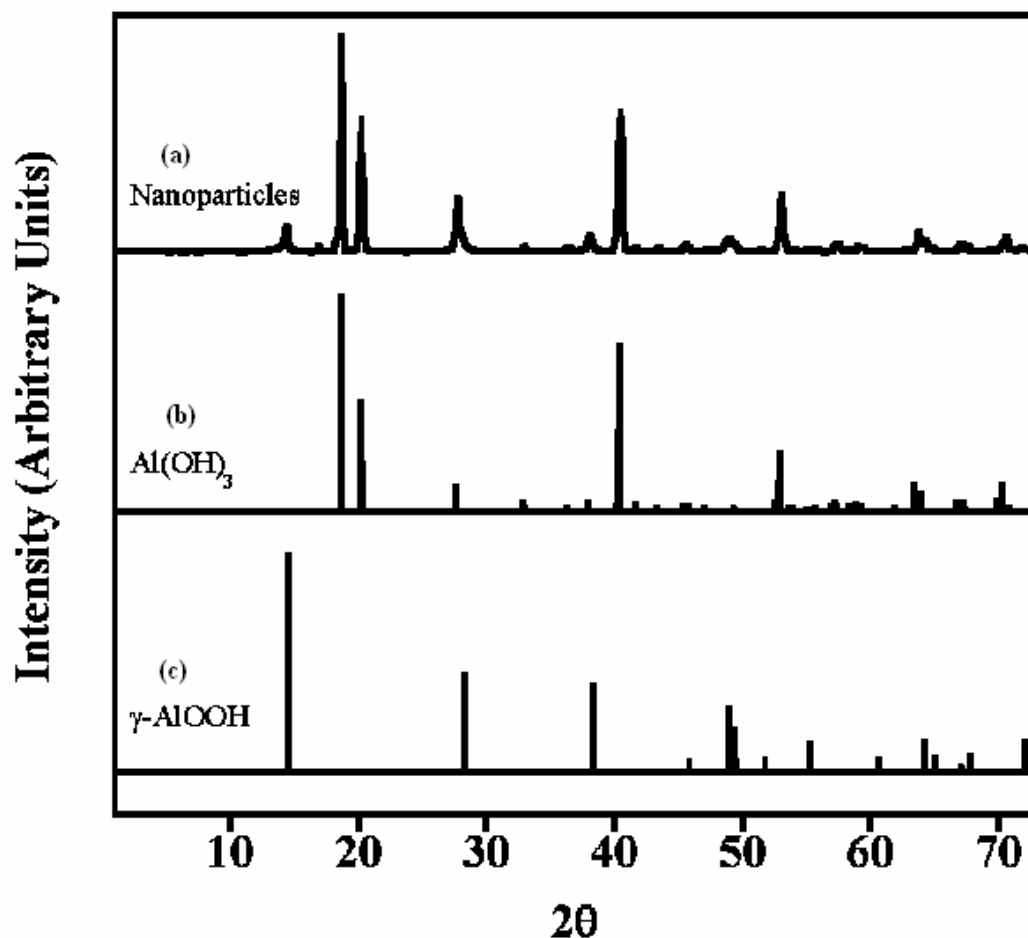
Figure 4.2: XRD pattern of alumina whiskers nanoparticles.[120]

4.3 Experimental Methods

4.3.1 Aluminum Based Materials

Two different alumina based materials were used in this study 4 x 2800 nm alumina whiskers and 10 nm alumina. Figure 4.1(a) and 4.1(b) show the transmission electron micrographs of the two samples. The differences between these samples lie in the size of the different nanomaterials and consequently surface area and morphology. 10

nm alumina is spherical in shape whereas the alumina whiskers are whisker or rod shaped. The external surface area for the two nanomaterials has been determined to be ca. 320 m^2 g^{-1} and 195 m^2 g^{-1}, respectively. The XRD pattern, determined with a Bruker D-5000 q - q diffractometer, confirms that alumina whiskers (Figure 4.2 a) are a hydroxide of aluminum and are composed of bayerite and boehmite phases (as shown in Figure 4.2 b,4.2 c), whereas the 10 nm alumina is an oxide of aluminum and consists of the gamma phase of Al_2O_3. Table 4.1 summarizes the size, surface area and phase information of the two nanomaterials used in this study.

Table 4.1: Summary of physical properties of alumina whiskers and 10 nm alumina.

	Size (nm)	Surface Area (m^2/g)	Phase
Alumina Whiskers	4x2800	320 ± 4	Bayerite [β-Al(OH)$_3$] +Boehmite [γ -AlO$_2$H]
10 nm Alumina	10	195 ± 3	γ Alumina

4.3.2 Transmission FTIR Spectroscopy

In situ transmission FTIR spectroscopy was employed to investigate the adsorption of CO_2 on these aluminum (alumina whiskers and 10 nm alumina) based materials. The infrared sample cell used here has been described previously.[52] Approximately 18 mg of the sample was mixed with a few drops of water resulting in the formation of a hydrosol. The hydrosol was then coated onto half of the tungsten grid and allowed to dry. The sample holder was then placed inside the stainless steel cube that sits on a linear translator inside the FTIR sample compartment. The linear translator allows each half of the sample grid to be translated into the infrared beam and permits the

detection of gas-phase and adsorbed species under identical reaction conditions. The samples were heated overnight under vacuum at 373 - 423 K temperature to remove adsorbed water. The next day, after the system has cooled, CO_2 was directly introduced into the reaction cell through the gas handling system. In these experiments, both the nanomaterials were exposed to carbon dioxide for around 30 minutes prior to a spectrum being recorded. It was followed by evacuation of system for 30 minutes. After this an increase pressure of CO_2 was introduced into the system. These steps were carried out repeatedly. Carbon dioxide was then adsorbed at different pressures at a temperature of 298 K. The exact pressures are given in the figure captions. Each spectrum was obtained by averaging 256 scans at an instrument resolution of 4 cm^{-1}.

4.4 Results and Discussion

4.4.1 Transmission FTIR Spectroscopy of Carbon Dioxide Adsorbed on Alumina Whiskers Under Dry Conditions

The adsorption of CO_2 on the alumina whiskers surface was carried out at pressures ranging from 0.274 Torr (equal to ambient pressure of CO_2) to 20 Torr of CO_2 as shown in Figure 4.3 below. On introduction of CO_2 we observe the appearance of a broad feature in the spectra region from 1000 to 1800 cm^{-1}. These peaks are low in intensity at lower CO_2 pressures and grow in intensity with increasing pressures. These peaks have been assigned to carbonate and bicarbonate formation. Different types of carbonate formation can occur on metal oxide surfaces.[63, 121] On this surface, we observe the formation of monodentate, bidentate and bridged carbonate formation. The peak for physically or linearly adsorbed CO_2 is low in intensity and is observed at 2342 cm^{-1}. The individual peaks are discussed in detail below and are also summarized in Table 4.2.
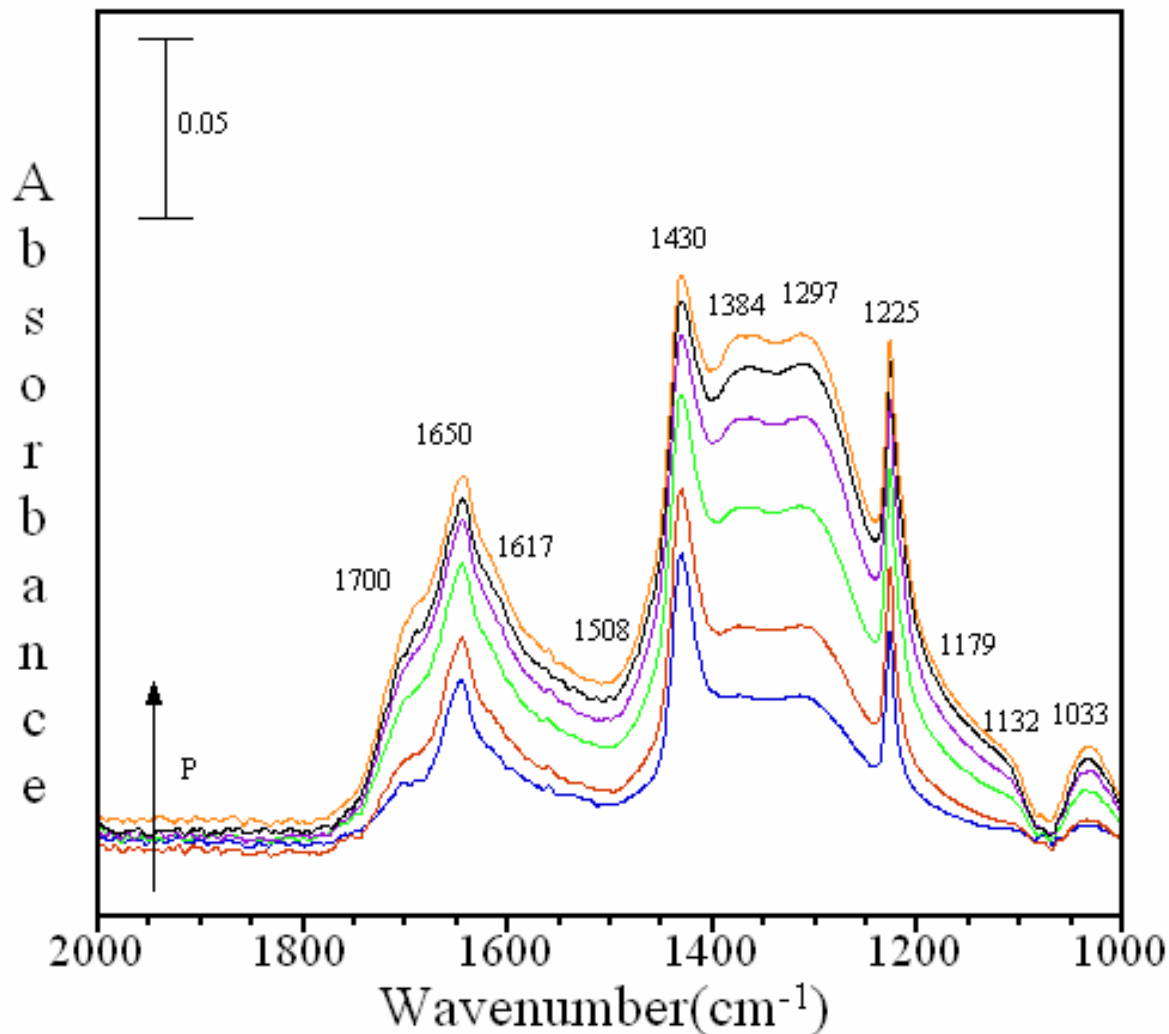
Figure 4.3: FTIR spectra of adsorbed $C^{16}O_2$ on dry commercial alumina whiskers as a function of CO_2 pressure. (P = 0.274, 0.989, 4.774, 11.4, 14.7, 20.6 Torr)

4.4.2.Transmission FTIR Spectroscopy of Carbon Dioxide
Adsorbed on 10 nm Alumina Under Dry Conditions

Likewise, adsorption of CO_2 on the 10 nm alumina surface was studied at similar pressures as for alumina whiskers, shown in Figure 4.4. We see in this case the appearance of a broad band (though low in intensity) in the 1000 to 1800 cm^{-1} region. These bands grow in intensity with increasing CO_2 pressures. Similarly, these peaks are
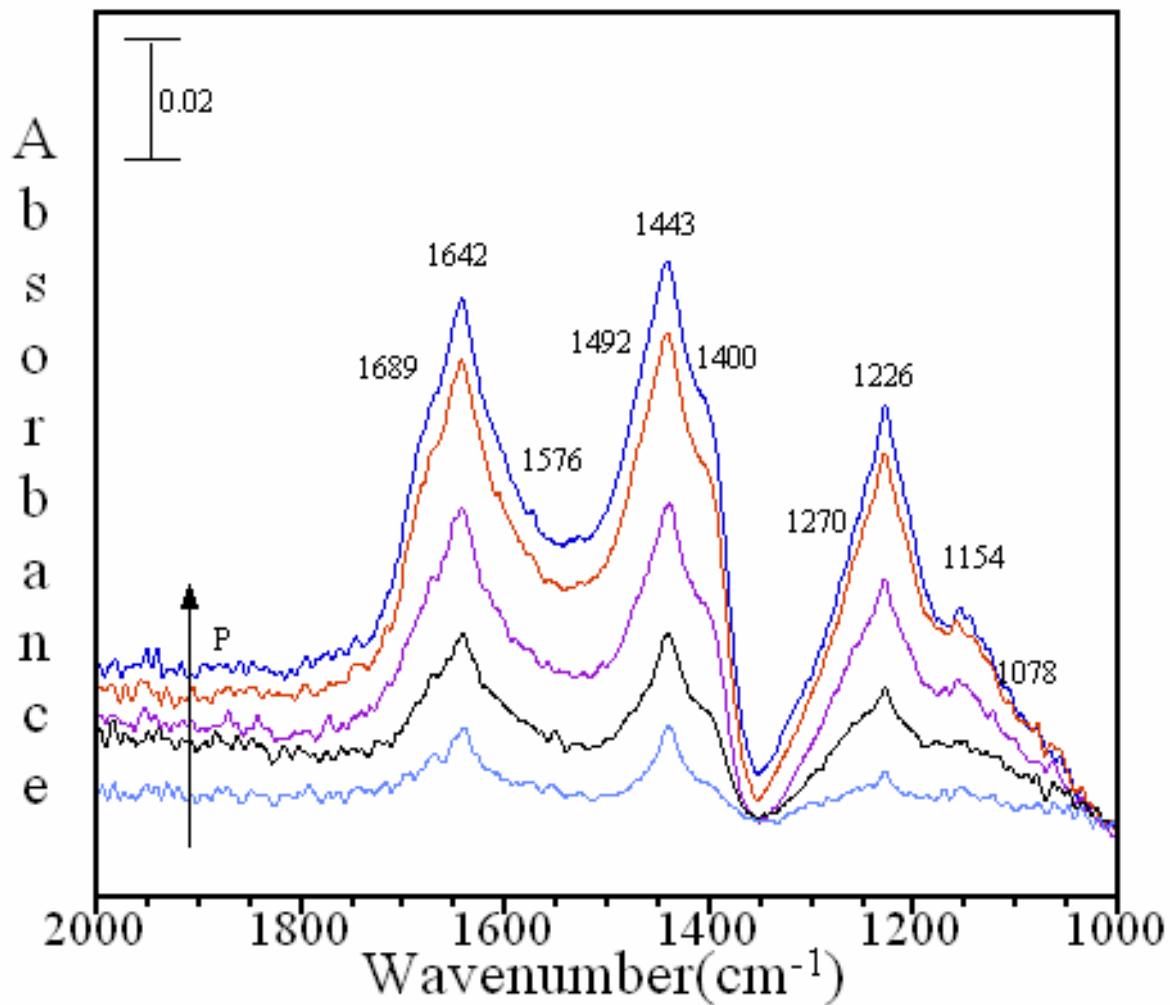
Figure 4.4:   FTIR spectra for of adsorbed $C^{16}O_2$ as a function of P (CO_2) on 10 nm alumina. The carbon dioxide pressures were 0.280, 1.002, 4.799, 11.7, 14.8, 19.5 Torr, respectively.

also assigned to carbonate (monodentate, bidentate and bridged), bicarbonate and linearly

adsorbed CO_2 formation (2345 cm^{-1}). The vibrational frequencies are summed up in

Table 4.2.

4.4.3 Transmission FTIR Spectroscopy of Carbon Dioxide
Adsorbed on Alumina Whiskers Versus 10 nm Alumina
Under Dry Conditions

In this section, the adsorption of $C^{16}O_2$ on nanoparticulate alumina whiskers and 10 nm alumina is compared at 1 Torr. Figure 4.5 shows the comparison of adsorption of CO_2 on the two aluminum based surfaces at a pressure of 1 Torr. The spectrum for alumina whiskers shows the presence of sharp peaks at 1650, 1430 and 1225 cm^{-1} which are assigned to the $\nu(OCO)a$, $\nu(OCO)s$ and $\delta(COH)$ vibrational modes of adsorbed bicarbonate, respectively. Similarly, for 10 nm alumina, in Figure 4.5 we see the presence of these bicarbonate bands at 1642, 1443, and 1226 cm^{-1}, respectively. It is important to note other vibrational bands such as $\delta(OCO)$, $\nu(OC-(OH))$, $\delta(CO_2)o.p.p.$ and $\nu(H$ torsion$)$ also associated for a bicarbonate species formation are situated below 850 cm^{-1}. [101, 106] Instrumental limitations as well as the aluminum oxide lattice absorptions below 850 cm^{-1} prevents these modes to be observed.[101, 106] For both the alumina whiskers and 10 nm alumina the $\nu(OH)$ is not observed. The vibrational frequencies of these peaks observed in the spectra are labeled and assigned in Table 4.2.

Bicarbonate species formation can be explained by the reaction mechanism previously proposed.[106] According to this mechanism, CO_2 is pre-adsorbed on the surface of the metal-oxide and is followed by intermolecular proton transfer by the neighboring hydroxyl groups of aluminum sites, resulting in bicarbonate formation. The reaction of carbon dioxide with surface hydroxyl groups has been shown to result in the formation of bicarbonate species.

For alumina whiskers and 10 nm alumina, in addition to the bicarbonate bands, carbonate bands are also present in the spectra as shown in Figure 4.5. In the case of
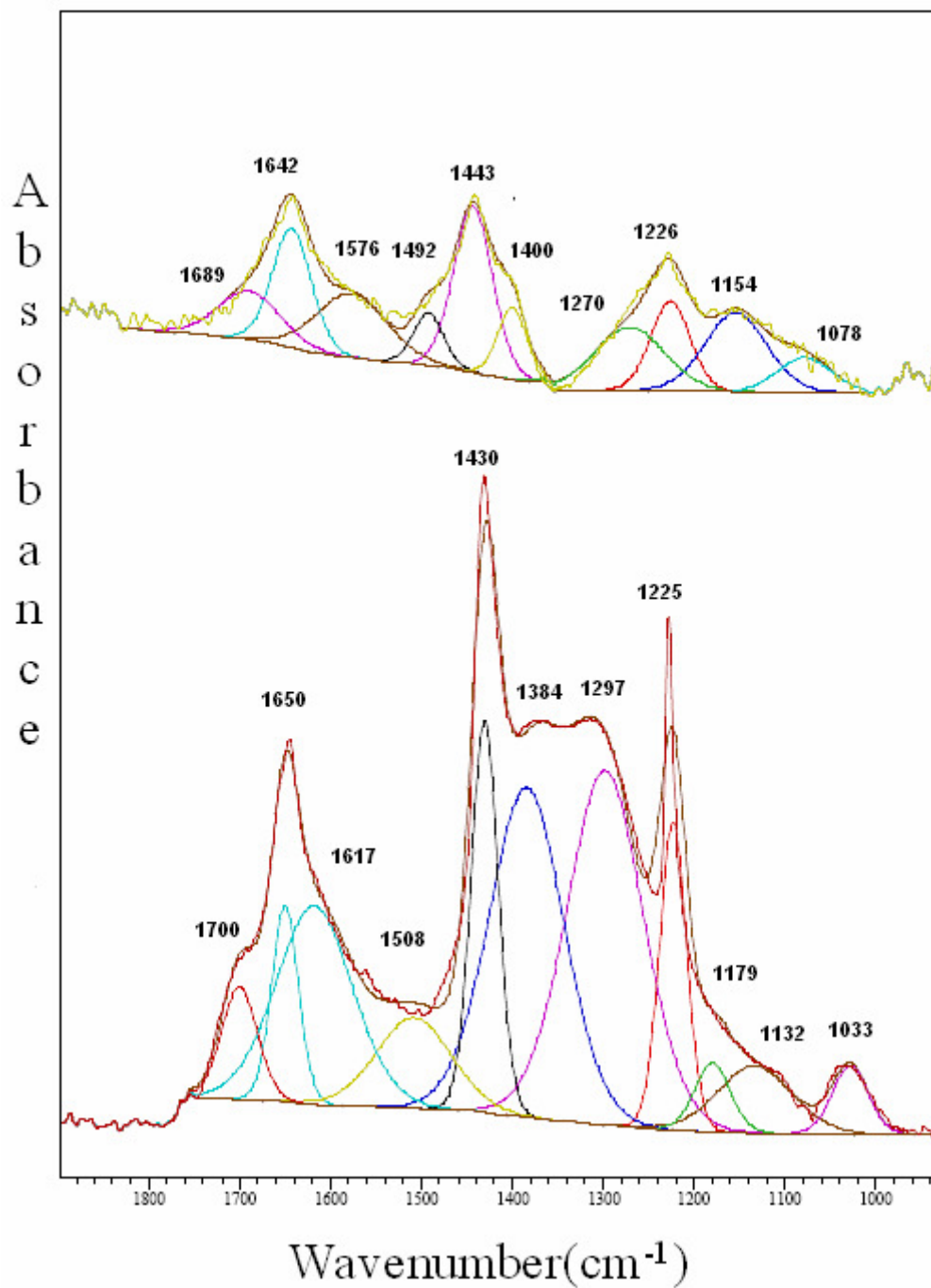
Figure 4.5: IR spectra of adsorbed CO_2 on alumina whiskers (lower spectrum), and 10 nm alumina (upper spectrum) at a CO_2 pressure of 1 Torr.

alumina whiskers, the underlying peaks present in the spectra at 1384, 1508 and 1132 cm$^-$^{1} are associated with monodentate form of carbonate, for the v(O-C-O)a, v(O-C-O)s and v (C-O)s modes respectively. Other peaks observed at 1297 and 1617 cm^{-1} are assigned to the bidentate carbonate formation. Whereas the other peaks at 1700, 1179 and 1033
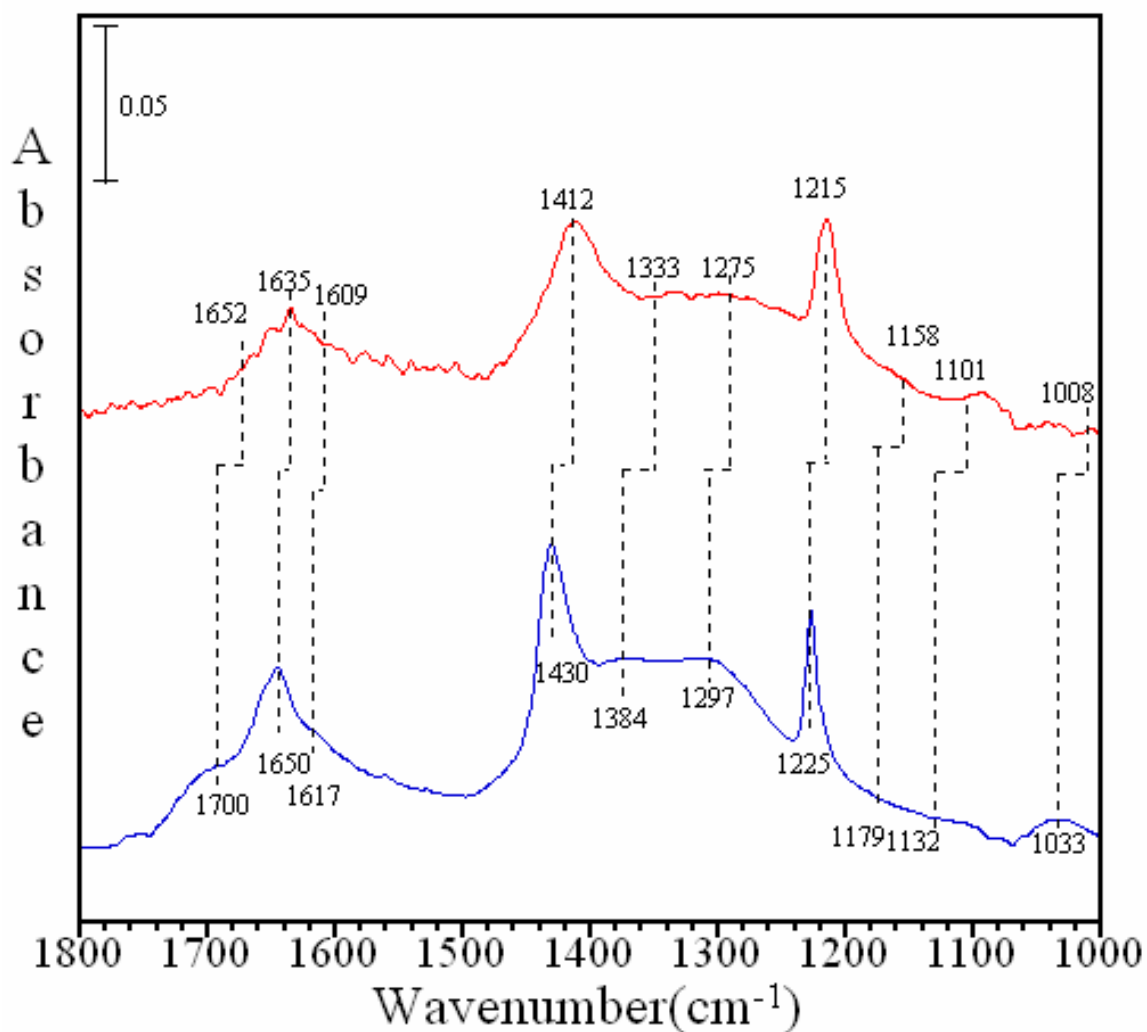
Figure 4.6: Absorbance spectra of adsorbed C^{16}O$_2$ (blue) and adsorbed C^{18}O$_2$ (red) on alumina whiskers at a pressure of 1 Torr and a temperature of 296 K.

cm^{-1} are assigned to the ν(O-C-O)a , ν(O-C-O)s , ν(C-O)s modes of the bridged carbonate formation. For 10 nm Al_2O_3, we observe some underlying peaks in the spectrum, which are also assigned to various carbonate species formation. The peaks at 1400, 1492 and 1078 cm^{-1} are specifically the ν(O-C-O)s, ν(O-C-O)a and ν(C-O)s stretching modes respectively. These absorptions peaks are assigned to the adsorbed monodentate carbonate formation. Other low intensity shoulder peaks due to bidentate carbonate species are observed at 1576 and at 1154 cm^{-1} for 10 nm alumina. Bridged carbonate vibrational bands are also underlying and are seen at 1689 and 1270 cm^{-1}. These bands are suggested to arise from the ν_3 asymmetric (O-C-O), ν_3 symmetric (O-C-O) stretch for the bridged structure of carbonate.

In Figure 4.5, on comparing the intensities of CO_2 adsorption on both the alumina surfaces, we see that alumina whiskers have more product formation. It is expected from the surface area measurements (i.e. higher the surface area leads to more adsorption sites and thus more product formation (carbonates and bicarbonates)), therefore this trend in absorbance or product formation is observed: i.e. alumina whiskers absorb more CO_2 than 10 nm alumina. We saw an extensive carbonate product formation on alumina whiskers whereas extensive bicarbonate formation is observed on 10 nm alumina. The carbonate-bicarbonate ratio for alumina whiskers (3.6) is greater than 10 nm alumina (1.5). The difference in the product formation in these nanomaterials can be explained in terms of the coordination geometry of aluminum sites. In alumina whiskers, the aluminum Al^{3+} sites have an octahedral coordination which favors carbonate formation by exposing the basic surface O^{2-} ions for the carbonate formation.[66, 106, 112, 129-131] On the

Table 4.2: Summary of experimental vibrational frequencies for adsorbed carbonate/bicarbonate formation in different aluminum based nanomaterials under dry conditions at $C^{16}O_2$ (and $C^{18}O_2$) [a] pressure of 1 Torr.

Adsorbed Species	Vibrational Mode	Alumina Whiskers (cm⁻¹)	10 nm Alumina (cm⁻¹)	Literature References (cm⁻¹)[b]
CO$_2$ Linear Complex				
	ν_3	2342	2345	2300-2400
Bicarbonate				
	ν_2(O-C-O)a	1650 (1635)	1642 (1633)	1615-1671
	ν_3(O-C-O)s	1430 (1412)	1443 (1421)	1396-1500
	δ_4(COH)	1225 (1215)	1226 (1217)	1220-1269
Carbonate				
Monodentate				
	ν_1(C-O)s	1132 (1101)	1078(1064)	1012-1074
	ν_3(O-C-O)s	1384 (1333)	1400(1392)	1360-1395
	ν_3(O-C-O)a	1508	1492 (1466)	1410-1590
Bidentate				
	ν_1(C-O)s	1033 (1008)	-	1015
	ν_3(O-C-O)s	1297 (1275)	1154 (1132)	1143-1355
	ν_3(O-C-O)a	1617 (1609)	1576 (1562)	1535-1670
Bridged				
	ν_1(C-O)s	1033 (1008)	-	1030
	ν_3(O-C-O)s	1179 (1158)	1270(1255)	1228-1198
	ν_3(O-C-O)a	1700 (1652)	1689 (1655)	1650-1711

[a] $C^{18}O_2$ frequencies in parentheses.

[b] Literature references [34, 37, 122-128]

other hand, the 10 nm alumina forms mainly bicarbonate species as it has minimal aluminum in octahedral coordination.

Figure 4.6 shows the spectrum resulting from adsorption of $C^{18}O_2$ versus $C^{16}O_2$ on alumina whiskers. As expected, we see a red shift in all the peaks due to carbonate (monodentate, bidentate, bridged) as well as due to bicarbonate formation. 18 labeled O, CO_2 was adsorbed on both the surfaces at 1 Torr, and the corresponding vibrational frequencies are summed up in Table 4.2 in parenthesis.

4.5 Conclusions

The adsorption of CO_2 was carried out on aluminum based materials (gamma alumina and alumina whiskers) under dry condition. CO_2 adsorbs on these nanomaterials with the formation of carbonates and bicarbonates depending upon the surface area and the coordination geometry of the nanomaterials. Under dry conditions, both the aluminum based surfaces react with carbon dioxide to form linearly adsorbed CO_2, bicarbonate and carbonate species. Nanocrystalline alumina whiskers have higher activity for CO_2 conversion compared to 10 nm alumina. This difference can be attributed mainly to an increased surface area. There are also some differences in surface carbonate/bicarbonate speciation observed between the two nanomaterials. The surface Al^{3+} coordination plays a key role in the surface chemistry of metal oxide surfaces and determines product formation; Al^{3+} coordination in octahedral coordination preferentially exposes basic O^{2-} ions towards the surface for carbonate product formation. The 10 nm alumina resulted in formation of mainly bicarbonate whereas the alumina whiskers

formed mainly carbonate species. All the peak assignments and other conclusions were supported with isotope experiments.

4.6 Acknowledgements

CHAPTER V

FTIR SPECTROSCOPY COMBINED WITH ISOTOPE LABELING AND QUANTUM CHEMICAL CALCULATIONS TO INVESTIGATE REACTIONS OF CARBON DIOXIDE ON ZINC OXIDE SURFACE

5.1 Abstract

In this study, CO_2 adsorption in the presence and absence of co-adsorbed H_2O was investigated on a zinc oxide surface. Under dry conditions, CO_2 reacts with ZnO surface O-H groups to form bent CO_2, adsorbed bicarbonate, carbonate and carboxylate species. The stability of adsorbed species was examined with evacuation experiments. Carbonate and carboxylate species were found to be more stable than bicarbonate and bent CO_2, which desorbs instantly on evacuation. In the presence of co-adsorbed water, adsorbed CO_2 and H_2O reacts to yield surface adsorbed carbonate species through a bicarbonate/carbonic acid intermediate mechanism earlier proposed by Baltrusaitis et al. Mixed isotope studies conducted demonstrate an extensive isotope exchange between oxygen in adsorbed carbon dioxide and oxygen in adsorbed water. Time course plots of the isotope mixing observed as a function of time suggests that the exchange is continuous over a time scale of hours. Adsorption of ^{18}O-labeled carbon dioxide and theoretical quantum chemical calculations confirm these assignments and conclusions.

5.2 Introduction

Carbon dioxide (CO_2) is the fourth most abundant gas in the atmosphere uniformly distributed over the Earth's surface with a concentration of about 385 ppm.[6] As

CO_2 plays an important role in global warming, carbon dioxide storage and conversion are topics of great importance to the scientific community and the public. Recent studies indicate that nanomaterials have the potential to adsorb and convert CO_2 into more useful products.

It is also well known that oxides and carbonates are important environmental interfaces.[54-56, 109] Zinc is an important naturally occurring mineral on Earth and exists in the form of wurtzite (zinc sulfide), smithsonite (zinc carbonate), zincite (ZnO) and other important minerals.[69] The applications of zinc oxide are numerous, and, as a result, it is constantly added into the atmosphere. Zinc oxide has many important properties such as a high refractive index, antibacterial properties, good thermal conductivity and others. Therefore, it is used in the manufacturing of important industrial products such as cement, plastics, glass, rubber, lubricants, paints, ointments, ceramics, pigments, fire retardants etc.[46,54,92,132-144] The surface chemistry of a metal oxide under ambient conditions plays a critical role in environmental as well as biological systems. Enzyme carbonic anhydrases (active component Zn) is an enzyme in the body that catalyzes the rapid hydration of carbon dioxide to bicarbonate.[145-149] Previous studies of CO_2 adsorption on ZnO under dry condition, resulted in the formation of adsorbed carbonates, bicarbonates, carboxylates, formates and bent CO_2 species. Recent studies of CO_2 adsorption on a ZnO surface has shown that an "unusual tridentate carbonate" species is formed with the two O atoms of the CO_2 molecule being almost equivalently bound to two different Zn surface atoms.[70] Although there have been numerous of IR spectroscopic studies of CO_2 adsorption on zinc oxide surfaces, in this paper we present FTIR experimental data for a systematic study of CO_2 adsorption on a nanomaterial ZnO

surface under dry as well as wet conditions, including isotope data to support vibrational mode assignments. To provide insights into the molecular structure of the carbonate, bicarbonate and carboxylate product formation as a result of reaction of CO_2 with the metal oxide surface, quantum chemical calculations were done. Differences are observed under different conditions investigated, with the formation of carbonates, bicarbonates and carboxylates depending upon the experimental conditions. Under wet conditions, water plays a significant role in the overall surface chemistry of CO_2. Adsorbed water blocks some of the reactive sites on the surface of ZnO and influences the reaction chemistry and product formation from bicarbonate, carbonate and carboxylate to carbonate formation only.

5.3 Experimental and Theoretical Methods

5.3.1 Transmission FTIR Spectroscopy

In situ transmission FTIR spectroscopy was employed to investigate the adsorption of CO_2 on the nanoparticulate zinc oxide surface. The infrared sample cell and the set up used has been described previously.[51] FTIR spectra were recorded using a single beam Mattson Infinity Gold FTIR spectrometer with a liquid nitrogen-cooled narrow band mercury–cadmium–telluride (MCT) detector. Firstly, the zinc oxide sample was calcined in a furnace at ~ 473 K to get rid of carbonate impurities. After calcination, approximately 15-20 mg of zinc oxide sample was mixed with a few drops of water resulting in the formation of a hydrosol, which was then coated onto half of the tungsten grid and allowed to dry. The sample holder was then placed inside the stainless steel cube that sits on a linear translator inside the FTIR sample compartment. The samples were

heated overnight under vacuum at ~ 473 K temperature to remove adsorbed water. CO_2 and H_2O were directly introduced into the reaction cell through the gas handling system. Two absolute pressure transducers were used to monitor the pressures. In the dry experiments, *i.e.* in the absence of co-adsorbed water, the zinc oxide was exposed for around 30 minutes to carbon dioxide prior to a spectrum being recorded. Carbon dioxide was then adsorbed at different pressures corresponding to the pressures ranging from 0.274 to 20 Torr. In the wet experiments carbon dioxide and water were also co-adsorbed onto the zinc oxide. Water vapor H_2O (40% RH) and CO_2 (0.274 Torr) were first introduced into the premix chamber cell and then allowed to equilibrate in the reaction cell for 30 minutes. All of these experiments were carried out at room temperature (296 K). The exact pressures are given in the figure captions. Each spectrum was obtained by averaging 256 scans at an instrument resolution of 4 cm^{-1}.

5.3.2 Sources of Oxide, Water and Carbon Dioxide

Commercially available ZnO nanopowder was used in these experiments with a specific surface area of 15 ± 1 m^2g^{-1} and was purchased from Melorium Technologies. The surface area was measured using a Quantachrome Nova 4000e Multipoint BET apparatus. The X-ray diffraction pattern obtained using a Bruker D-5000 q-q diffractometer with a Cu Kα source suggests a hexagonal wurtzite structure for the ZnO nanopowder. The JEOL TEM-1230 Transmission Electron Microscope was used to obtain acquire images of the nanoparticulate materials. Figure 5.1 shows a transmission electron micrograph of the ZnO nanomaterial, which shows the particles to be spherical

with a particle size distribution of approximately 25±1 nm in diameter based on the image. The particle size distribution is shown in Figure 5.2.

100 nm
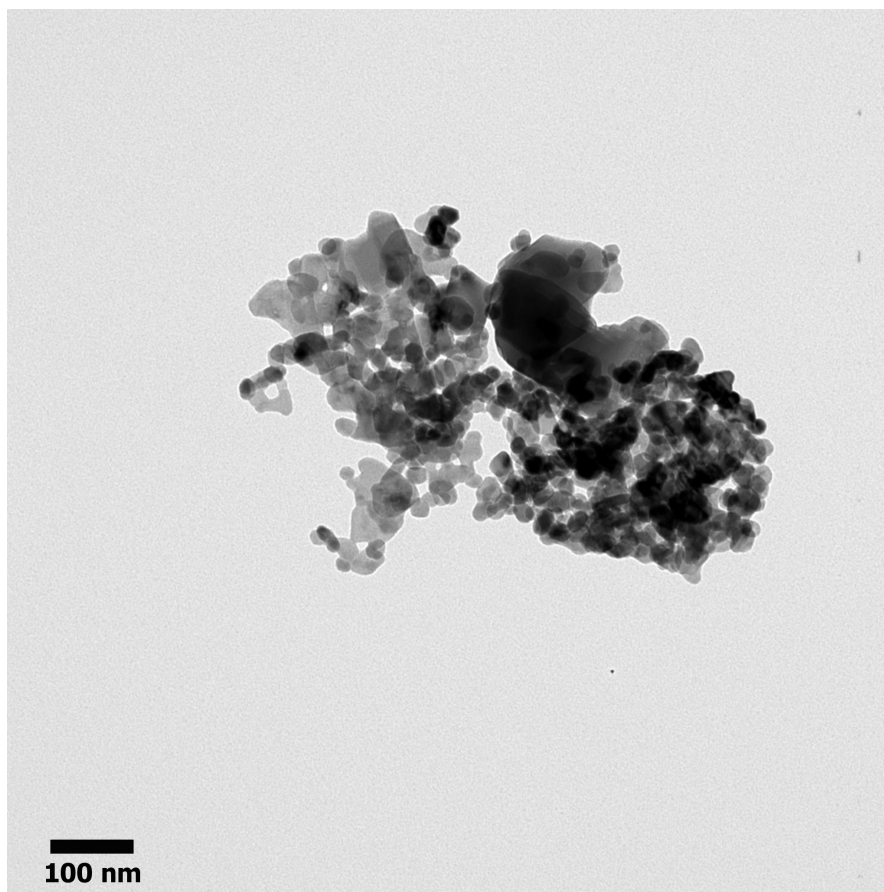
Figure 5.1: Transmission electron micrograph of ZnO used in this study.

Depending upon the isotope required water vapor was taken from the headspace of the different glass bulbs. Distilled H_2O was purchased from Fisher Scientific Inc.and was degassed prior to use. [18]O labeled water, purchased from ISOTEC (minimum 95 atom % 18O) and was used as received. Research grade carbon dioxide was used, and $C^{18}O_2$, was purchased from ISOTEC (minimum 97 atom % 18O). CO_2 gases, both

labeled and unlabeled, were used directly from the gas cylinders without any pretreatment.
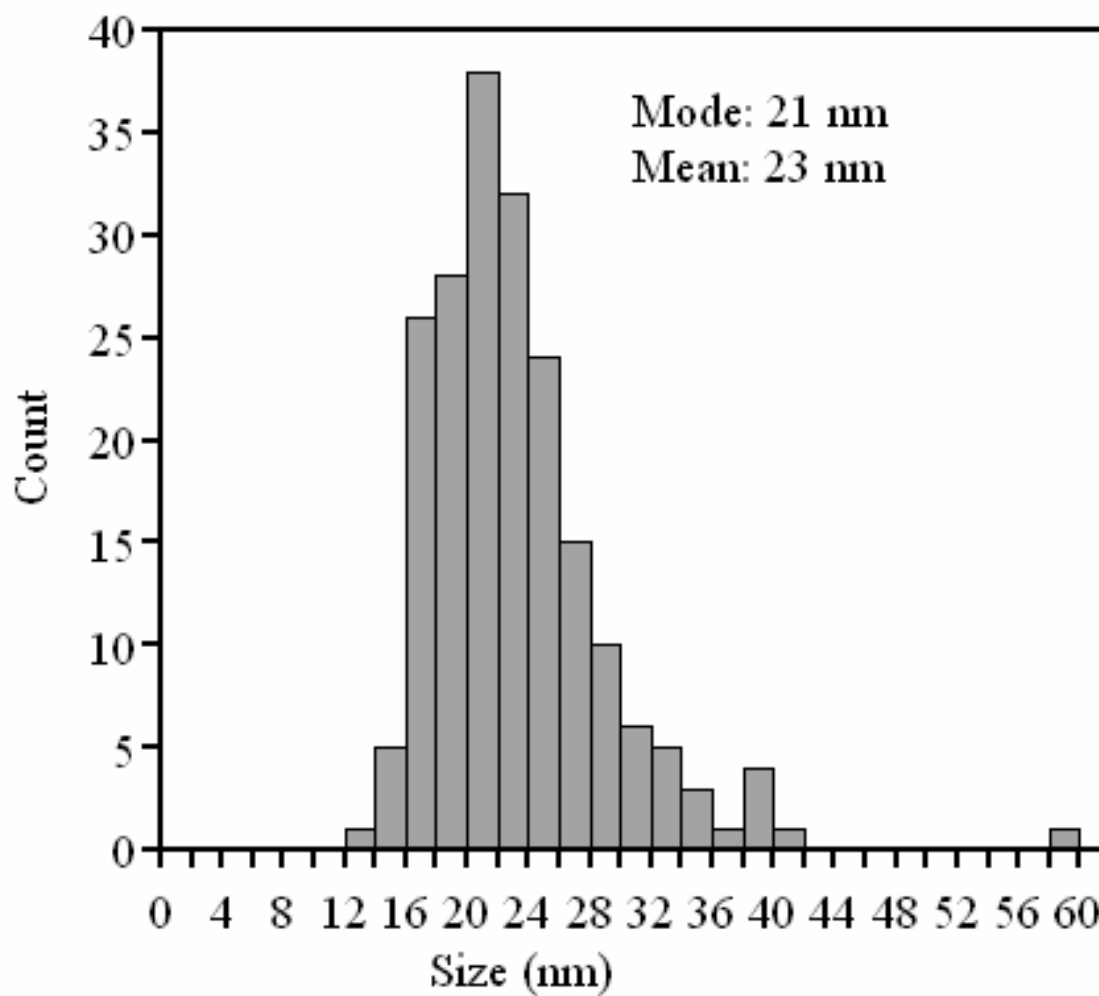
Figure 5.2: Size distribution of ZnO nanoparticles.
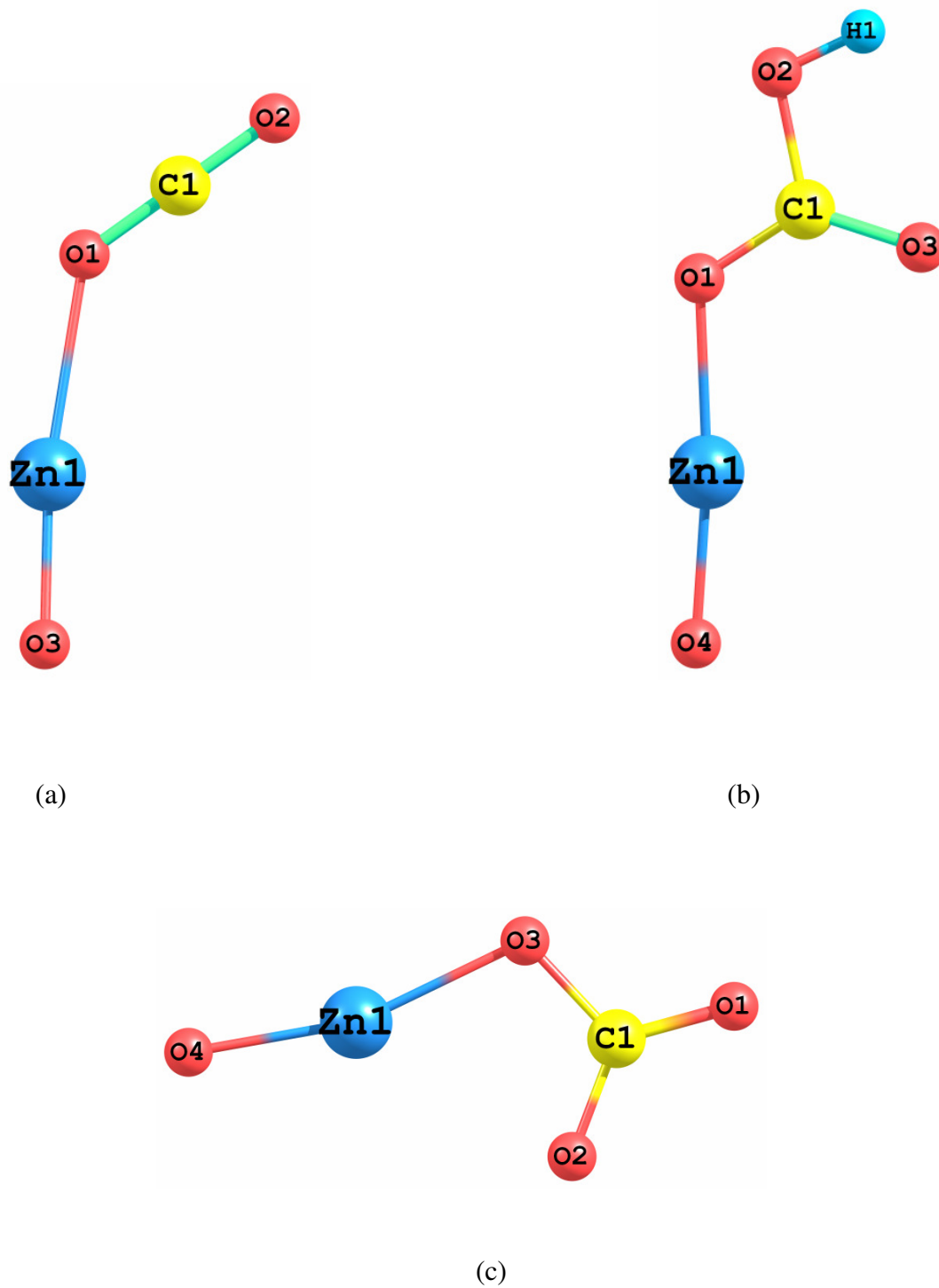
Figure 5.3: Energy minimized structures for (a) bent CO_2; (b) bicarbonate; (c) monodentate carbonate; (d) bidentate carbonate; and (e) carboxylate formed on the ZnO surface.

(d)

(e)
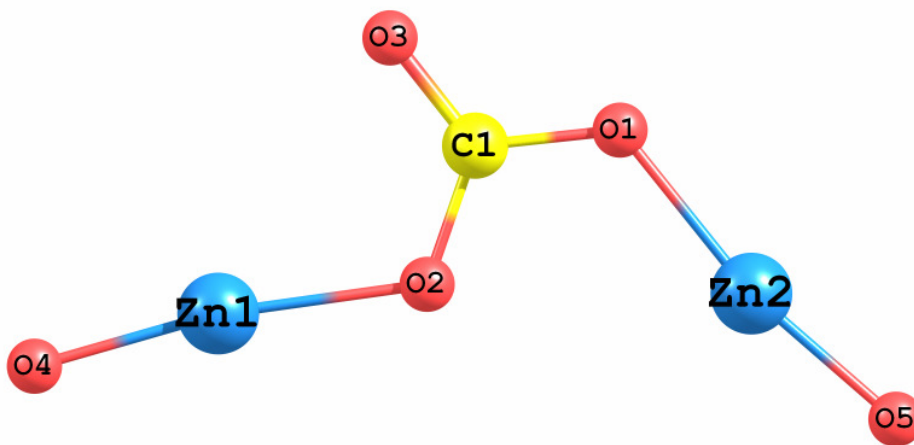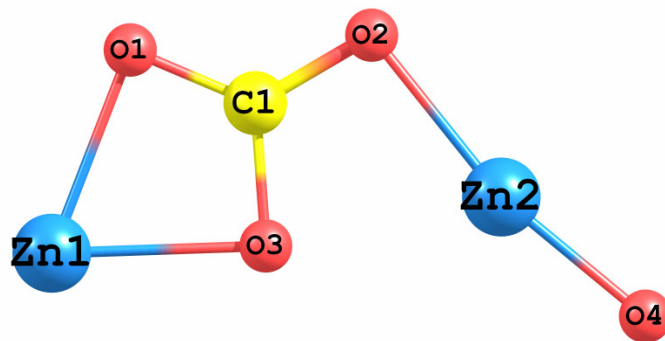
(Figure 5.3 continued)

*5.3.3 Quantum Chemical Calculation of Carbon Dioxide,
Bicarbonate, Carbonate and Carboxylate Complexes*

All molecules and clusters were optimized within the Density Functional Theory approximation[82-84] using spin restricted calculations with B3LYP functional as implemented in Turbomole and TZVP basis set[85,86] with multipole accelerated resolution of identity approximation[87] (MARIJ-B3LYP/TZVP). No symmetry constraints were imposed during the geometry optimization. Vibrational frequencies were calculated after the optimization at the same level of theory to confirm that the optimized geometry was a minimum in the potential energy surface. No negative vibrational frequencies were observed for minimum structures. Geometry optimization and frequency calculations were performed using Turbomole 6.1 package running on a Linux workstation.[88] All structures were visualized using commercially available Chemcraft software.[150] All energy minimized structures for (a) bent CO_2, (b) bicarbonate, (c) monodentate carbonate, (d) bidentate carbonate and (e) carboxylate formed on the ZnO surface are shown in Figure 5.3.

5.4 Results and Discussion

*5.4.1 Transmission FTIR Spectroscopy and Quantum
Calculations of Carbon Dioxide Adsorbed on ZnO
Under Dry Conditions*

FTIR spectra of zinc oxide surface exposed to CO_2 as a function of increasing pressure from 0.274 Torr to 20 Torrs, was taken. The adsorption of CO_2 on ZnO surface results in the formation of complex absorption region between the 2000 and 1000 cm^{-1} region and the bands in this region grow in intensity as the carbon dioxide pressure increases. Figure 5.4 shows the adsorption of CO_2 on the ZnO surface as a function of

increasing CO_2 pressure. Three intense peaks in the spectra are seen at 1225, 1422, and

1630 cm^{-1} which are distinctive of the bicarbonate species formation.
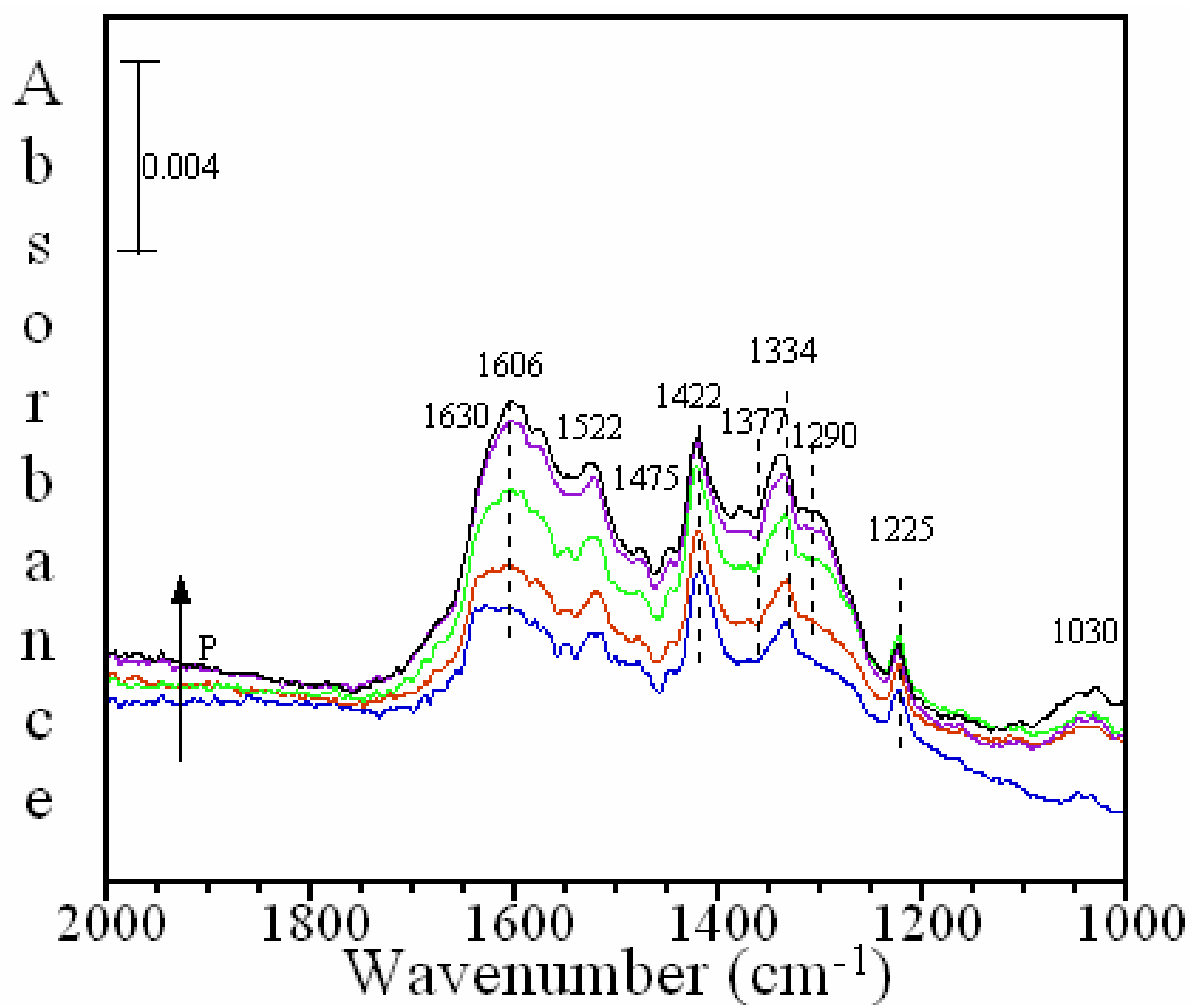
Figure 5.4: Transmission FT-IR spectra of CO_2 adsorbed on dry commercial ZnO as a function of pressure in the spectral range extending from 2000 to 1000 cm^{-1} (P = 0.274, 0.989, 4.774, 11.4, 14.7 and 20.6 Torr).

These peaks at 1225, 1422, and 1630 cm^{-1} are assigned to the δ_4(COH), ν_3(O-C-O)s, and

ν_2(O-C-O)a vibrational modes respectively.[106, 151-156] The ν_1(OH) supposed to be

observed in the 3600-3000 cm^{-1} but in this case is obscured due to noise in the higher

wavenumber region and is not shown in this figure. The mechanism of the bicarbonate
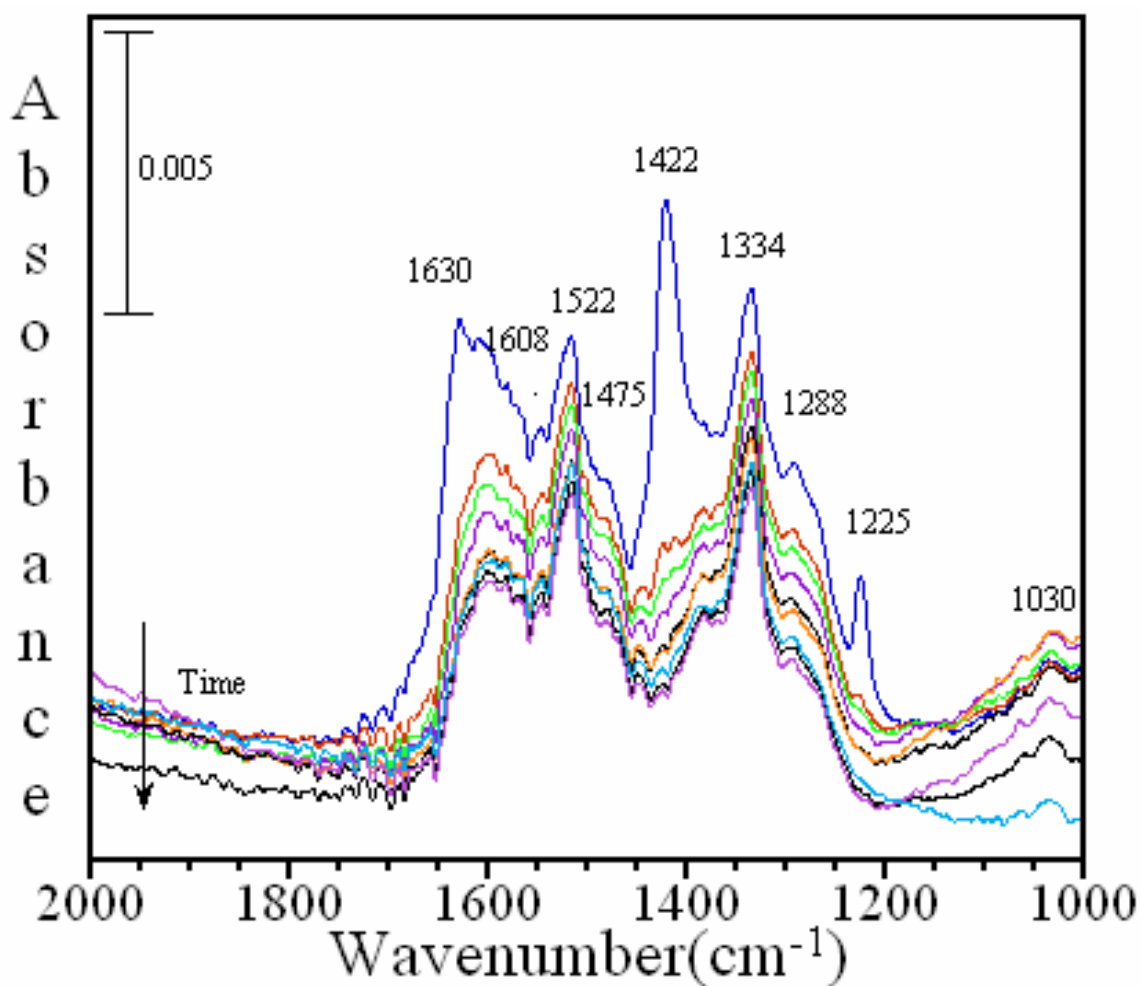
Figure 5.5: Transmission FT-IR spectra of evacuation of CO_2 adsorbed on ZnO in the spectral range extending from 2000 to1000 cm^{-1}. The losses in the spectra are due to the desorption of bicarbonate species are shown.

 formation is suggested to occur with an initial nucleophilic attack of CO_2 on the metal

oxide surface followed by an intermolecular proton transfer that results in the formation

of bicarbonate structure.[106] The energy minimized structure for bicarbonate formation is shown in Figure 5.3(b), and the corresponding calculated frequencies (at 1 Torr CO_2 pressure) are summarized along with the experimental frequencies in Table 5.1 to further support our vibration assignments. It is important to mention here that there is small shift in wavenumbers for some of the peaks at different CO_2 pressures.

In addition to the bicarbonate peaks, a number of other peaks are observed in the spectra. The other peaks that appear at 1475 and 1377 cm^{-1}, are due to O-C-O stretching vibrations of the monodentate carbonates species.[151, 153, 157-160] Similarly, the adsorption at 1606 and 1334 cm^{-1} are assigned to OCO stretching, both symmetric and asymmetric stretching, of bidentate carbonate species.[151-153, 156, 157, 160] Low intensity peaks observed at 1030 and 994 cm^{-1} correspond to the CO stretching modes of adsorbed monodentate and bidentate carbonates, respectively. Figure 5.3 (c) and (d) shows the optimized structures for possible monodentate and bidentate carbonate adsorbed products. The bidentate carbonate formed has a bridging structure wherein the oxygen atoms of the carbonate are shared between two different surface Zn atoms. The vibrational frequency calculations for carbonate/bicarbonate adsorbed on the surface show three bands, where the ν_3 mode is degenerate and is split into ν_3(O–C–O)a and ν_3(O–C–O)s bands. Table 5.1 also gives the calculated ν_1 and ν_3 vibrational frequencies for the different type of carbonate species formed.

If a bridged carboxylate structure, as in Figure 5.3(e), is formed analogous ν_3(O–C–O)a and ν_3(O–C–O)s bands are expected to be observed in the experimental infrared

Table 5.1 Summary of experimental and calculated vibrational frequencies for adsorbed $C^{16}O_2$ (and $C^{18}O_2$) at 1 Torr on the ZnO surface under dry conditions.

Adsorbed Species	Vibrational Mode	ZnO Frequency(cm^{-1}) $C^{16}O_2$ ($C^{18}O_2$)	Calculated Frequency (cm^{-1})	Literature Frequency (cm^{-1}) [a]
Bent CO$_2$				
	ν_1	-	1369	-
	ν_3	2350 (2305)	2423	2364-2353
Bicarbonate				
	ν_1(OH)	-	3793	3620-3605
	ν_2(O-C-O)a	1630 (1620)	1747	1650-1610
	ν_3(O-C-O)s	1422 (1400)	1369	1435-1424
	δ_4(COH)	1225 (1211)	1228	1230- 1228
Carbonate				
Monodentate				
	ν_1(C-O)s	1030	989	1040
	ν_3(O-C-O)s	1375 (1355)	1393	1404-1370
	ν_3(O-C-O)a	1475 (1452)	1580	1480-1425
Bidentate				
	ν_1(C-O)s	994 (976)	1017	1030- 999
	ν_3(O-C-O)s	1334 (1319)	1314	1364-1303
	ν_3(O-C-O)a	1608 (1577)	1573	1665-1512
Carboxylate				
	ν_1(C-O)s	-	1050	1030
	ν_3(O-C-O)s	1288 (1275)	1310	1382-1300
	ν_3(O-C-O)a	1522 (1500)	1621	1580-1508

[a] Range taken from references. [151-154, 156-161]

data. In the spectra, the stretches at 1522 and 1290 cm^{-1} observed can be assigned to the v_3(O-C-O)a and v_3(O-C-O)s modes due to the formation of carboxylate species based on literature.[151-153, 156, 160, 161]

CO_2 adsorption not only leads to the formation of chemisorbed products but also physisorbed bent CO_2, as suggested by the peak at 2350 cm^{-1}. The presence of this bent CO_2 structure is further confirmed with the help of quantum calculations, as shown in Figure 5.3(a). The intensity of this weakly bound bent CO_2 species increases as a function of increasing CO_2 pressures. This peak at 2350 cm^{-1} is assigned to the asymmetric stretching mode (v_3) of CO_2. Another peak must be observed near 1382 cm^{-1} due to the symmetric stretch of CO_2. However, this peak is not observed and is probably hidden underneath the broad and overlapping spectral region. All of the experimental vibrations observed are summarized in Table 5.1.

Evacuation experiments, using FTIR spectroscopy, of the ZnO surface after the exposure to 1 Torr of CO_2 as a function of time were performed as shown in Figure 5.5. In these experiments the stability of adsorbed surface species is determined. Of all the adsorbed species, adsorbed bicarbonate and bent CO_2 species were found to be unstable upon evacuation of gas-phase CO_2. The peaks due to adsorbed bicarbonate species, at 1225, 1422, and 1630 cm^{-1}, decrease significantly in intensity, upon evacuation. The peaks that stay behind in the spectrum and are stable are due to adsorbed carbonates (both monodentate adsorption and bidentate carbonate) and carboxylate species. This suggests that carbonate and carboxylate species are stable and remain adsorbed on the surface of ZnO even upon evacuation for longer time duration. These results are consistent with previous literature observations of CO_2 adsorption on other metal oxides. As we know,
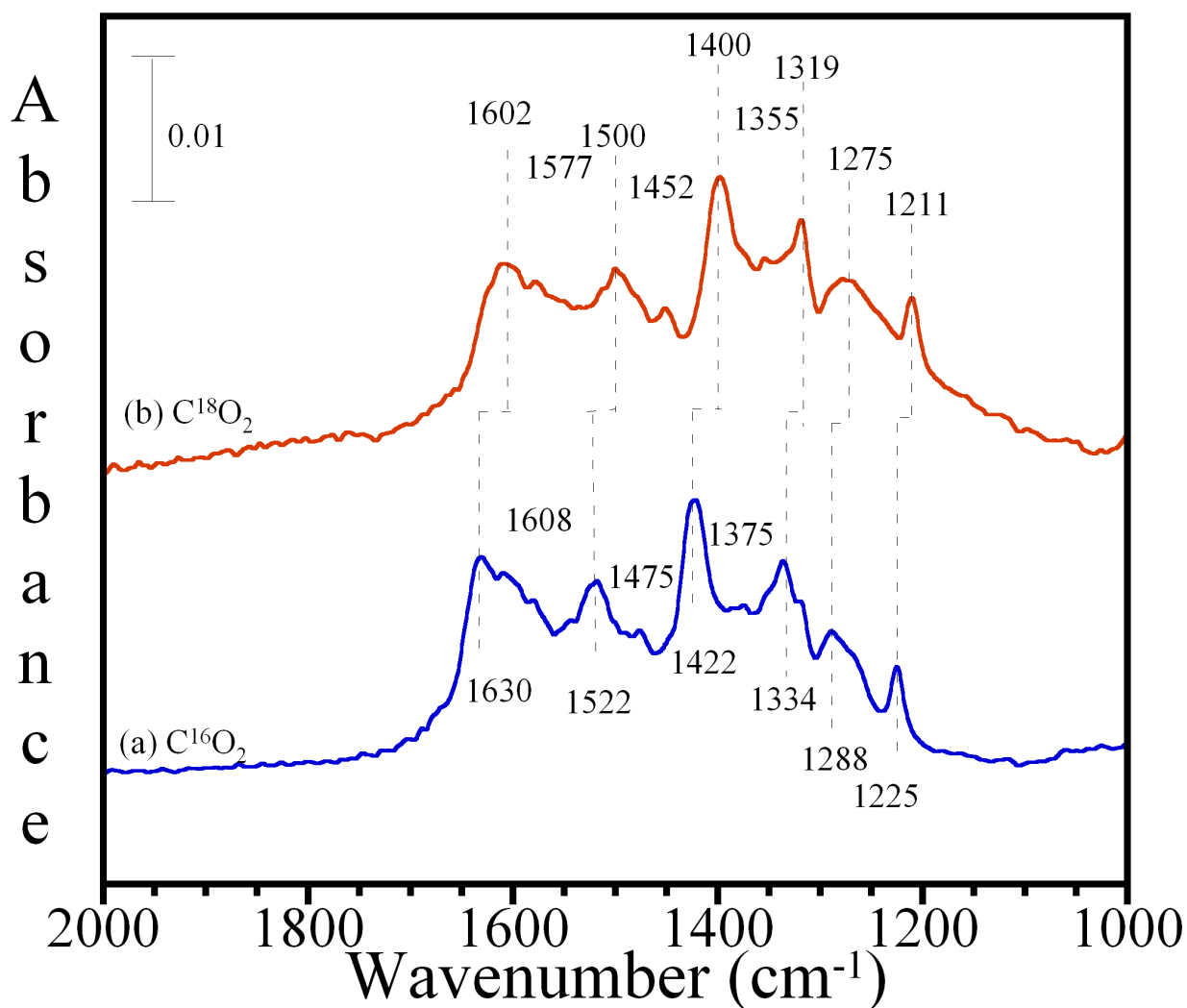
Figure 5.6: Transmission FT-IR spectra of adsorbed (a) $C^{16}O_2$ (black); and adsorbed (b) $C^{18}O_2$ (red) on ZnO at a pressure of 1 Torr and a temperature of 296 K.

isotope-labeling FTIR experiments can provide information about the surface adsorbed species, therefore isotope experiments were performed. O^{18} labeled CO_2 was adsorbed onto the surface of ZnO surface, to investigate the vibrational frequencies of surface adsorbed species, as shown in Figure 5.6. Shifts in vibrational frequencies for all the characteristic peaks due to bent CO_2, bicarbonate, carbonate and carboxylate species

were observed which further supports our vibrational mode assignments. The isotope vibration frequencies have also been summarized in the Table 5.1

Table 5.2: Summary of experimental vibrational frequencies for adsorbed H_2O at 40% RH on the ZnO surface.

Vibrational Mode	ZnO Frequency(cm^{-1})
O—H Stretching [a]	3695
	3620
	3475
	3408
H—O—H Bending	1642
Association mode	2218
Water solvated surface carbonate	1406

[a] The O—H stretching region is broad and has four underlying absorption peaks at 3695, 3620, 3475, 3408 cm^{-1}.

5.4.2 Transmission FTIR Spectroscopy of Water Adsorbed on ZnO

FTIR spectroscopy was used to analyze H_2O adsorption on ZnO surfaces. For comparison, the ZnO surface was exposed to water vapor as a function of increasing relative humidity in the absence of CO_2. Figure 5.7(a) and (b) shows the transmission FTIR spectra, in higher and lower wavenumber regions, of ZnO as a function of increasing relative humidity (from < 5 % to 75 % RH). We observe in this spectrum a peak at 1642 cm^{-1} due to the bending mode of adsorbed water. A broad and low intensity peak at 1406 cm^{-1} has been assigned to water solvated surface carbonate based on the fact that a small amount of carbonate species was initially present on the ZnO surface.[126] The

O—H stretching region was broad and uninteresting with underlying absorption peaks at 3695, 3620, 3475, 3408 cm^{-1}, as shown in this figure. Also a weak band at 2218 cm^{-1} was seen and is called association band. This band is a result of the combination of bending, liberation, and hindered translation modes, $\nu_2+\nu_L-\nu_T$, respectively, and is not shown in this Figure.[126] The vibrational frequencies are summed up in Table 5.2.
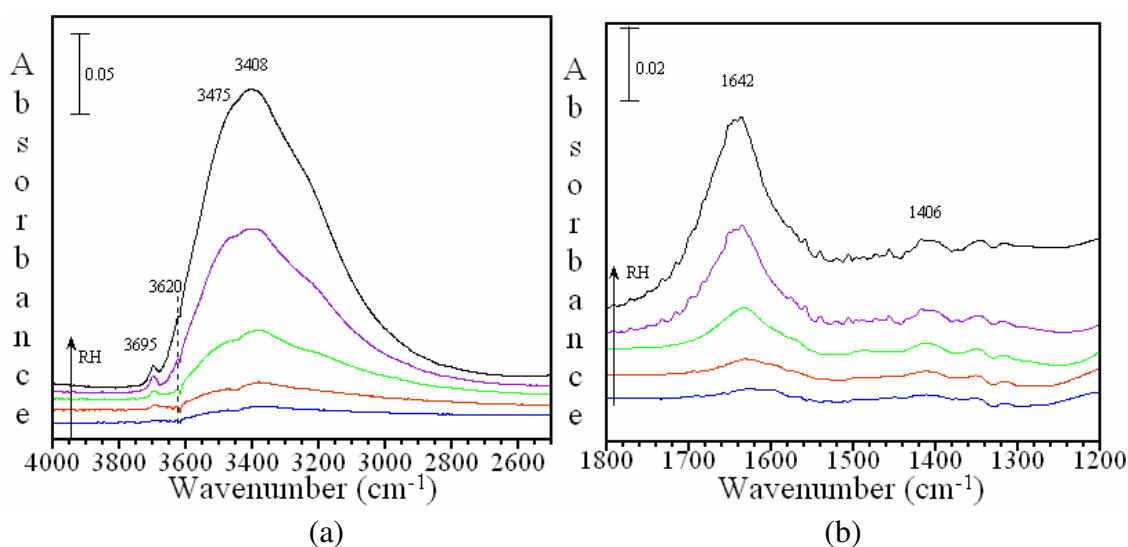
Figure 5.7: Transmission FTIR spectra of ZnO as a function of increasing relative humidity (from < 5 % to 75 % RH). (a) 4000-2500 cm^{-1};(b) 1800-1200 cm^{-1} region.

5.4.3 Transmission FTIR Spectroscopy and Quantum Calculations of Carbon dioxide Adsorbed on ZnO Under Wet Conditions

The spectrum shown in Figure 5.8(a) is due to adsorbed H_2O at 40% RH on ZnO. The spectrum in Figure 5.8(b) shows the adsorbed products on the surface after exposure to a mixture of carbon dioxide (0.274 Torr of $C^{16}O_2$) and water (40% RH) at 296 K. Whereas, spectrum 5.8(a) showed only adsorbed H_2O, the resulting spectra are quite

similar (Figure 5.8(a) and 5.8(b)). Therefore, a difference spectrum was taken as shown in Figure 5.8(c), showing low intensity peaks due to the formation of a small amount of carbonate. These absorption bands are assigned to the monodentate and bidentate carbonate formation. The OCO stretching modes at 1507 and 1400 cm^{-1} are due to monodentate carbonate formation,[151, 153, 157-160] and vibrations at 1602, 1340 cm^{-1} are due the OCO stretching for the bidentate carbonate formation.[152, 153, 155-157, 160] The weak absorption bands seen in the difference spectrum are due to the formation of small amount of carbonate species. An increase in the intensity of these peaks due to adsorbed carbonate occurs with an increase in RH. For the O-H stretching region, 3400-4000 cm^{-1}, not much difference is observed. The vibrational frequencies are summarized in Table 5.3.

Previously, Baltrusaitis et al. has shown the formation of carbonate species in presence of CO_2 and relative humidity, for both nanoparticulate Fe_2O_3 and Al_2O_3 surfaces, suggesting water catalyzes the formation of carbonate species. It involves the initial adsorption and reaction of H_2O and CO_2 to yield a bicarbonate intermediate that rearranges to form the carbonic acid, and strong hydrogen bonding with surface adsorbed hydroxyl groups further stabilizes the carbonic acid. Carbonic acid formed then deprotonates to form carbonate species, as shown below (here M = Zn). [117, 162-164]

$$H_2O(a) + CO_2\ (a) + MOH \leftrightarrow MOH_2^+ + HCO_3^- \tag{3}$$

$$MOH_2^+ + HCO_3^- \leftrightarrow MOH + H_2CO_3 \tag{4}$$

$$2MOH + H_2CO_3 \leftrightarrow MOCO_2^- + MOH_2^+ + H_2O(a) \tag{5}$$
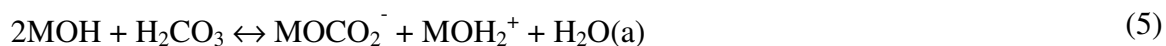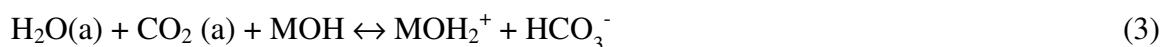
There is an absence of carboxylate species that was otherwise observed under dry conditions. As suggested previously in literature, presence of a dissociative electron donor, such as water, aids in the conversion of carboxylate species to the unidentate
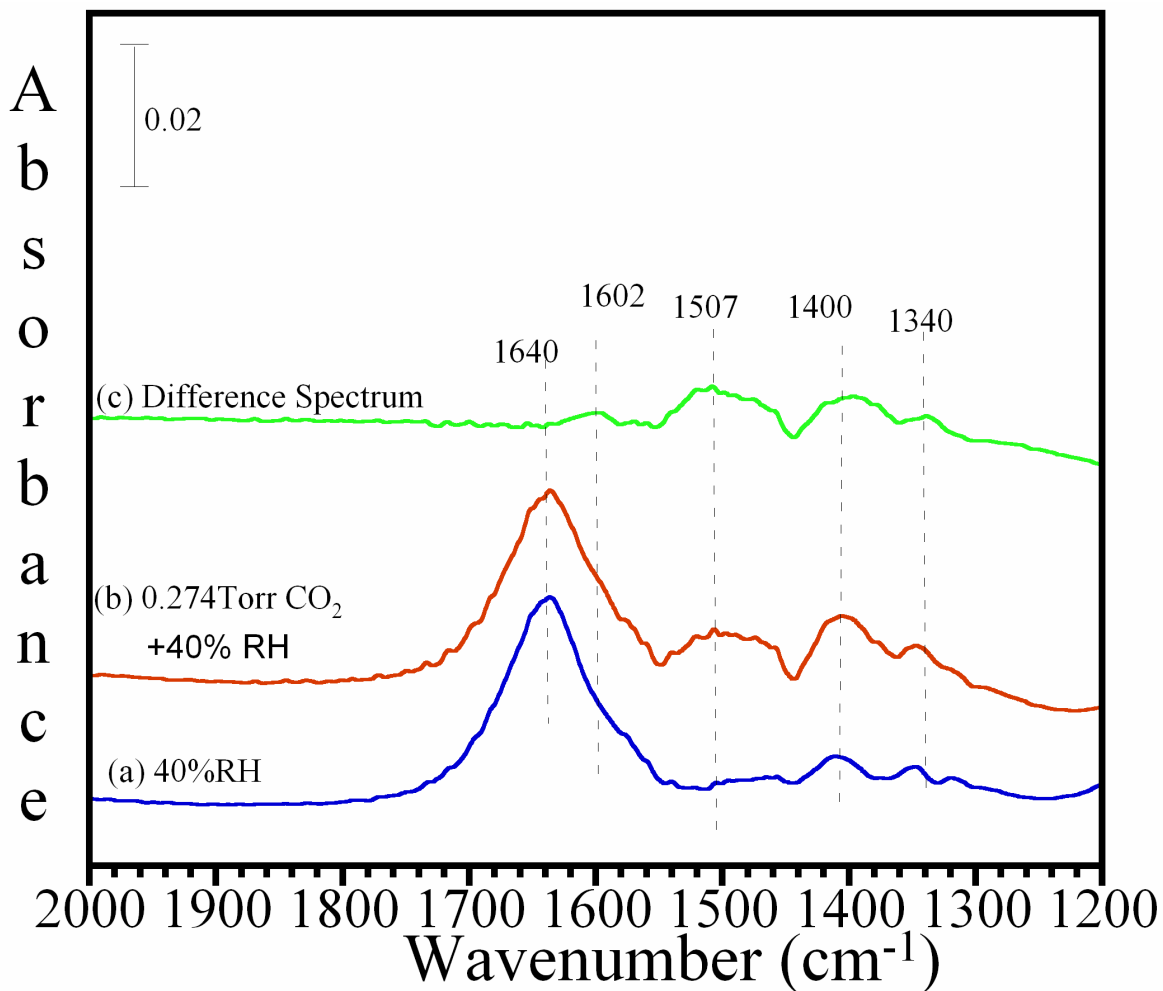
Figure 5.8: Transmission FTIR spectrum (a) of ZnO following exposure to 40% relative humidity (RH); (b) of ZnO following exposure to 0.274 Torr CO_2 pre-equilibrated with 40% RH ; and (c) is a difference spectrum as a result of the spectral subtraction of ZnO in the presence of H_2O at 40% RH from the spectrum of ZnO in the presence of 0.274 Torr CO_2 and H_2O at 40% RH.

carbonate species.[33] The possible monodentate and bidentate carbonate formation structures are shown in Figure 5.3(c) and 5.3(d) and have been explained earlier.
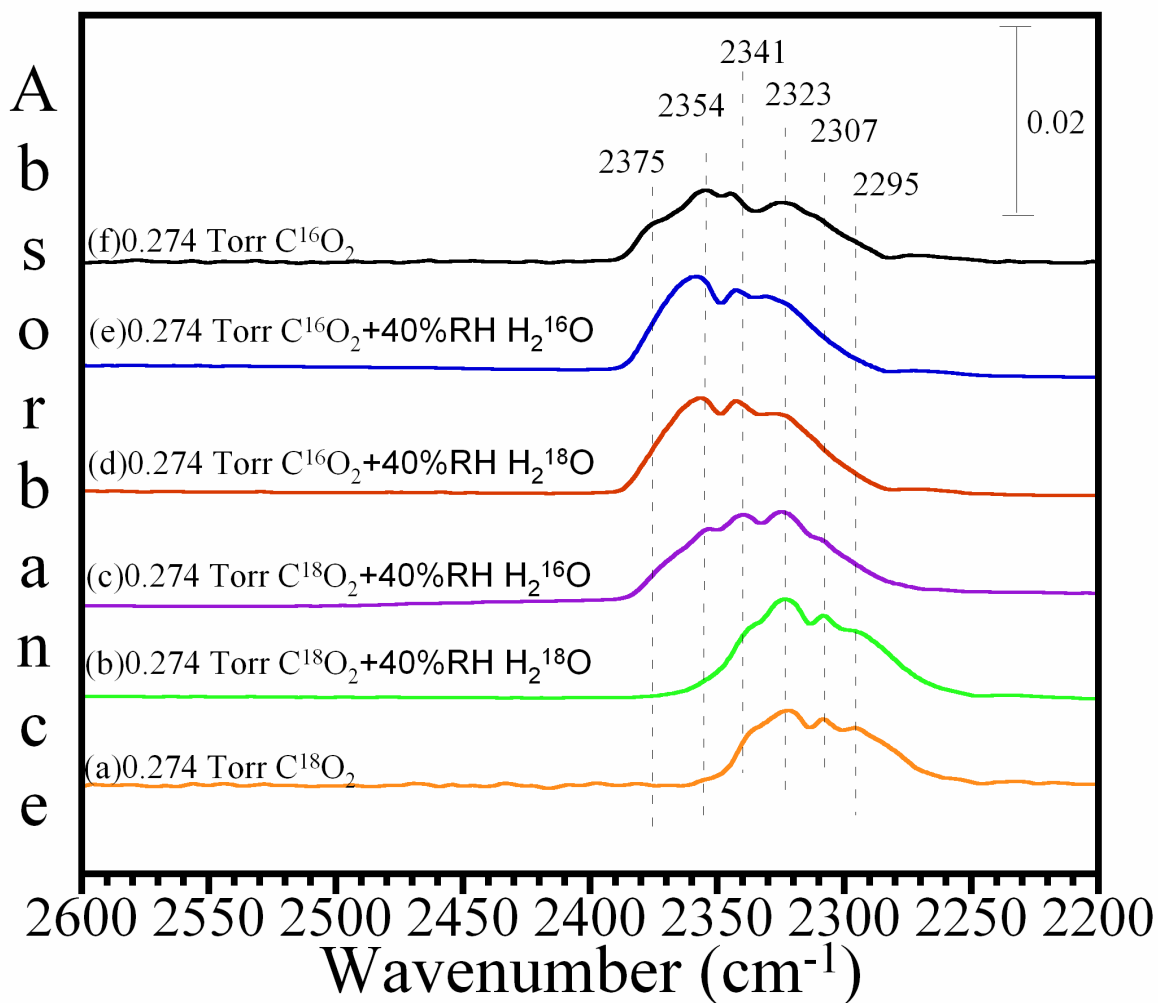
Figure 5.9: Gas-phase transmission FTIR spectra of (a) 0.274 Torr $C^{18}O_2$; (b) 0.274 Torr $C^{18}O_2$ and 40% RH $H_2^{18}O$; (c) 0.274 Torr $C^{18}O_2$ and 40% RH $H_2^{16}O$; (c) 0.274 Torr $C^{16}O_2$ and 40% RH $H_2^{18}o$; (c) 0.274 Torr $C^{16}O_2$ and 40% RH $H_2^{16}o$; and (d) 0.274 Torr $C^{16}O_2$ on nanoparticulate ZnO.

Isotope-labeling experiments in the presence of co-adsorbed water were conducted for better understanding the reaction mechanism of premixed CO_2 and H_2O on the ZnO surface. These isotope-labeling experiments were performed using various isotope combinations of $C^{16}O_2$, $H_2^{16}O$, $C^{18}O_2$ and $H_2^{18}O$. Isotope combinations $C^{16}O_2 + H_2^{16}O$, $C^{16}O_2 + H_2^{18}O$, $C^{18}O_2 + H_2^{16}O$ and $C^{18}O_2 + H_2^{18}O$ were premixed, and a comparison was made with the transmission FT-IR spectra of pure $C^{16}O_2$ or $C^{18}O_2$ at 0.274 Torr, as shown in Figure 5.9 for nanoparticulate ZnO. Examination of the gas-phase spectra suggests that isotope mixing occurs in the gas-phase i.e. upon adsorption of isotopically labeled CO_2 and H_2O, slight shifts in the vibrational frequencies occurred as compared to the pure $C^{16}O_2$ and $C^{18}O_2$ adsorption frequencies. One can conclude that extensive isotope exchange is observed between oxygen atoms of the CO_2 and H_2O in the gas-phase. To further justify our conclusion, blank experiments were conducted in absence of the ZnO surface, and no changes in the peaks for gas-phase CO_2 or H_2O were observed. As a result, we can conclude that the isotope scrambling observed is surface mediated. The corresponding adsorptions for the adsorbed carbonate are not shown here since the adsorption intensities are small and broad and any change is overshadowed by the broadness of the adsorbed carbonate species. Baltrusaitis et al. has previously proposed the isotope substitution reaction mechanism following the $C^{18}O_2 + H_2^{16}O$ exposure on an aluminum oxide surface.[117, 162-164]

$$H_2^{16}O + C^{18}O_2 \leftrightarrow H_2C^{18}O_2^{16}O \tag{6}$$

$$H_2C^{18}O_2^{16}O \leftrightarrow H_2^{18}O + C^{16}O^{18}O \tag{7}$$

$$H_2^{16}O + C^{16}O^{18}O \leftrightarrow H_2C^{16}O_2^{18}O \tag{8}$$

To further see the isotope scrambling in the gas-phase, in the presence of the ZnO surface in the reaction cell, $C^{18}O_2 + H_2^{16}O$, $C^{16}O_2 + H_2^{18}O$ was monitored on a longer time scale ranging from a few seconds to a couple of hours. FT-IR spectra were recorded every 4 seconds, at an instrument resolution of 4 cm^{-1}. Figure 5.10 shows the gas-phase spectra.

Table 5.3: Summary of experimental and calculated vibrational frequencies for adsorbed 0.274 Torr $C^{16}O_2$ on the ZnO surface under wet (40% RH) conditions.

Adsorbed Species	Vibrational Mode	ZnO (Wet) Frequency (cm^{-1})	Calculated Frequency (cm^{-1})	Literature Frequency (cm^{-1})[a]
Carbonate				
Monodentate				
	ν_1(C-O)s	-	989	1040
	ν_3(O-C-O)s	1400	1393	1404-1370
	ν_3(O-C-O)a	1507	1580	1480-1425
Bidentate				
	ν_1(C-O)s	-	1017	1030- 999
	ν_3(O-C-O)s	1340	1314	1364-1303
	ν_3(O-C-O)a	1602	1573	1665-1512

[a] Range taken from references.[151-161]

that were collected while the zinc oxide was exposed to 0.274 Torr of $C^{18}O_2$ and 40%RH ($H_2^{16}O$) as a function of time. These time course plots are used to illustrate this isotope mixing observed as a function of time. A gradual shift in the $C^{18}O_2$ occurs towards higher

frequencies as a result of isotope mixing ($C^{16}O^{18}O$) between the oxygen atoms of CO_2 and H_2O.
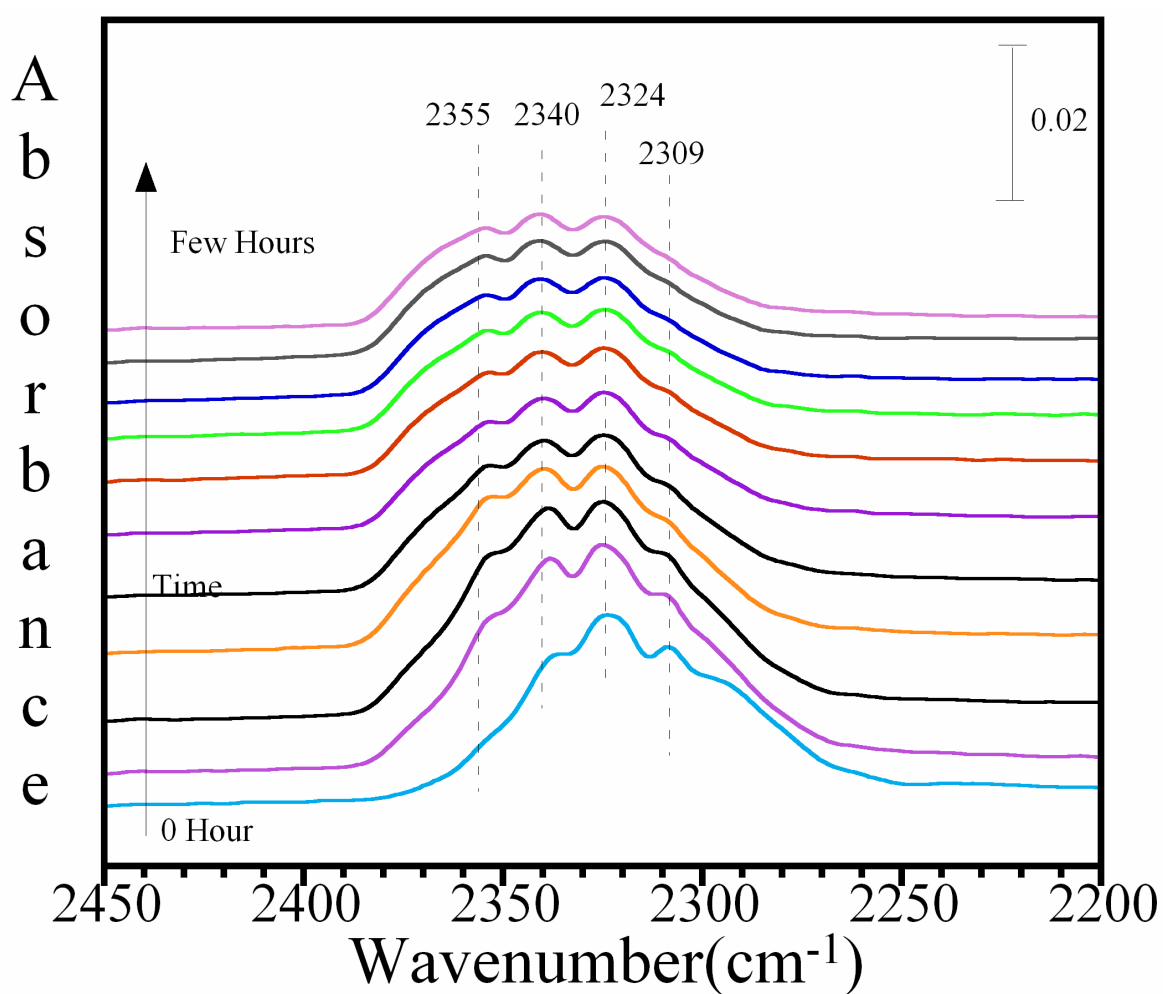
Figure 5.10: Gas-phase transmission spectra of 0.274 Torr $C^{18}O_2$ and 40% RH $H_2^{16}O$ on nanoparticulate ZnO as a function of time.

5.5 Conclusions

To conclude, under dry conditions, the ZnO surface reacts with carbon dioxide to form bent CO_2, bicarbonate, carbonate and carboxylate species. Under wet conditions, water and carbon dioxide adsorbs on the metal oxide surface, which forms bicarbonate and carbonic acid intermediates. The carbonic acid intermediate then deprotonates to adsorbed carbonate species. All the peak assignments and other conclusions were supported with quantum calculation and isotope experiments. Thus, CO_2 and H_2O premixed can have potential implications in atmospheric chemistry and can have interesting chemistry.

5.6 Acknowledgements

CHAPTER VI

CARBON DIOXIDE ADSORPTION ON MgO NANOMATERIAL: EFFECT OF PARTICLE SIZE AND SURFACE AREA

6.1 Abstract

Alkaline earth-based oxides are important materials for the storage of carbon dioxide. Here a comparison of CO_2 adsorption on two different MgO samples is discussed. A commercially available low surface area material is compared to a lab-synthesized high surface area material. The preparation of the synthesized material is discussed briefly. Characterization of both the MgO samples for the phase, particle size, pore size and surface area was accomplished using several techniques and methods including scanning electron microscopy (SEM), transmission electron microscopy (TEM), powder X-ray diffraction (XRD), and nitrogen adsorption analysis. The results show that synthesized MgO has a high surface area in the range of 120-136 m^2/g and a narrow pore size distribution in the range of 2-5 nm. In situ transmission FTIR spectroscopy was used to investigate CO_2 adsorption on the two MgO surfaces. This spectroscopic investigation shows that synthesized MgO exhibits enhanced CO_2 adsorption capacity relative to commercially available MgO nanoparticles. These differences can be attributed mainly to an increased surface area. There are also some differences in surface carbonate/bicarbonate speciation observed between the synthesized versus commercial MgO samples, which may be related to structural differences for the smaller nanoparticles.

6.2 Introduction

CO$_2$ plays an important role in global warming, carbon dioxide storage and conversion are topics of great importance to the scientific community and the public.[74, 165] Novel technologies and materials are needed to capture and store CO$_2$. Recent studies indicate that nanomaterials have the potential to adsorb and convert CO$_2$ into more useful products. One of the potential methods for the removal of CO$_2$ is the use of solid sorbent materials.[74] Recently, alkaline earth-based oxide materials have received increased attention as adsorbents for CO$_2$.[74, 75, 165] In the case of MgO, stoichiometric amounts of CO$_2$ can be taken up according to the reaction: MgO + CO$_2$ $\rightarrow$ MgCO$_3$. However, due to the low surface area-to-volume ratio of many materials and the formation of a termination layer of carbonate on the surface, there is a hindrance toward further reaction of the alkaline earth oxide such as MgO with CO$_2$.[166] Thus enhancing the efficiency of alkaline earth-based CO$_2$ absorbent is of great interest.[74, 166, 167]

Most current work focuses on alkaline earth-based sorbents using impregnation and wet mixing of potassium carbonate, alkaline metals for multiple CO$_2$ capture-and-release cycles.[74, 166, 168] A more effective method for enhancing the efficiency of CO$_2$ adsorption on alkaline earth oxides may be by decreasing the particle size for exposing more active sites. In recent years, metal oxide nanoparticles have been widely used in many applications including as adsorbents,[74, 169, 170] sensors,[171-173] and catalysts,[72, 174-176] due to their large surface area-to-volume ratio.[169, 171, 177] Additionally, MgO is one of the most important metal oxides. It has been used for application in catalysis, refractory material industries, paint, and superconductors.[71-73] MgO is also a promising sorbent for chemisorption of various pollutants.[73, 178]

Porous MgO is desirable for CO_2 adsorption. Porous materials have several advantages including high surface area, expedite mass transport, and can be more effectively recycled.[72, 179] In this study, a general strategy to synthesize MgO, a high surface area and small particle size, with a nanocrystalline framework via the thermal decomposition of magnesium alkoxide is discussed. In situ transmission FTIR of CO_2 adsorption on synthesized and commercial is then discussed, from which we learn that CO_2 can be absorbed effectively on the surface of synthesized MgO.[72]

6.3 Experimental Methods

6.3.1 Materials

Magnesium acetate tetrahydrate, commercial MgO and 1-butanol were purchased from Sigma-Aldrich. 1-Hexanol was obtained form Alfa Aesar. 2-Propanol was obtained form Fisher Scientific. Ethanol was obtained from Decon Laboratories, Inc. All chemicals were used without further purification.

Research-grade purity carbon dioxide ($C^{16}O_2$) was purchased from Airgas and was used directly without any purification.

6.3.2 Synthesis of Magnesium Oxide

The synthesized MgO is obtained by thermal decomposition of magnesium ethoxide occurs without the use of structure-directing reagent, such as surfactants. The steps of this process include the reaction of magnesium acetate with ethanol to obtain magnesium ethoxide, according to (1). First, 2.14 g of $Mg(CH_3COO)_2 \cdot 4H_2O$ is added to 200 mL ethanol. After stirring with a magnetic stir bar for 1 hour at 120 °C, a solid

product was obtained. The solid was recovered and purified by three centrifugation and re-dispersion cycles with acetone.

$$Mg(CH_3CO_2)_2 + CH_3CH_2OH \rightarrow Mg(CH_3CH_2O)_2 + CH_3CO_2H \tag{9}$$
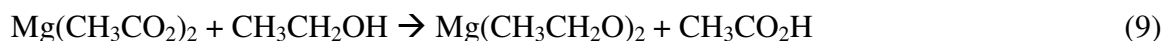
Second, the magnesium ethoxide obtained was then calcined at 500 °C for 2 hours with a heating rate of 2.0 °C/min in air, which breaks magnesium ethoxide into small MgO nanoparticles. In this high temperature step, volatile gases are generated as the framework of magnesium ethoxide breaks down. This step results in an intercrystalline mesoporous structure.[180]

6.3.3 Characterization of Materials

The morphology of as-prepared MgO and commercial MgO (purchased from Aldrich) were examined by various techniques. Both samples were characterized by transmission electron microscopy (TEM, JEOL JEM-1230). Powder X-ray diffraction (XRD) patterns were collected using a X-Ray diffractometer with Cu Ka radiation 40 kV and 30 mA. The Brunauer-Emmett-Teller (BET) specific surface area and pore size was measured using a Quantachrome Nova 4200e. Pore size distribution plots for both the MgO nanoparticles were obtained by Barrett-Joyner-Halenda (BJH) method from the adsorption branch of the isotherm. Measurements are reported as averages of multiple measurements. Errors in these measurements represent the standard deviation.
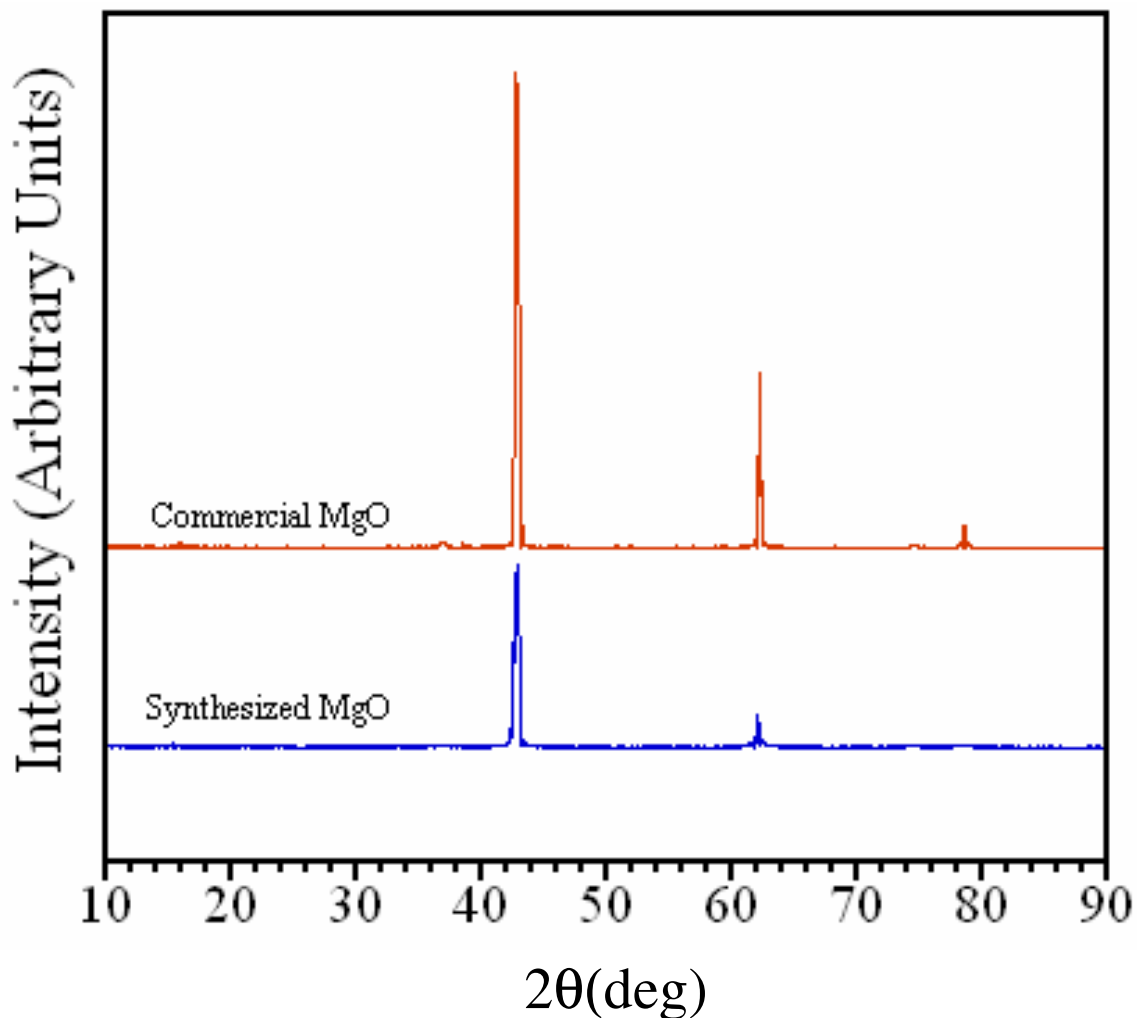
Figure 6.1: XRD pattern of commercial and synthesized MgO samples.

6.3.4 FTIR studies of Carbon Dioxide Adsorption

In situ transmission FTIR spectroscopy was employed to investigate the adsorption of CO_2 on synthesized MgO and commercial MgO. The infrared sample cell and gas handling system used to investigate CO_2 adsorption has been described previously.[52] FTIR spectra were recorded using a single beam Mattson Infinity Gold FTIR spectrometer with a liquid nitrogen-cooled narrow band mercury–cadmium–telluride (MCT) detector.

Table 6.1: Physical properties determined from nitrogen adsorption measurements and transmission electron microscopy for MgO nanomaterials.

Sample	Surface Area (m^2/g)	Size (nm)	Pore Volume[a] (cm^3/g)	Pore Size[b] (nm)
Synthesized MgO	121± 15	9 ± 2	0.373	3.8
Commercial MgO	35± 6	36 ± 10	0.080	1.3

[a] The pore volume of each sample is determined at $P/P_0 = 0.986$.

[b] The pore size is determined by the peak position of the pore size distribution.

Before CO_2 adsorption studies, samples were calcined at 500 °C in oxygen atmosphere for 2 hours to get rid of any impurities. The samples were then pressed onto the tungsten grid and then placed in the infrared sample cell and evacuated overnight under vacuum at room temperature to remove any adsorbed water. CO_2 gas was introduced into the reaction cell through the gas handling system. Two absolute pressure transducers were used to monitor the pressures. MgO sample was exposed to carbon dioxide for around 30 minutes prior to recording a spectrum. Carbon dioxide was then adsorbed at different pressures at room temperature. Each spectrum was obtained by averaging 256 scans at an instrument resolution of 4 cm^{-1}. Each absorbance spectrum shown represents a single beam scan referenced to the MgO sample prior to adsorption.

6.4 Results and Discussion

6.4.1 Characterization of MgO Samples

Figure 6.1 shows the powder XRD patterns of magnesium oxide samples, both commercial and synthesized. The XRD pattern shows two strong peaks at around 42° and 62°, which is the typical pattern of MgO crystal. The strong peaks at around 42° and 62° are assigned to the (200) and (220) reflections of MgO in the cubic rock salt structure JCPDS card no. 75-0447). The XRD data for synthesized MgO shows that it is highly crystalline, and at this temperature, magnesium ethoxide is completely gone and the sample has converted entirely to crystalline MgO.

The size of the nanoparticles as well as the pore structure of MgO samples is examined by TEM. Figure 6.2 shows the TEM images of both the MgO samples. The smaller nanoparticles and detailed pore structure can be observed by using high magnification TEM. The TEM image indicates that MgO is composed of particles with irregular shape. High-magnification TEM image of synthesized MgO reveals the presence of many wormlike pores inside a larger aggregate. The formation of mesopores is due to the aggregation of many small primary MgO nanoparticles with interparticle connections. The primary particle size is determined to be 9 ± 2 nm and 36 ± 10 nm for synthesized and commercial MgO samples respectively, as shown in Figure 6.3. Surface area of both the nanoparticles was analyzed using BET. Synthesized MgO has a BET surface area of 121 ± 15 m^2/g whereas the commercial MgO has a surface area of 35 ± 6 m^2/g. The physical properties of the samples are summarized in Table 6.1.
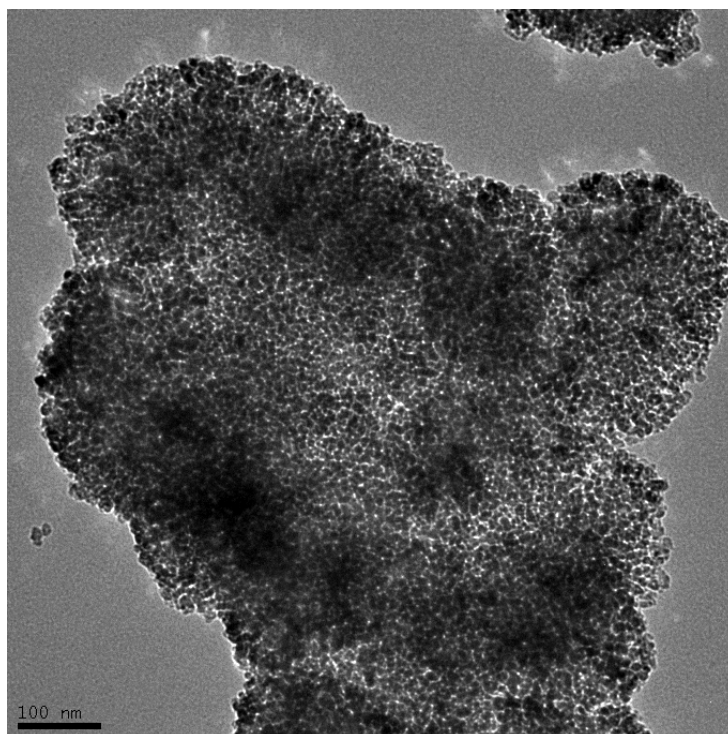
(a)
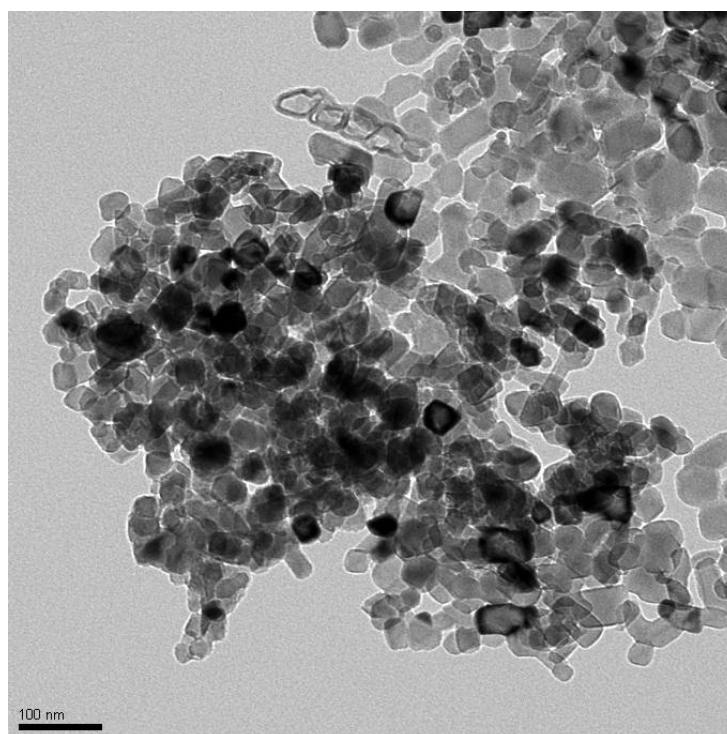
(b)

Figure 6.2: High magnification TEM images of (a) synthesized MgO and (b) commercial MgO.
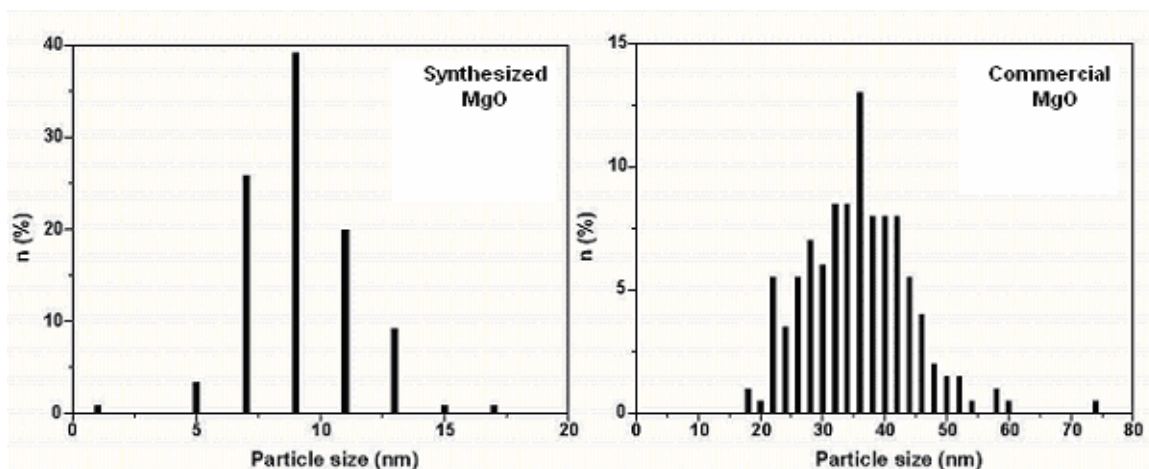
Figure 6.3: Particle size distribution of synthesized MgO and commercial MgO.

To further analyze and quantify the pore structure of the synthesized and commercial MgO sample, nitrogen adsorption-desorption analysis is done. Both samples display type IV isotherms according to the IUPAC, as shown in Figure 6.4. Both the samples are porous, synthesized MgO has a pore volume of 0.373 cm^3/g, and commercial MgO has a pore volume of 0.080 cm^3/g. Figure 6.5 exhibits the pore size distribution of both samples (synthesized and commercial) using the BJH method to the adsorption branch. This yields a pore size of 3.8 and 1.3 nm for synthesized and commercial MgO, respectively. These pore size distributions are narrow and by definition mesoporous in size.

6.4.2 Carbon Dioxide Adsorption on MgO Surfaces

To investigate the potential application of the synthesized MgO for CO_2 adsorption, *in situ* transmission FTIR spectroscopy is used. Figure 6.6 shows FTIR spectra of CO_2 adsorbed on synthesized MgO as a function of CO_2 pressure from 0.26 to

20.2 Torr at 23 $^{\circ}$C. The adsorption of CO_2 on commercial MgO surface was also carried out and is shown in Figure 6.7. The adsorption of the CO_2 on both the surfaces results in
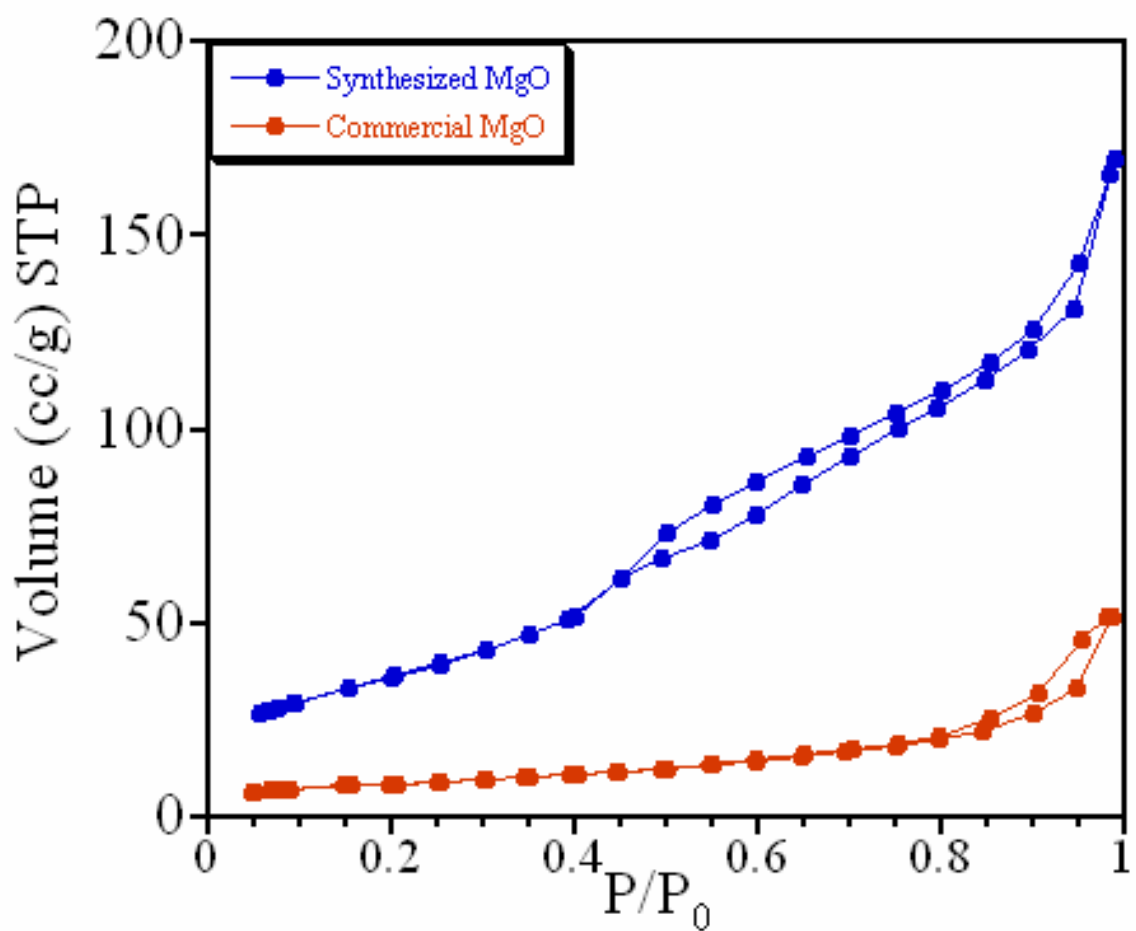
Figure 6.4: Nitrogen adsorption-desorption isotherms for synthesized MgO and commercial MgO.

appearance of a broad feature in the 1000-1800 cm^{-1} region, with similar peaks, and these peaks grow in intensity with increasing CO_2 pressures. The nature of CO_2 adsorption on both the surfaces is discussed below in detail as a comparison.

Figure 6.8, compares the two surfaces for CO_2 adsorption at 1 Torr pressure. The absorption band at 2344 cm^{-1} is observed most notably at high pressure and is due to the formation of linearly adsorbed CO_2.[75, 181] This band as we see in this figure is low in
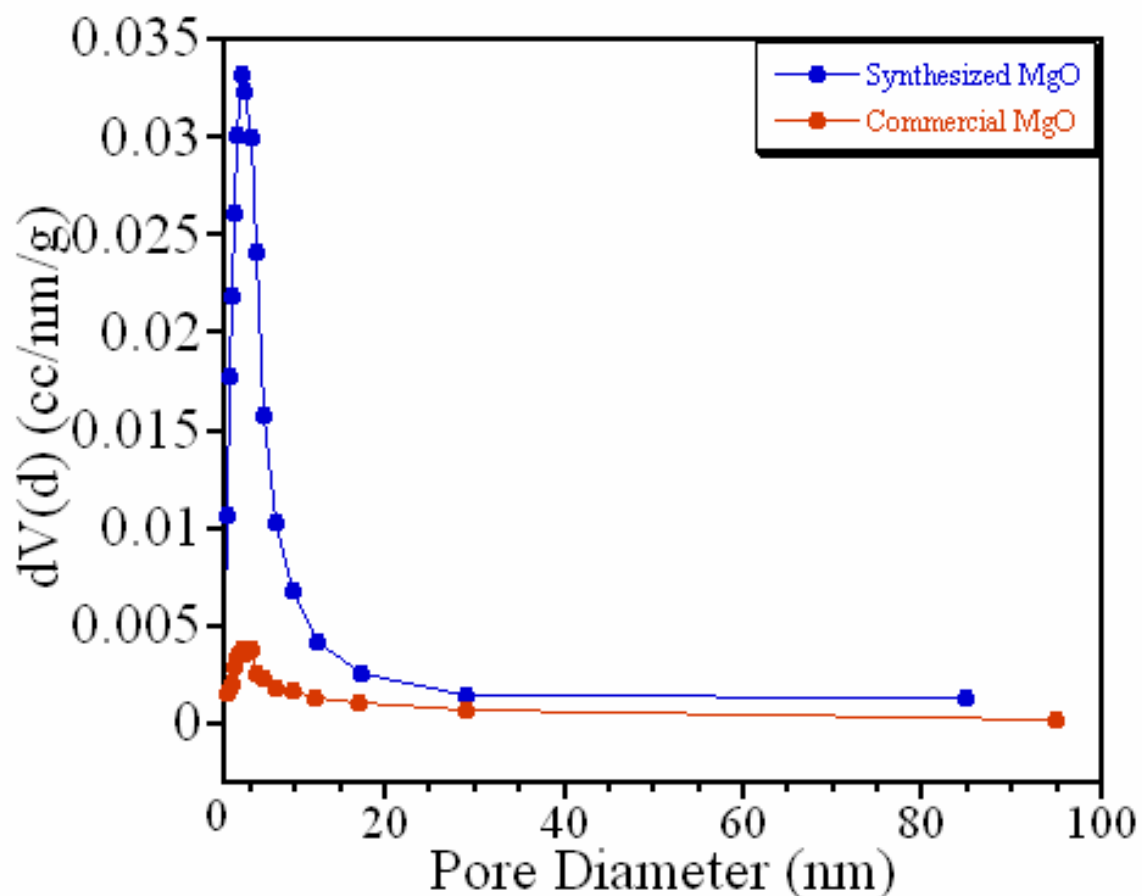
Figure 6.5: Pore size distribution of synthesized MgO and commercial MgO.

intensity and grows in intensity with increasing CO_2 pressures (as shown earlier in Figure 6.7). On looking closely, we observe that more molecular CO_2 can be absorbed on the surface of synthesized MgO as compared to commercial MgO at higher CO_2 pressures.

The absorption bands at 1651, 1406, 1223 and 1028 cm^{-1} are due to the $\nu(OCO)a$, $\nu(OCO)s$, $\delta(COH)$ and $\nu(CO)s$ of bicarbonate, and the bands at 1673, 1556, 1361 and 1091 cm-1 are assigned to the $\nu(OCO)a$, $\nu(OCO)a$, $\nu(OCO)s$ and $\nu(CO)s$ of carbonate
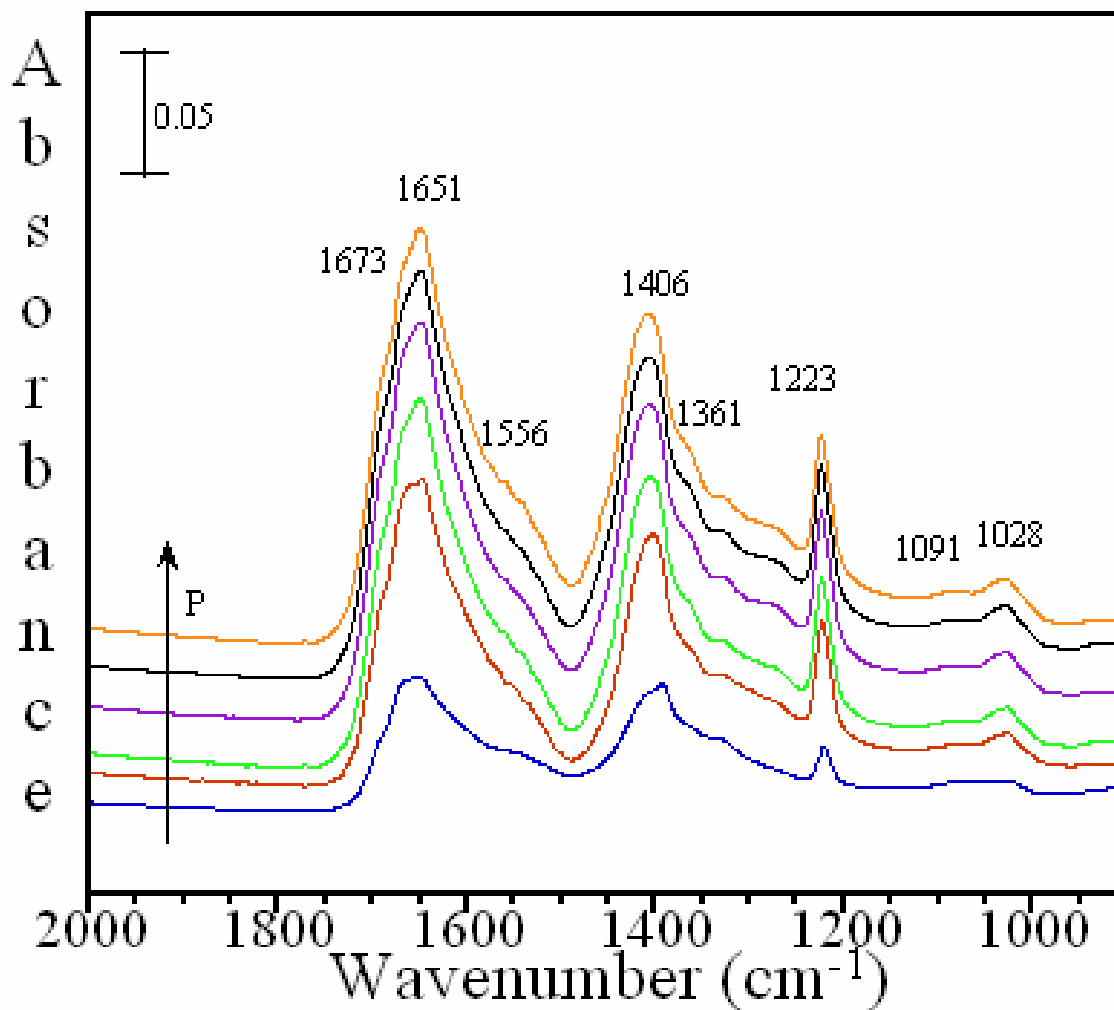
Figure 6.6: Transmission FTIR spectra of adsorbed CO_2, as a function of increasing CO_2 pressure on synthesized MgO (P = 0.264, 0.933, 4.697, 11.2, 15.8 and 20.2 Torr).

species formed on the surface of MgO nanomaterials.[181, 182] All the vibrational

frequencies are summarized in Table 6.2.
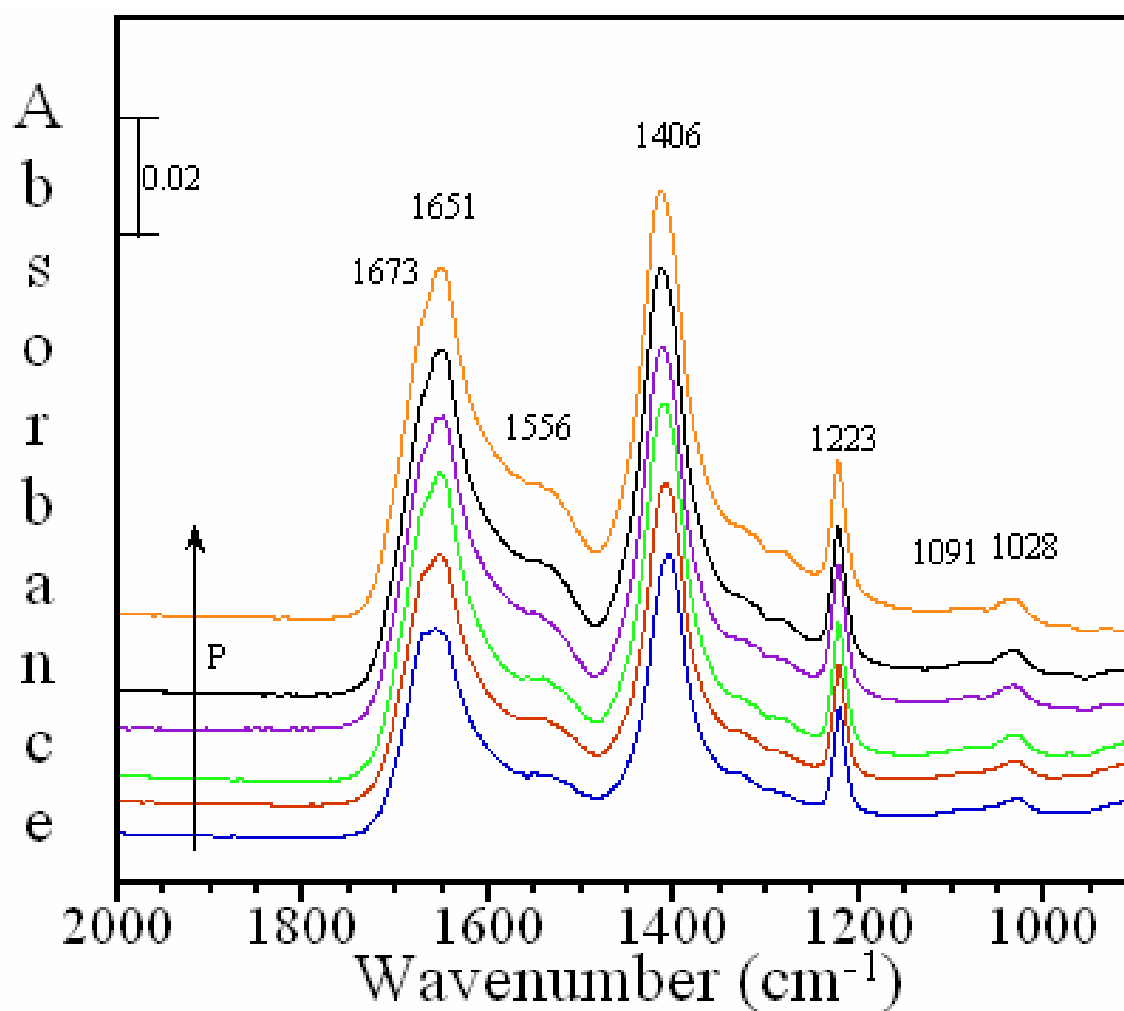
Figure 6.7: Transmission FTIR spectra of adsorbed CO_2 on commercial MgO as a function of CO_2 pressure at room temperature (P = 0.269, 0.939, 4.710, 11.4, 15.8 and 19.7 Torr), under dry conditions.

MgO is known to possess both acidic and basic adsorption sites. In previous

studies, CO_2 has been used as a probe molecule for these sites. Both linearly bonded CO_2

as well as carbonate/bicarbonate species are observed in the spectra of MgO surfaces upon CO_2 adsorption. Bicarbonate species, characterized by the most intense absorption bands at 1651, 1406 and 1223 cm^{-1} forms via the reaction of CO_2 with basic surface hydroxyl groups.[183] On the other hand, carbonate species formation can be of a few types,
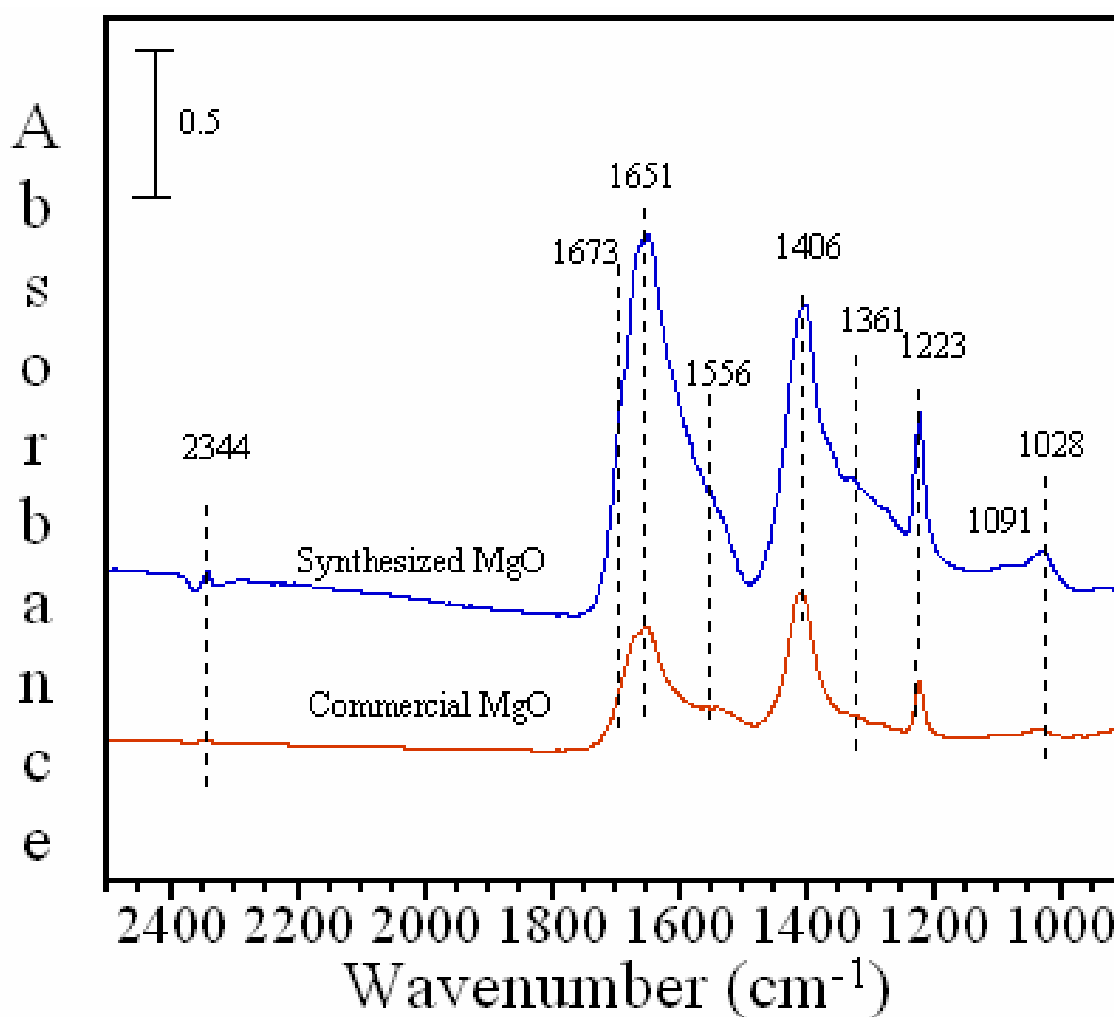
Figure 6.8: FTIR spectra of adsorbed CO_2 on synthesized MgO and commercial MgO at a CO_2 pressure of ~1 Torr and temperature of 296 K. Weight of the samples is normalized to 5 mg.

depending on the acid basic sites present. There can be formation of monodentate, bidentate and bridged carbonate on metal oxide surfaces. On these MgO surfaces we observed the formation of two types of carbonates, monodentate and bidentate. Monodentate carbonate species, commonly observed on metal oxide surfaces exposed to CO_2 has absorption bands at 1510 and 1410 cm^{-1}. These bands are absent or obscured by the more intense bicarbonate and bidentate carbonate bands (*vide infra*). These generally are formed via the interaction of CO_2 molecule with basic surface oxygen sites. In the spectra shown in Figure 6.6, the intense bands at 1556 and 1361 cm^{-1} can be assigned to a bidentate carbonate.[193] Bidentate carbonate has been proposed to form via the interaction of CO_2 with both surface acidic and basic sites. Bridged carbonate species are formed by bonding of CO_2 to two basic sites via formation of bicarbonate followed by bicarbonate deprotonation on nearby basic sites to yield carbonate[106] and are not observed in these experiments.

Comparing both the MgO samples for CO_2 adsorption, in Figure 6.8, we observe distinct absorption bands at 2344, 1673, 1651, 1556, 1406, 1361, 1223, 1091 and 1208 cm^{-1} in the FTIR spectra. In the case of synthesized MgO, with smaller particle size, these bands are much stronger than the corresponding bands in the spectrum of commercial MgO under the same experimental condition for a given mass. It indicates that synthesized MgO has higher activity for CO_2 conversion into bicarbonate/carbonate relative to commercial MgO.

To further justify this conclusion, the integrated areas are compared for the carbonate and bicarbonate absorptions in the spectral range extending from 980 to 1850 cm^{-1}. Figure 6.9 shows the integrated areas of both the surfaces with increasing CO_2

pressures. The increase rate of integrated area is higher at low pressure than that at high pressure. However, for the same sample mass, the integrated area of bicarbonate and carbonate increases faster on synthesized MgO than on the commercial MgO under the same conditions. At a CO_2 pressure of 20.5 Torr, the integrated area of carbonate on synthesized MgO is about 3.2 times larger than on commercial MgO. The higher activity of synthesized MgO is most likely due to the smaller primary MgO nanoparticles and larger surface area. The surface area and particle size of synthesized MgO is 121 ± 15 m^2/g and 9 ± 2 nm. In contrast, the commercial MgO has lower surface area ($35 \pm 6 \ m^2/g$) and larger particle size (36 ± 10 nm). According to the surface area and particle size, we can suggest that synthesized MgO has more active sites for CO_2 adsorption due to the high surface area-to-volume ratio. The higher surface area-to- volume ratio, the higher the efficiency of MgO for CO_2 adsorption, as high surface area-to-volume ratio allows effective utilization of MgO, and conversion to carbonates/ bicarbonates.

On the basis of results from the adsorbed CO_2 on the MgO samples, synthesized MgO with small primary MgO nanoparticle size has high activity for CO_2 adsorption due to increased surface area. To further compare the samples for CO_2 adsorption the ratio of carbonate to bicarbonate absorption band intensities is calculated. The ratio is slightly different for the two samples with, with ratios of 0.49 and 0.45, for synthesized MgO and commercial MgO particles, respectively. This shows an increase in acidic surface sites for the synthesized MgO needed to form surface carbonate. This increase in surface acidity can be associated with an increase in acidic unsaturated surface magnesium sites due to the smaller particle size and/or preparation method. Although the majority of surface sites are basic on both samples, mainly hydroxylated magnesium sites, as inferred

from the major bicarbonate peaks, an increase in carbonate species intensity suggests local disorder in the vicinity of hydroxylated magnesium sites. These differences are important as adsorbed carbonate species, once formed, have been shown to have greater
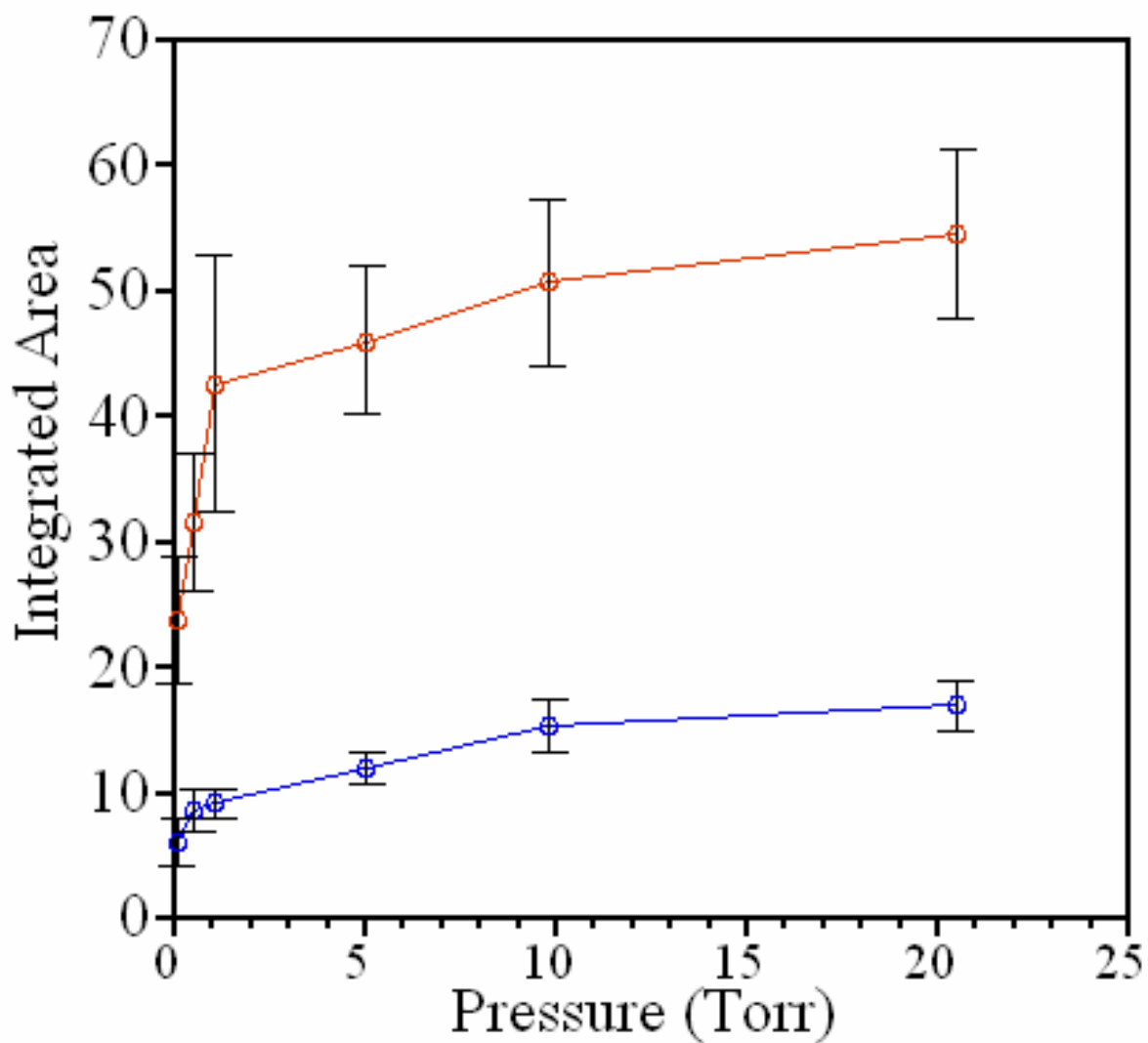
Figure 6.9: Integrated area of carbonate and bicarbonate region of synthesized MgO and commercial MgO as a function of CO_2 pressure. Integrated in the spectral range extending from 980 to 1850 cm^{-1}.
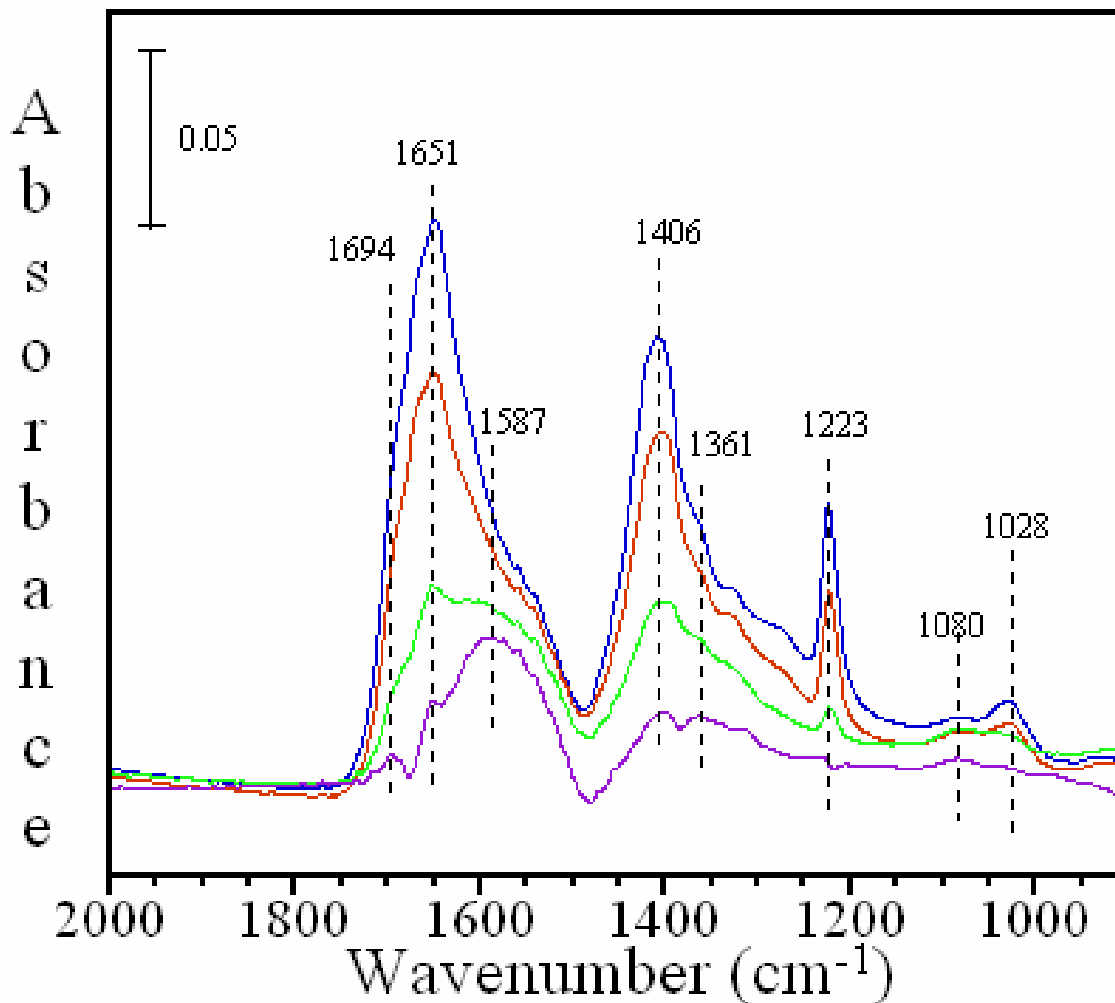
Figure 6.10: Transmission FTIR spectra of evacuation CO_2 adsorbed on synthesized MgO in the spectral range extending from 2000 to 900 cm^{-1}. The losses in the spectra are due to the desorption of bicarbonate species as shown.

stability with evacuation or heating.[106, 184] Changes in surface speciation may indicate differences in the surface sites and structural arrangement of MgO nanoparticles surfaces.

Evacuation experiments, using FTIR spectroscopy, of the MgO surface after the exposure to 1 Torr of CO_2 as a function of time were performed as shown in Figure 6.10. In these experiments the stability of adsorbed surface species is determined. Of all the adsorbed species, adsorbed bicarbonate and linearly adsorbed CO_2 species were found to

be unstable upon evacuation of gas-phase CO_2. The peaks due to adsorbed bicarbonate species, at 1651, 1406, 1223 and 1028 cm^{-1}, decrease significantly in intensity, upon evacuation. The peaks that stay behind in the spectrum are stable and are due to adsorbed carbonate species. This suggests that carbonate species is stable and remains adsorbed on the surface of MgO even upon evacuation for longer time duration. These results are consistent with previous literature observations of CO_2 adsorption on other metal oxides.[106, 121]

Table 6.2: Summary of experimental vibrational frequencies for adsorbed carbonate/ bicarbonate on the MgO surface under dry conditions at $C^{16}O_2$ pressure of 1 Torr.

Adsorbed Species	Vibrational Mode	MgO Frequency (cm^{-1})	Literature Frequency (cm^{-1})[a]
CO_2 linear complex			
	ν_3	2344	2400-2200
Bicarbonate			
	$\nu_1(OH)$	-	3620
	$\nu_2(O\text{-}C\text{-}O)a$	1651	1700-1604
	$\nu_3(O\text{-}C\text{-}O)s$	1406	1480-1383
	$\delta_4(COH)$	1223	1250-1210
	$\nu_5(C\text{-}O)s$	1028	1040
Carbonate			
Monodentate			
	$\nu_1(C\text{-}O)s$	1091	1075-1050
	$\nu_3(O\text{-}C\text{-}O)s$	-	1510-1385
	$\nu_3(O\text{-}C\text{-}O)a$	1556	1590-1510
Bidentate			
	$\nu_1(C\text{-}O)s$	-	1005-950
	$\nu_3(O\text{-}C\text{-}O)s$	1361	1380-1280
	$\nu_3(O\text{-}C\text{-}O)a$	1673	1700-1635

[a] References:[68, 182, 185-190]

6.5 Conclusions

In summary, we have demonstrated that the synthesized MgO with small primary MgO nanoparticles exhibited high adsorption capacity for CO_2 due to its small particle size of the primary MgO nanoparticles and high surface area compared to commercial samples of MgO that contain larger particles.

6.6 Acknowledgements

CHAPTER VII

CONCLUSIONS AND FUTURE DIRECTIONS

7.1 Conclusions

Carbon dioxide storage and conversion are topics of great importance to the scientific community and the public because of the global implications related to climate change, sustainability and energy. There is a great deal of interest in using nanomaterials for the capturing, storage and conversion of carbon dioxide. This chapter discusses briefly the overall trend and reactivity of all the oxide based nanomaterials used in this study towards CO_2 adsorption. On these nanomaterials we see formation of various products such as bicarbonate, carbonate (monodentate, bidentate and bridged) and even carboxylate species (in the case of ZnO).

The different samples were also compared for their adsorption capacity as shown in Figure 7.1 and Figure 7.2. This trend in the CO_2 adsorption capacity of these nanomaterials can be taken in future to predict their reactivity, when these nanomaterials are pretreated under similar conditions.

In Figure 7.1, the adsorption capacity of different nanomaterials is compared, normalized by mass. On comparing the adsorption trend at 10 Torr, we observe that the MgO nanomaterials adsorb the most CO_2 compared to other metal oxides. These nanomaterials are better than other nanomaterials for converting CO_2 to carbonates and bicarbonates. Second to the MgO are the porous nanomaterials, zeolites. Zeolites adsorb CO_2 molecularly and there is a little conversion to carbonate and bicarbonates. These are followed by the alumina nanomaterials and lastly by ZnO. This trend observed for metal

oxides can be explained in terms of their basicity. MgO is more basic than the amphoteric Al_2O_3 and ZnO nanomaterials.
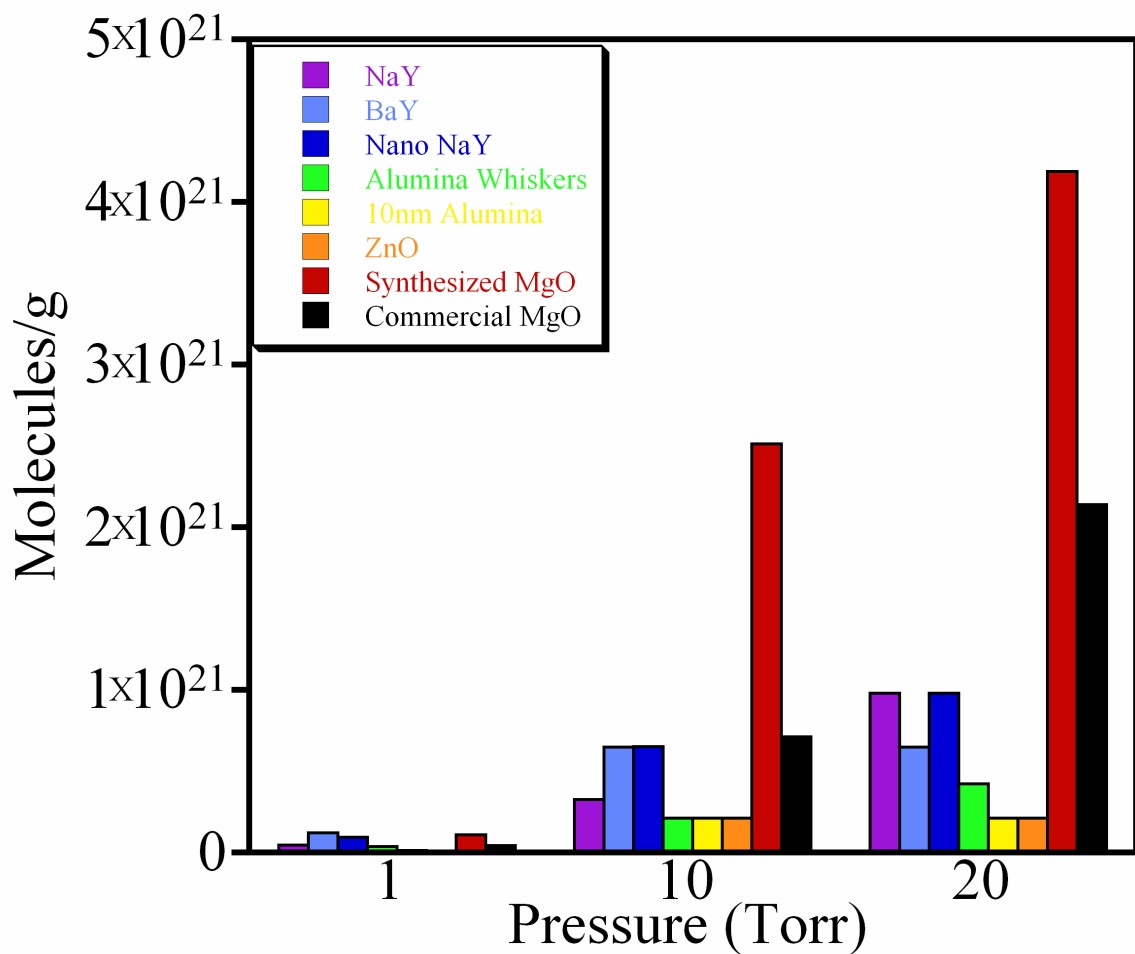
Figure 7.1: Bar graph showing CO_2 adsorption capacity of different oxide based nanomaterials in molecules/g (normalized by mass) at CO_2 pressures of 1, 10 and 20 Torr.

Figure 7.2 shows the trend in adsorption capacity of the nanomaterials normalized to surface area. We observe a similar trend for different metal oxides and zeolites.

Interestingly, now we observe that the at higher CO_2 pressure synthesized MgO falls lower in adsorption capacity than the commercial MgO, which absorbs more CO_2 based on the surface area. Though the overall trend now is slightly changed: MgO > ZnO > Al_2O_3 and the zeolites fall in between. ZnO, with its lower surface area, shows more
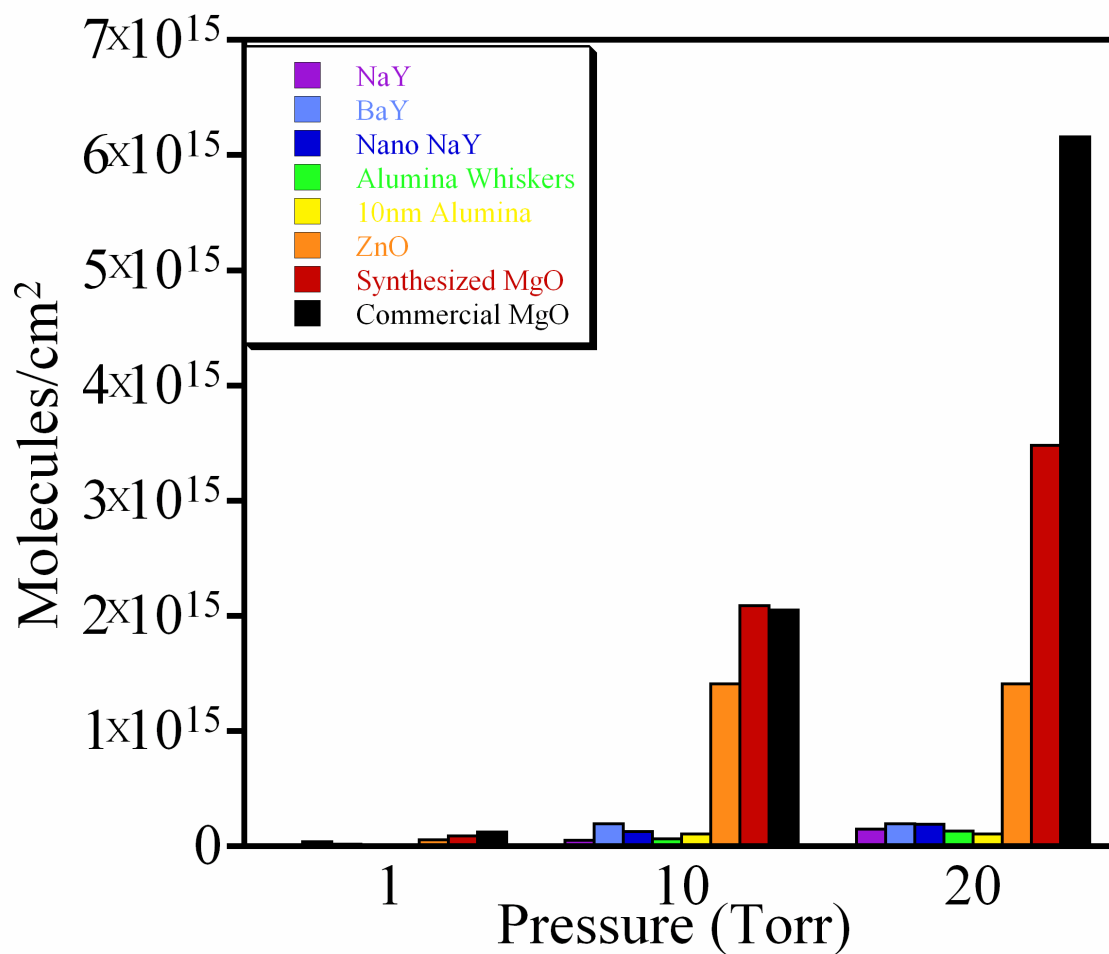
Figure 7.2: Bar graph showing CO_2 adsorption capacity of different nanomaterials (NaY, BaY, nano NaY, alumina whiskers, 10 nm alumina, ZnO, synthesized and commercial MgO) normalized to surface area at three different CO_2 pressures (1, 10 and 20 Torr).

reactivity as compared to alumina nanomaterials and thus distorts the earlier observed order.

Adsorption of CO_2 in the presence of relative humidity was studied in the case of ZnO and zeolite nanomaterials. We observed a slight change in reactivity under wet conditions as compared to dry conditions. In the case of zeolites, for BaY, we saw formation of bicarbonate species when water and CO_2 are co-adsorbed. Formation of bicarbonate and carbonate species was observed under wet conditions for nano NaY. However, for ZnO, under wet conditions only carbonate species was formed, whereas under dry conditions we saw bicarbonate and carboxylate species as well.

7.2 Future Directions

The research conducted so far can serve as a platform for new future directions for this project. Recent studies have shown that there can be enhancement in the adsorption capacity of nanoporous zeolites by functionalizing the structure of zeolites. Literature suggests that modifying the structure of commercial Y zeolite with TEPA (tetraethylenepentamine) resulted in a significant enhancement in CO_2 adsorption capacity.[191] Similarly, it will be interesting to substitute the zeolite framework and study the photocatalytic activity. Previously, such an experiment resulted in formation of CO_2, CH_4 and CH_3OH onto mesoporous silica where a framework substitution by Ti species was made. [192]

In the case of metal oxides, a comparison study of CO_2 adsorption behavior on different aluminum materials (or other metal hydroxides) will be equally interesting. Studying the photocatalytic behavior of ZnO for CO_2 reduction might lead to formation

of interesting new products. For MgO nanomaterials, the adsorption capacity for CO_2 under wet conditions will be another interesting study to conduct. $MgCO_3$ is known to exist in different phases under relative humidity.[193-195] It will therefore be interesting to study co-adsorption of CO_2 and H_2O on these surfaces and to observe a phase change behavior under such experimental conditions.

APPENDIX A

INSTRUMENTAL PARAMETERS, MACRO PROGRAMS AND

CALCULATIONS

A1. Instrumental Parameters for Transmission FT-IR Spectroscopy: Mattson Infinity Gold FTIR Spectrometer

Basic
Sample Scans: 250
Background Scans: 1
Resolution: 4 cm^{-1}
Gain: 1
Moving Mirror
Forward Velocity: 40.0 kHz
Reverse Velocity: 40.0 kHz
Frequency Start: 650 cm^{-1}
Frequency End: 4000 cm^{-1}
Spectral Range: MIR
Laser Samp: 2
Low Pass Filter: Auto
Signal
ADC Sensitivity: Off
ZPD Polarity: Positive
ZPD Threshold: 170Mv
Processing
Zero Fill: 1X
FFT Symmetry: Double
Apodization: Triangle
Phase Correction: Mertz
Phase Apodization: Triangle
Phase Type: Real

A2. Macro Programs

Different type of Macro programs were used to automatically instruct the spectrometer either to continuously collect spectra or to manipulate the data after taking the scans.

A2.1 Macro Program for Automatic Scans

```
For x = 1 to 5000 step 1
begin

sleep 4
Bench:Scan

save
end
```

A2.2. Macro Program for Integrating Specific Regions in the Spectra

```
cd C:\Pragati\8thjune2009
S = findFirstFile "8jun9*.abs"
A = stringLength S
if (A > 0)
{
        while (A > 0)
        {
                B = load S
                A = integrate 1800 980
                save
                S = findNextFile
                A = stringLength S
        }
```

A3. Adsorption Capacity Calculations

Step 1:
Experimental
Initial Pressure (Ip)
Equilibrium Pressure (Ep)
Δp (Exp) (Torr) = Ip – Ep

Step 2:
Blank
Initial Pressure (Ipb)
Equilibrium Pressure (Epb)
Δp (Blank) (Torr) = Ipb – Epb

Step 3:
Δp (Exp) = Ip – Ep
Δp (Blank) = Ip – Ep
$d(\Delta p)$(Torr) = Δp (Blank) - Δp (Exp)

Step 4:
n = (d(Δp).V) / (R.T)
N = n.A

Step 5:
N/cm^2 = Molecules/cm^2 = N / (SA* wt)

Step 6:
N/g = Molecules/g = N/wt

Constants
N = Avagadros Number = 6.02E+23
R = Gas Constant = 62363.67 mLTorrK^{-1}mol^{-1}
V = Volume of cell = 1197 ml
T = Room Temperature = 298 K
wt = Weight of sample, Value taken from Table A.1
SA = Surface area, Value taken from Table A.2

Table A.1: Summary of sample weight taken for each experiment
and surface area of individual samples.

Oxides	Surface Area (cm^2/g)	Sample Weight (g)
NaY	6550000	0.0118
BaY	3320000	0.0119
Nano NaY	5230000	0.0118
Alumina Whiskers	3200000	0.0183
10 nm Alumina	1950000	0.0183
ZnO	150000	0.0183
Synthesized MgO	1210000	0.0046
Commercial MgO	350000	0.0054

Table A.2: Calculations summary for the CO_2 adsorption capacity of individual samples.

Oxides	Ep (Torr)	Δp Exp (Torr)	Δp Blank (Torr)	$d\Delta p$	n	N/cm^2	N/g
NaY							
	0.931	0.269	0.255	0.014	9.01E-07	7.03E+12	4.60E+19
	11.4	2.8	2.7	0.1	6.44E-06	5.02E+13	3.29E+20
	19.5	5.6	5.3	0.3	1.93E-05	1.51E+14	9.86E+20
BaY							
	0.907	0.293	0.255	0.038	2.44E-06	3.73E+13	1.24E+20
	11.3	3.4	3.2	0.2	1.28E-05	1.96E+14	6.52E+20
	19.6	5.5	5.3	0.2	1.28E-05	1.96E+14	6.52E+20
Nano NaY							
	0.916	0.284	0.255	0.029	1.86E-06	1.82E+13	9.53E+19
	11.3	3.4	3.2	0.2	1.28E-05	1.26E+14	6.58E+20
	19.5	5.6	5.3	0.3	1.93E-05	1.89E+14	9.86E+20
Alumina Whiskers							
	0.928	0.272	0.255	0.017	1.09E-06	1.13E+13	3.60E+19
	11.4	3.3	3.2	0.1	6.44E-06	6.62E+13	2.12E+20
	19.6	5.5	5.3	0.2	1.28E-05	1.32E+14	4.24E+20
10 nm Alumina							
	0.939	0.261	0.255	0.006	3.86E-07	6.52E+12	1.27E+19
	11.4	3.3	3.2	0.1	6.44E-06	1.09E+14	2.12E+20
	19.7	5.4	5.3	0.1	6.44E-06	1.09E+14	2.12E+20
ZnO							
	0.941	0.259	0.255	0.004	2.57E-07	5.65E+13	8.48E+18
	11.4	3.3	3.2	0.1	6.44E-06	1.41E+15	2.12E+20
	19.7	5.4	5.3	0.1	6.44E-06	1.41E+15	2.12E+20
Synthesized MgO							
	0.932	0.268	0.255	0.013	8.37E-07	9.06E+13	1.10E+20
	11.2	3.5	3.2	0.3	1.93E-05	2.09E+15	2.53E+21
	20.2	6.1	5.6	0.5	3.22E-05	3.48E+15	4.22E+21
Commercial MgO							
	0.939	0.261	0.255	0.006	3.86E-07	1.23E+14	4.31E+19
	11.4	3.3	3.2	0.1	6.44E-06	2.05E+15	7.18E+20
	19.7	5.6	5.3	0.3	1.93E-05	6.16E+15	2.16E+21

REFERENCES

1.   Houghton, J. T.; Ding, Y.; Griggs, D. J.; Noguer, M.; Van der Linden, P. J.; Dai, X.; Maskell, K.; Johnson, C. A. *Climate Change 2001: The Scientific Basis. Contribution of Working Group I to the Third Assessment Report of the Intergovernmental Panel on Climate Change.*; **2001**.

2.   Fourier, J. B., Memoire sur les temperatures du globe terrestre et des espaces planetaires. *Mémoires de l'Académie Royale des Sciences* **1827,** 7, 569–604.

3.   Mitchell, J. F. B., The greenhouse effect and climate change *Reviews of Geophysics* **1989,** 27 (1), 115–139.

4.   Nordhaus, W. D., A sketch of economics of the greenhouse-effect *American Economic Review* **1991,** 81, (2), 146-150.

5.   Robbins, L. L.; Fabry, V. J., Carbon Dioxide Chemistry: Environmental Issues. In Paul, J., Pradier, C., Eds. ed.; The Royal Society of Chemistry: 1994; p 301–304.

6.   Marquis, M.; Tans, P., Climate change - Carbon crucible. *Science* **2008,** 320, (5875), 460-461.

7.   Luthi, D.; Le Floch, M.; Bereiter, B.; Blunier, T.; Barnola, J. M.; Siegenthaler, U.; Raynaud, D.; Jouzel, J.; Fischer, H.; Kawamura, K.; Stocker, T. F., High-resolution carbon dioxide concentration record 650,000-800,000 years before present. *Nature* **2008,** 453, (7193), 379-382.

8.   Hoch, P. K., Historical studies in the physical and biological sciences-Seidel, RW. *Technology and Culture* **1988,** 18, (1), 991-993.

9.   Rotty, R. M., Past and future emission of CO2. *Cellular and Molecular Life Sciences* **1980,** 36, (7), 781-783.

10.   Tans, P., Monthly Average Carbon Dioxide Concentration. Mauna Loa Observatory. In *NOAA/ESRL (www.esrl.noaa.gov/gmd/ccgg/trends/)*.

11.   Solomon, S.; Qin, D.; Manning, M.; Chen, Z.; Marquis, M.; Averyt, K. B.; Tignor, M. A.; Miller, H. L. *Climate Change 2007: The Physical Science Basis. Contribution of Working Group I to the Fourth Assessment Report of the Intergovernmental Panel on Climate Change.* ; **2007**.

12.   Petit, J. R.; Jouzel, J.; Raynaud, D.; Barkov, N. I.; Barnola, J. M.; Basile, I.; Bender, M.; Chappellaz, J.; Davis, M.; Delaygue, G.; Delmotte, M.; Kotlyakov, V. M.; Legrand, M.; Lipenkov, V. Y.; Lorius, C.; Pepin, L.; Ritz, C.; Saltzman, E.; Stievenard, M., Climate and atmospheric history of the past 420,000 years from the Vostok ice core, Antarctica. *Nature* **1999,** 399, (6735), 429-436.

13.   Scambos, T. A.; Hulbe, C.; Fahnestock, M.; Bohlander, J., The link between climate warming and break-up of ice shelves in the Antarctic Peninsula. *Journal of Glaciology* **2000,** 46, (154), 516-530.

14.   Rothrock, D. A.; Yu, Y.; Maykut, G. A., Thinning of the Arctic sea-ice cover. In *Geophysical Research Letters* **1999**, 26, 3469-3472.

15.   Holloway, G.; Sou, T., Has Arctic sea ice rapidly thinned. *Journal of Climate* **2002,** 15, (13), 1691-1701.

16.   Meehl, G. A.; Washington, W. M.; Collins, W. D.; Arblaster, J. M.; Hu, A. X.; Buja, L. E.; Strand, W. G.; Teng, H. Y., How much more global warming and sea level rise. *Science* **2005,** 307, (5716), 1769-1772.

17.   Archer, D.; Eby, M.; Brovkin, V.; Ridgwell, A.; Cao, L.; Mikolajewicz, U.; Caldeira, K.; Matsumoto, K.; Munhoven, G.; Montenegro, A.; Tokos, K., Atmospheric lifetime of fossil fuel carbon dioxide. *Annual Review of Earth and Planetary Sciences* **2009**, 117-134.

18.   Parry, M. L.; Canziani, O. F.; Palutikof, J. P.; Linden, P. J. V.; Hanson, C. E. *Climate change 2007: Impacts, Adaptation and Vulnerability. Summary for Policymakers. Contribution of Working Group II to the Fourth Assessment Report of the Intergovernmental Panel on Climate Change.*; **2007**.

19.   Seppälä, R.; Buck, A.; Katila, P. *Adaptation of Forests and People to Climate Change.* ; **2009.**

20.   Covert, D. S. a. H., J., Size distributions and chemical properties of aerosol at Ny Ålesund, Svalbard'. *Atmospheric Environment* **1993,** 27, 2989-2997.

21.   Tegen, I.; Lacis, A. A., Modeling of particle size distribution and its influence on the radiative properties of mineral dust aerosol. *Journal geophysical research* **1996,** 101, (19), 237-244.

22.   Whitey, K. T., The physical characteristics of sulfur aerosols. *Atmospheric Environment* **2007,** 41, (1), 25-49.

23.   O'Dowd, C. D.; Aalto, P.; Hmeri, K.; Kulmala, M.; Hoffmann, T., Aerosol formation: Atmospheric particles from organic vapours. . *Nature* **2002,** 416, (6880), 497-498.

24.	Cruz, C. N.; Pandis, S. N., Deliquescence and Hygroscopic Growth of Mixed Inorganicâ Organic Atmospheric Aerosol. *Environmental Science & Technology* **2000,** 34, (20), 4313-4319.

25.	Polissar, A. V.; Paatero, P.; Hopke, P. K.; Malm, W. C.; Sisler, J. F., Atmospheric aerosol over Alaska 2. Elemental composition and sources. *Journal of geophysical research* **1998,** 103, 19045-19057.

26.	Bauer, S. E.; Balkanski, Y.; Schulz, M.; Hauglustaine, D. A.; Dentener, F., Global modeling of heterogeneous chemistry on mineral aerosol surfaces: Influence on tropospheric ozone chemistry and comparison to observations. *Journal of Geophysical Research-Atmospheres* **2004,** 109, (D2).

27.	Tegen, I.; Harrison, S. P.; Kohfeld, K. E.; Engelstaedter, S.; Werner, M., Emission of soil dust aerosol: Anthropogenic contribution and future changes. *Geochica Et Cosmochimica Acta* **2002,** 66, (15A), A766-A766.

28.	Miller, R. L.; Tegen, I., Climate response to soil dust aerosols. *Journal of Climate* **1998,** 11, (12), 3247-3267.

29.	Woodward, S., Modeling the atmospheric life cycle and radiative impact of mineral dust in the Hadley Centre climate model. *Journal of Geophysical Research-Atmospheres* **2001,** 106, (D16), 18155-18166.

30.	Zender, C. S.; Bian, H. S.; Newman, D., Mineral dust entrainment and deposition (DEAD) model: Description and 1990s dust climatology. *Journal of Geophysical Research- Atmospheres* **2003**.

31.	Husar, R. B.; Tratt, D. M.; Schichtel, B. A.; Falke, S. R.; Li, F.; Jaffe, D.; Gasso, S.; Gill, T.; Laulainen, N. S.; Lu, F.; Reheis, M. C.; Chun, Y.; Westphal, D.; Holben, B. N.; Gueymard, C.; McKendry, I.; Kuring, N.; Feldman, G. C.; McClain, C.; Frouin, R. J.; Merrill, J.; DuBois, D.; Vignola, F.; Murayama, T.; Nickovic, S.; Wilson, W. E.; Sassen, K.; Sugimoto, N.; Malm, W. C., Asian dust events of April 1998. *Journal of Geophysical Research-Atmospheres* **2001,** 106, (D16), 18317-18330.

32.	Mahowald, N. M.; Kiehl, L. M., Mineral aerosol and cloud interactions. *Geophysical Research Letters* **2003,** 30, (9).

33.	Shinn, E. A.; Smith, G. W.; Prospero, J. M.; Betzer, P.; Hayes, M. L.; Garrison, V.; Barber, R. T., African dust and the demise of Caribbean coral reefs. *Geophysical Research Letters* **2000,** 27, (19), 3029-3032.

34.	Sokolik, I. N.; Winker, D. M.; Bergametti, G.; Gillette, D. A.; Carmichael, G.; Kaufman, Y. J.; Gomes, L.; Schuetz, L.; Penner, J. E., Introduction to special section: Outstanding problems in quantifying the radiative impacts of mineral dust. *Journal of Geophysical Research- Atmospheres* **2001,** 106, (D16), 18015-18027.

35.   Reid, E. A.; Reid, J. S.; Meier, M. M.; Dunlap, M. R.; Cliff, S. S.; Broumas, A.; Perry, K.; Maring, H., Characterization of African dust transported to Puerto Rico by individual particle and size segregated bulk analysis. *Journal of Geophysical Research-Atmospheres* **2003,** 108, (D19).

36.   Linke, C.; Mohler, O.; Veres, A.; Mohacsi, A.; Bozoki, Z.; Szabo, G.; Schnaiter, M., Optical properties and mineralogical composition of different Saharan mineral dust samples: a laboratory study. *Atmospheric Chemistry and Physics* **2006,** 6, 3315-3323.

37.   Claquin, T.; Schulz, M.; Balkanski, Y. J., Modeling the mineralogy of atmospheric dust sources. *Journal of Geophysical Research-Atmospheres* **1999,** 104, (D18), 22243-22256.

38.   Ma, C. J.; Tohno, S.; Kasahara, M.; Hayakawa, S., Properties of individual Asian dust storm particles collected at Kosan, Korea during ACE-Asia. *Atmospheric Environment* **2004,** 38, (8), 1133-1143.

39.   DeMott, P. J.; Cziczo, D. J.; Prenni, A. J.; Murphy, D. M.; Kreidenweis, S. M.; Thomson, D. S.; Borys, R.; Rogers, D. C., Measurements of the concentration and composition of nuclei for cirrus formation. *Proceedings of the National Academy of Sciences of the United States of America* **2003,** 100, (25), 14655-14660.

40.   Rudich, Y.; Khersonsky, O.; Rosenfeld, D., Treating clouds with a grain of salt. *Geophysical Research Letters* **2002,** 29, (22).

41.   Sokolik, I. N.; Toon, O. B., Incorporation of mineralogical composition into models of the radiative properties of mineral aerosol from UV to IR wavelengths. *Journal of Geophysical Research-Atmospheres* **1999,** 104, (D8), 9423-9444.

42.   Claustre, H.; Morel, A.; Hooker, S. B.; Babin, M.; Antoine, D.; Oubelkheir, K.; Bricaud, A.; Leblanc, K.; Queguiner, B.; Maritorena, S., Is desert dust making oligotrophic waters greener. *Geophysical Research Letters* **2002,** 29, (10).

43.   Usher, C. R.; Michel, A. E.; Grassian, V. H., Reactions on mineral dust. *Chemical Reviews* **2003,** 103, (12), 4883-4939.

44.   Jessop, P. G.; Heldebrant, D. J., Green Biphasic Homogeneous Catalysis. *Environmental Catalysis* **2005**, 627-648.

45.   Bian, H. S.; Zender, C. S., Mineral dust and global tropospheric chemistry: Relative roles of photolysis and heterogeneous uptake. *Journal of Geophysical research-Atmospheres* **2003**.

46.   Tang, E.; Cheng, G.; Ma, X.; Pang, X.; Zhao, Q., Surface modification of zinc oxide nanoparticle by PMAA and its dispersion in aqueous system. *Applied Surface Science* **2006,** 252, (14), 5227-5232.

47.   Larsen, S. C., Nanocrystalline zeolites and zeolite structures: Synthesis, characterization, and applications. *Journal of Physical Chemistry C* **2007,** 111, 18464-18474.

48.   Corma, A., State of the art and future challenges of zeolites as catalysts. *Journal of Catalysis* **2003,** 216, (1-2), 298-312.

49.   Marcus, B. K.; Cormier, W. E., Going green with zeolites. *Chemical Engineering Progress* **1999,** 95, (6), 47-53.

50.   Song, W. G.; Li, G. H.; Grassian, V. H.; Larsen, S. C., Development of improved materials for environmental applications: Nanocrystalline NaY zeolites. *Environmental Science & Technology* **2005,** 39, (5), 1214-1220.

51.   Li, G. H.; Jones, C. A.; Grassian, V. H.; Larsen, S. C., Selective catalytic reduction of NO2 with urea in nanocrystalline NaY zeolite *Journal of Catalysis* **2005,** 235, (2), 431-431.

52.   Li, G. H.; Larsen, S. C.; Grassian, V. H., Catalytic reduction of NO2 in nanocrystalline NaY zeolite. *Journal of Molecular Catalysis a-Chemical* **2005,** 227, (1-2), 25-35.

53.   Henrich, V. E., The surfaces of metal-oxides *Reports on Progress in Physics* **1985**, 1481-1541.

54.   Al-Abadleh, H. A.; Grassian, V. H., Oxide surfaces as environmental interfaces. *Surface Science Reports* **2003,** 52, (3-4), 63-161.

55.   Brown, G. E.; Henrich, V. E.; Casey, W. H.; Clark, D. L.; Eggleston, C.; Felmy, A.; Goodman, D. W.; Gratzel, M.; Maciel, G.; McCarthy, M. I.; Nealson, K. H.; Sverjensky, D. A.; Toney, M. F.; Zachara, J. M., Metal oxide surfaces and their interactions with aqueous solutions and microbial organisms. *Chemical Reviews* **1999,** 99, (1), 77-174.

56.   Finlayson-Pitts, B. J.; Wingen, L. M.; Sumner, A. L.; Syomin, D.; Ramazan, K. A., The heterogeneous hydrolysis of NO2 in laboratory systems and in outdoor and indoor atmospheres: An integrated mechanism. *Physical Chemistry Chemical Physics* **2003,** 5, (2), 223-242.

57.   Walker, J. C. G., The carbon cycle and atmosphere CO2 -Natural variations archean to present Sundquist, ET, Broecker,WS *Science* **1985**, 163-164.

58.   Penkett, S. A., Chemistry of the natural atmosphere -Warneck, P *Nature* **1988**, 322-322.

59.   Martens, W. N.; Frost, R. L.; Bartlett, J.; Kloprogge, J. T., The ageing of alumina hydrolysates synthesized from sec-butoxyaluminium(III). *Journal of Materials Chemistry* **2001,** 11, (6), 1681-1686.

60.   Kloprogge, J. T.; Ruan, H. D.; Frost, R. L., Thermal decomposition of bauxite minerals: infrared emission spectroscopy of gibbsite, boehmite and diaspore. *Journal of Material Science* **2002,** 37, (6), 1121-1129.

61.   Auroux, A.; Gervasini, A., Microcalorimetric study of the acidity and basicity of mteal-oxide surfaces *Journal of Physical Chemistry* **1990,** 94, (16), 6371-6379.

62.   Taravel, B.; Delorme, P.; Chauvet, G.; Lorenzel.V, Theoretical study of planar vibrations of CO3(2-) ions and NO3(-) ions in complex structures with bridged coordination *Journal of Molecular Structure* **1972,** 13, (2), 283.

63.   Busca, G.; Lorenzelli, V., Infrared spectroscopic identification of species arising from reactive adsorption of carbon oxides on metal oxide surfaces. *Materials Chemistry* **1982,** 7, (1), 89-126.

64.   Ferretto, L.; Glisenti, A., Study of the surface acidity of an hematite powder. *Journal of Molecular Catalysis A-Chemical* **2002,** 187, (1), 119-128.

65.   Hoggan, P. E.; Bensitel, M.; Lavalley, J. C., A new method of calculating interactions between adsorbates and metal-oxide surfaces -Application to the study of CO2 insertion in hydroxyl or methoxy groups on Al2O3 AND TiO2. *Journal of Molecular Structure* **1994,** 320, 49-56.

66.   Morterra, C.; Zecchina, A.; Coluccia, S.; Chiorino, A., IR Spectroscopic study of CO2 adsorption onto eta-AL2O3. *Journal of the Chemical Society-Faraday Transactions I* **1977,** 73, 1544-1560.

67.   Ramis, G.; Busca, G.; Lorenzelli, V., Low-temperature CO2 adsorption on metal-oxides.Spectroscopic characterization of some weakly adsorbed species *Materials Chemistry and Physics* **1991,** 29, (1-4), 425-435.

68.   Rethwisch, D. G.; Dumesic, J. A., Effect of metal oxygen bond strength on properties of oxides .1. Infrared-sepctroscopy of adsorbed CO and CO2. *Langmuir* **1986,** 2, (1), 73-79.

69.   Brugger, J.; McPhail, D. C.; Wallace, M.; Waters, J., Formation of willemite in hydrothermal environments. *Economic Geology and the Bulletin of the Scociety of Economic Geologists* **2003,** 98, (4), 819-835.

70.   Wang, Y.; Kovacik, R.; Meyer, B.; Kotsis, K.; Stodt, D.; Staemmler, V.; Qiu, H.; Traeger, F.; Langenberg, D.; Muhler, M.; Woll, C., CO2 activation by ZnO through the formation of an unusual tridentate surface carbonate. *Angewandte Chemie-International Edition* **2007,** 46, (29), 5624-5627.

71.   Yan, C. L.; Xue, D. F., Novel self-assembled MgO nanosheet and its precursors. *Journal of Physical Chemistry B* **2005,** 109, (25), 12358-12361.

72.   Bian, S. W.; Ma, Z.; Cui, Z. M.; Zhang, L. S.; Niu, F.; Song, W. G., Synthesis of micrometer-sized nanostructured magnesium oxide and its high catalytic activity in the Claisen-Schmidt condensation reaction. *Journal of Physical Chemistry C* **2008,** 112, (30), 11340-11344.

73.   Climent, M. J.; Corma, A.; Iborra, S.; Mifsud, M., MgO nanoparticle-based multifunctional catalysts in the cascade reaction allows the green synthesis of anti-inflammatory agents. *Journal of Catalysis* **2007,** 247, (2), 223-230.

74.   Lee, S. C.; Chae, H. J.; Lee, S. J.; Choi, B. Y.; Yi, C. K.; Lee, J. B.; Ryu, C. K.; Kim, J. C., Development of Regenerable MgO-Based Sorbent Promoted with K2CO3 for CO2 Capture at Low Temperatures. *Environmental Science & Technology* **2008,** 42, (8), 2736-2741.

75.   Hu, J.; Zhu, K.; Chen, L.; Kubel, C.; Richards, R., MgO(111) Nanosheets with Unusual Surface Activity. *The Journal of Physical Chemistry C* **2007,** 111, (32), 12038-12044.

76.   Stevens, R. W.; Siriwardane, R. V.; Logan, J., In Situ Fourier Transform Infrared (FTIR) Investigation of CO2 Adsorption onto Zeolite Materials. *Energy Fuels* **2008,** 22 (5), 3070–3079.

77.   Ali, H. M. Laboratory studies of atmospheric particles: heterogeneous reactions and phase transition. University of Iowa, 2005.

78.   Elzey, S. R. Applications and physiochemical characterization of nanomaterials in environmental, health, and safety studies. University of Iowa, 2010.

79.   Elzey, S.; Mubayi, A.; Larsen, S. C.; Grassian, V. H., FTIR study of the selective catalytic reduction of NO2 with ammonia on nanocrystalline NaY and CuY. *Journal of Molecular Catalysis A: Chemical* **2008,** 285, (1-2), 48-57.

80.   Frisch, M. J.; Trucks, G. W.; Schlegel, H. B.; Scuseria, G. E.; Robb, M. A.; Cheeseman, J. R.; Montgomery, J. A.; Vreven, J.; Kudin, K. N.; Burant, J. C.; Millam, J. M.; Iyengar, S. S.; Tomasi, J.; Barone, V.; Mennucci, B.; Cossi, M.; Scalmani, G.; Rega, N.; Petersson, G. A.; Nakatsuji, H.; Hada, M.; Ehara, M.; Toyota, K.; Fukuda, R.; Hasegawa, J.; Ishida, M.; Nakajima, T.; Honda, Y.; Kitao, O.; Nakai, H.; Klene, M.; Li, X.; Knox, J. E.; Hratchian, H. P.; Cross, J. B.; Bakken, V.; Adamo, C.; Jaramillo, J.; Gomperts, R.; Cammi, R.; Stratmann, R. E.; Yazyev, O.; Austin, A. J.; Cammi, R.; Pomelli, C.; Ochterski, J.; Ayala, P. Y.; Morokuma, K.; Voth, G. A.; Salvador, P.; Dannenberg, J. J.; Zakrzewski, V. G.; Dapprich, S.; Daniels, A. D.; Strain, M. C.; Farkas, O.; Malick, D. K.; Rabuck, A. D.; Raghavachari, K.; Foresman, J. B.; Ortiz, J. V.; Cui, Q.; Baboul, A. G.; Clifford, S.; Cioslowski, J.; Stefanov, B. B.; Liu, G.; Liashenko, A.; Piskorz, P.; Komaromi, I.; Martin, R. L.; Fox, D. J.; Keith, T.; Al-Laham, M. A.; Peng, C. Y.; Nanayakkara, A.; Challacombe, M.; Gill, P. M. W.; Johnson, B. G.; Chen, W.; Wong, M. W.; C., G.; Pople, J. A. *Gaussian 03 (Revision C.02),* ; Wallingford, CT, 2004.

81.   Treutler, O.; Ahlrichs, R., Efficient molecular numerical-integration schemes *Journal of Catalysis* **1995,** 102, (1), 346-354.

82.   Becke, A., Density-functional exchnage-energy apporximation with correct asymptotic behavior *Physical Review A* **1988,** 38 (6), 3098-3100.

83.   Becke, A. D., A new mixing of Hartree–Fock and local density functional theories. *Journal of Chemical Physics* **1993,** 98, (2), 1372-1377.

84.   Lee, C.; Yang, W.; Parr, R., Development of Colle-Salvetti correlation-energy into a functional of the electron-density *Physical Review B* **1988,** 37 (2), 785-789.

85.   Schafer, A.; Huber, C.; Ahlrichs, R., Fully optimized contracted gaussian-basis sets of triple zeta valence quality for atoms Li to Kr *Journal of Chemical Physics* **1994,** 100, (8), 5829-5835.

86.   Eichkorn, K.; Weigend, F.; Treutler, O.; Ahlrichs, R., Auxiliary basis sets for main row atoms and transition metals and their use to approximate Coulomb potentials. . *Theoretical Chemistry Accounts* **1997,** 97 (1-4), 119-124.

87.   Sierka, M.; Hogekamp, A.; Ahlrichs, R., Fast evaluation of the Coulomb potential for electron densities using multipole accelerated resolution of identity approximation. . *Journal of Chemical Physics* **2003,** 118, (20), 9136-9148.

88.   Ahlrichs, R.; Bar, M.; Haser, M.; Horn, H.; Kolmel, C., Electronic-structure calculations on workstation computers-the program system turbomole *Chemical Physics Letters* **1989,** 162 (3), 165-169.

89.   http://www.chemcraftprog.com.

90.   Li, G.; Xu, M.; Larsen, S. C.; Grassian, V. H., Photooxidation of cyclohexane and cyclohexene in BaY. *Journal of Molecular Catalysis A: Chemical* **2003,** 194, (1-2), 169-180.

91.   Angell, C. L.; Howell, M. V., Inrared spectroscopic investigations of zeolites and adsorbed molecules .V. Carbon dioxide *Canadian Journal of Chemistry* **1969,** 47, (20), 3831.

92.   Chan, B.; Radom, L., Zeolite-catalyzed hydrogenation of carbon dioxide and ethene. *Journal of the American Chemical Society* **2008,** 130, (30), 9790-9799.

93.   Bonenfant, D.; Kharoune, M.; Niquette, P.; Mimeault, M.; Hausler, R., Advances in principal factors influencing carbon dioxide adsorption on zeolites. *Science and Technology of Advanced Materials* **2008,** 9, (1).

94.   Khelifa, A.; Derriche, Z.; Bengueddach, A., Sorption of carbon dioxide by zeolite X exchanged with Zn2+ and Cu2+. *Microporous and Mesoporous Materials* **1999,** 32, (1-2), 199-209.

95.   Goj, A.; Sholl, D. S.; Akten, E. D.; Kohen, D., Atomistic simulations of CO2 and N-2 adsorption in silica zeolites: The impact of pore size and shape. *Journal of Physical Chemistry B* **2002,** 106, (33), 8367-8375.

96.   Baltrusaitis, J.; Schuttlefield, J.; Jensen, J. H.; Grassian, V. H., FTIR spectroscopy combined with quantum chemical calculations to investigate adsorbed nitrate on aluminium oxide surfaces in the presence and absence of co-adsorbed water. *Physical Chemistry Chemical Physics* **2007,** 9, 4970-4980.

97.   Andersson, M. P.; Blomquist, J.; Uvdal, P., Surface-induced C-O bond anharmonicity of methoxy adsorbed on Cu(100): Experiments and density-functional theory calculations. *Journal of Chemical Physics* **2005,** 123, (22).

98.   Plant, D. F.; Maurin, G.; Deroche, I.; Gaberova, L.; Llewellyn, P. L., CO2 adsorption in alkali cation exchanged Y faujasites: A quantum chemical study compared to experiments. *Chemical Physics Letters* **2006,** 426, (4-6), 387-392.

99.   Plant, D. F.; Maurin, G.; Deroche, I.; Llewellyn, P. L., Investigation of CO2 adsorption in Faujasite systems: Grand Canonical Monte Carlo and molecular dynamics simulations based on a new derived Na+-CO2 force field. *Microporous and Mesoporous Materials* **2007,** 99, (1-2), 70-78.

100.   Ferrari, A. M.; Ugliengo, P.; Garrone, E., Ab initio study of the adducts of carbon monoxide with alkaline cations. *Journal of Chemical Physics* **1996,** 105, (10), 4129-4139.

101.   Baltrusaitis, J.; Schuttlefield, J. D.; Zeitler, E.; Jensen, J. H.; Grassian, V. H., Surface reactions of carbon dioxide at the adsorbed water-oxide interface. *Journal of Physical Chemistry C* **2007,** 111, 14870-14880.

102.   Krishnakumar, V.; Balachandran, V., Analysis of vibrational spectra of 5-fluoro, 5-chloro and 5-bromo-cytosines based on density functional theory calculations *Spectrochimica acta. Part A, Molecular and biomolecular spectroscopy* **2005,** 61, (5), 1001-1006.

103.   Pulay, P.; Fogarasi, G.; Pongor, G.; Boggs, J. E.; Vargha, A., Combination of theoretical abinitio and experimental information to obtain reliable harmonic force constants scaled quantum mechanical (SQM) force-fields for glyoxal, acrolein, butadiene, formaldehyde and ethylene. *Journal of the American Chemical Society* **1983,** 105, (24), 7037-7047.

104.   Yamakita, Y.; Tasumi, M., Vibrational analyses of p-benzoquinodimethane and p-benzoquinone based on Ab-Initio Hartree-Fock and 2nd order Moller-Plesset calculations *Journal of Physical Chemistry* **1995,** 99, (21), 8524-8534.

105.   Sett, P.; Mishra, T.; Chowdhury, J.; Ghosh, M.; Chattopadhyay, S.; Sarkar, S. K.; Mallick, P. K., Vibrational dynamics and structural investigation of 2,2'-dipyridylketone using Raman, IR and UV-visible spectroscopy aided by ab initio and density functional theory calculation. *The Journal of Chemical Physics* **2008,** 128, (14), 144507.

106.   Baltrusaitis, J.; Jensen, J. H.; Grassian, V. H., FTIR Spectroscopy combined with isotope labeling and quantum chemical calculations to investigate adsorbed bicarbonate formation following reaction of carbon dioxide with surface hydroxyl groups on Fe(2)O3 and Al2O3. *Journal of Physical Chemistry B* **2006,** 110, (24), 12005-12016.

107.   Garrone, E.; Bonelli, B.; Lamberti, C.; Civalleri, B.; Rocchia, M.; Roy, P.; Arean, C. O., Coupling of framework modes and adsorbate vibrations for CO2 molecularly adsorbed on alkali ZSM-5 zeolites: Mid- and far-infrared spectroscopy and ab initio modeling. *Journal of Chemical Physics* **2002,** 117, (22), 10274-10282.

108.   Bonelli, B.; Civalleri, B.; Fubini, B.; Ugliengo, P.; Arean, C. O.; Garrone, E., Experimental and quantum chemical studies on the adsorption of carbon dioxide on alkali-metal-exchanged ZSM-5 zeolites. *Journal of Physical Chemistry B* **2000,** 104, (47), 10978-10988.

109.   Casey, W. H., Chemistry of the solod water interface - Processes at the mineral water and particle water interface in natural systems - Stumm ,W. *Nature* **1993,** 363, (6426), 222.

110.   Yang, X. F.; Sun, Z. X.; Wang, D. S.; Forsling, W., Surface acid-base properties and hydration/dehydration mechanisms of aluminum (hydr)oxides. *Journal of Colloid and Interface Science* **2007,** 308, (2), 395-404.

111.   Okada, K.; Hattori, A.; Kameshima, Y.; Yasumori, A.; Das, R. N., Effect of monovalent cation additives on the gamma-Al2O3-to-alpha-Al2O3 phase transition. *Journal of the American Ceramic Society* **2000,** 83, (5), 1233-1236.

112.   Iordan, A.; Zaki, M. I.; Kappenstein, C., Formation of carboxy species at CO/Al2O3 interfaces. Impacts of surface hydroxylation, potassium alkalization and hydrogenation as assessed by in situ FTIR spectroscopy. *Physical Chemistry Chemical Physics* **2004,** 6, (9), 2502-2512.

113.   Wolverton, C.; Hass, K. C., Phase stability and structure of spinel-based transition aluminas. *Physical Review B* **2001,** 6302, (2).

114.   Shek, C. H.; Lai, J. K. L.; Gu, T. S.; Lin, G. M., Transformation evolution and infrared absorption spectra of amorphous and crystalline nano-Al2O3 powders. *Nanostructured Materials* **1997,** 8, (5), 605-610.

115.   Busca, G.; Lorenzelli, V.; Ramis, G.; Escribano, V. S., Chemistry of olefins at metal-oxide surfaces- a tool for surface science investigation of oxide catalysts *Materials chemistry and Physics* **1991,** 29, (1-4), 175-189.

116.   Turek, A. M.; Wachs, I. E.; Decanio, E., Acidic properties of alumina-supported metal-oxide catalysts-an inrared-spectroscopic study *Journal of Physical Chemistry* **1992,** 96, (12), 5000-5007.

117.   Su, C. M.; Suarez, D. L., In situ infrared speciation of absorbed carbonate on aluminum and iron oxide. *Clays and Clay Minerals* **1997,** 45, (6), 814-825.

118.   Martra, G., Lewis acid and base sites at the surface of microcrystalline TiO2 anatase: relationships between surface morphology and chemical behaviour. *Applied Catalysis A-General* **2000,** 200, (1-2), 275-285.

119.   Brintzin, H.; Hester, R. E., Vibrational analysis of some oxyanion-metal complexes *Inorganic Chemistry* **1966,** 5, (6), 980.

120.   Park, H.; Grassian, V. H., Commercially manufactured engineered nanomaterials for environmental and health studies: important insights provided by independent characterization. . *Environmental Toxicology and Chemistry* **2010,** 29, (3), 715–721.

121.   Busca, G.; Lorenzelli, V., Infrared study of CO2 adsorption of CO2 on hematite. *Materials Chemistry* **1980,** 5, (3), 213-224.

122.   Richardson, C. B.; Hightower, R. L., Evaporation of ammonium-nitrate particles *Atmospheric Environment* **1987,** 21, (4), 971-975.

123.   Jickells, T. D.; An, Z. S.; Andersen, K. K.; Baker, A. R.; Bergametti, G.; Brooks, N.; Cao, J. J.; Boyd, P. W.; Duce, R. A.; Hunter, K. A.; Kawahata, H.; Kubilay, N.; laRoche, J.; Liss, P. S.; Mahowald, N.; Prospero, J. M.; Ridgwell, A. J.; Tegen, I.; Torres, R., Global iron connections between desert dust, ocean biogeochemistry, and climate. *Science* **2005,** 308, (5718), 67-71.

124.   Mogili, P. K.; Kleiber, P. D.; Young, M. A.; Grassian, V. H., N2O5 hydrolysis on the components of mineral dust and sea salt aerosol: Comparison study in an environmental aerosol reaction chamber. *Atmospheric Environment* **2006,** 40, (38), 7401-7408.

125.   Mashburn, C. D.; Frinak, E. K.; Tolbert, M. A., Heterogeneous uptake of nitric acid on Na-montmorillonite clay as a function of relative humidity. *Journal of Geophysical Research-Atmospheres* **2006,** 111, (D15).

126.   Goodman, A. L.; Bernard, E. T.; Grassian, V. H., Spectroscopic study of nitric acid and water adsorption on oxide particles: Enhanced nitric acid uptake kinetics in the presence of adsorbed water. *Journal of Physical Chemistry A* **2001,** 105, (26), 6443-6457.

127.   Baraton, M. I.; Chen, X.; Gonsalves, K. E., FTIR study of a nanostructured aluminum nitride powder surface: Determination of the acidic/basic sites by CO, CO2 and acetic acid adsorptions. *Nanostructured Materials* **1997,** 8, (4), 435-445.

128.   Sica, A. M.; Gigola, C. E., Interaction of CO, NO and NO/CO over Pd/gamma-Al2O3 and Pd-WOx/gamma-Al2O3 catalysts. *Applied Catalysis A-General* **2003,** 239, (1-2), 121-139.

129.   Morterra, C.; Emanuel, C.; Cerrato, G.; Magnacca, G., Infrared study of some surface-properties of boehmite (Gamma-AlO2H). *Journal of the Chemical Society-Faraday Transactions* **1992,** 88, (3), 339-348.

130.   Chen, F. R.; Davis, J. G.; Fripiat, J. J., Aluminum coordination and lewis acidity in transition aluminas *Journal of Catalysis* **1992,** 133, (2), 263-278.

131.   Kantschewa, M.; Albano, E. V.; Ertl, G.; Knozinger, H., Infrared and X-ray photoelectron-spectroscopy study of K2CO3/Gamma-Al2O3. *Applied Catalysis* **1983,** 8, (1), 71-84.

132.   Mitchnick, M. A.; Fairhurst, D.; Pinnell, S. R., Microfine zinc oxide (Z-Cote) as a photostable UVA/UVB sunblock agent. *Journal of the American Academy of Dermatology* **1999,** 40, (1), 85-90.

133.   Gal, D.; Hodes, G.; Lincot, D.; Schock, H. W., Electrochemical deposition of zinc oxide films from non-aqueous solution: a new buffer/window process for thin film solar cells. *Thin Solid Films* **2000,** 361-362, 79-83.

134.   Rong, M. Z.; Zhang, M. Q.; Wang, H. B.; Zeng, H. M., Surface modification of magnetic metal nanoparticles through irradiation graft polymerization. *Applied Surface Science* **2000,** 200, (1-4), 76-93.

135.   Pauporté, T.; Lincot, D., Electrodeposition of semiconductors for optoelectronic devices: results on zinc oxide. *Electrochimica Acta* **2000,** 45, (20), 3345-3353.

136.   Pineda, M.; Palacios, J. M.; Alonso, L.; García, E.; Moliner, R., Performance of zinc oxide based sorbents for hot coal gas desulfurization in multicycle tests in a fixed-bed reactor. *Fuel* **2000,** 79, (8), 885-895.

137.   Iwasaki, T.; Satoh, M.; Masuda, T.; Fujita, T., Powder design for UV-attenuating agent with high transparency for visible light *Journal of Materials Science* **2000,** 35, (16), 4025-4029.

138.   Sato, T.; Tanigaki, T.; Suzuki, H.; Saito, Y.; Kido, O.; Kimura, Y.; Kaito, C.; Takeda, A.; Kaneko, S., Structure and optical spectrum of ZnO nanoparticles produced in RF plasma. *Journal of Crystal Growth* **2003,** 255, (3-4), 313-316.

139.   Shi, J.; Cao, Q.; Wei, Y.; Huang, Y., ZnO varistor manufactured by composite nano-additives. *Materials Science and Engineering B* **2003,** 99, (1-3), 344-347.

140.   Wang, Z. L., Zinc oxide nanostructures: growth, properties and applications *Journal of Physics: Condensed Matter* **2004,** 16, (25), R829–R858.

141.   Yang, Y.; Chen, H.; Zhao, B.; Bao, X., Size control of ZnO nanoparticles via thermal decomposition of zinc acetate coated on organic additives. *Journal of Crystal Growth* **2004,** 263, (1-4), 447-453.

142.   Fan, Z.; Lu, J. G., Zinc Oxide Nanostructures: Synthesis and Properties *Journal of Nanoscience and Nanotechnology* **2005,** 5, (10), 1561-1573.

143.   Battez, A. H.; Gonzalez, R.; Viesca, J. L.; Fernandez, J. E.; Fernandez, J. M. D.; Machado, A.; Chou, R.; Riba, J., CuO, ZrO2 and ZnO nanoparticles as antiwear additive in oil lubricants. *Wear* **2008,** 265, (3-4), 422-428.

144.   Turkoglu, M.; Yener, S., Design and in vivo evaluation of ultrafine inorganic-oxide-containing-sunscreen formulations. *International Journal of Cosmetic Science* **2008,** 19, (4), 193 - 201.

145.   Badger, M. R.; Price, G. D., The role of carbonic-anhydrase in photosynthesis *Annual Review of Plant Physiology and Plant Molecular Biology* **1994,** 45, 369-392.

146.   Rombach, M.; Brombacher, H.; Vahrenkamp, H., The insertion of heterocumulenes into Zn-H and Zn-OH bonds of pyrazolylborate-zinc complexes. *European Journal of Inorganic Chemistry* **2002**, (1), 153-159.

147. Loferer, M. J.; Tautermann, C. S.; Loeffler, H. H.; Liedl, K. R., Influence of backbone conformations of human carbonic anhydrase II on carbon dioxide hydration: Hydration pathways and binding of bicarbonate. *Journal of the American Chemical Society* **2003,** 125, (29), 8921-8927.

148. Schroder, D.; Schwarz, H.; Schenk, S.; Anders, E., A gas-phase reaction as a functional model for the activation of carbon dioxide by carbonic anhydrase. *Angewandte Chemie-International Edition* **2003,** 42, (41), 5087-5090.

149. Bottoni, A.; Lanza, C. Z.; Miscione, G. P.; Spinelli, D., New model for a theoretical density functional theory investigation of the mechanism of the carbonic anhydrase: How does the internal bicarbonate rearrangement occur. *Journal of the American Chemical Scociety* **2004,** 126, (5), 1542-1550.

150. Wang, Y. G.; Bronsveld, P. M.; DeHosson, J. T. M.; Djuricic, B.; McGarry, D.; Pickering, S., Ordering of octahedral vacancies in transition aluminas. *Journal of the American Ceramic Society* **1998,** 81, (6), 1655-1660.

151. Taylor, J. H.; Amberg, C. H., Inrared spectra of gases chemisorbed on zinc oxide.1. CO and CO2. *Canadian Journal of Chemistry-Revue Canadienne De Chime* **1961,** 39, (3), 535.

152. Saussey, J.; Lavalley, J. C.; Bovet, C., Infrared study of CO2 adsorption on ZNO - adsorption sites. *Journal of the Chemical Society- Faraday-Transactions I* **1982,** 78, 1457-1463.

153. Boccuzzi, F.; Ghiotti, G.; Chiorino, A., Surface-reactions of CO on a metal-semiconductor sustem - CU/ZNO. *Surface Science* **1985,** 162, (1-3), 361-367.

154. Boccuzzi, F.; Chiorino, A., FTIR study of carbon monoxide oxidation and scrambling at room temperature over copper supported on ZnO and TiO2 .1. *Journal of Physical Chemistry A* **1996,** 100, (9), 3617-3624.

155. Sahibed-Dine, A.; Aboulayt, A.; Bensitel, M.; Saad, A. B. M.; Daturi, M.; Lavalley, J. C., IR study of CS2 adsorption on metal oxides: relation with their surface oxygen basicity and mobility. *Journal of Molecular Catalysis a-Chemical* **2000,** 162, (1-2), 125-134.

156. Szunyogova, E.; Mudronova, D.; Gyoryova, K.; Nemcova, R.; Kovarova, J.; Piknova-Findorakova, L., The physicochemical and biological properties of zinc(II) complexes. *Journal of Thermal analysis and Calorimetry* **2007,** 88, (2), 355-361.

157. Edwards, J. F.; Schrader, G. L., Infreared- spectroscopy of Cu/ZnO catalysts for the water-gas shift reaction and methanol synthesis *Journal of Physical Chemistry A* **1984,** 88, (23), 5620-5624.

158.   Shido, T.; Iwasawa, Y., Reactant-promoted reaction-mechanism for the water-gas shift reaction on ZnO, as the genesis of surface catalysis *Journal of Catalysis* **1991,** 129, (2), 343-355.

159.   Shido, T.; Iwasawa, Y., The effect of coadsorbates in reverse water gas shift reaction on ZnO, in relation to reactant-promoted reaction-mechanism *Journal of Catalysis* **1993,** 140, (2), 575-584.

160.   Chafik, T.; Bianchi, D.; Teichner, S. J., On the mechanism of the methanol synthesis involving a catalyst based on zirconia support *Topics in Catalysis* **1995,** 2, (1-4), 103-116.

161.   Vikulov, K.; Scarano, D.; Zecchina, A.; Coluccia, S., Fourier-transform infrared spectroscopic study of adsorption of ketene on zinc-oxide *Journal of Chemical Society-Faraday Transactions* **1993,** 89, (7), 1127-1129.

162.   Baltrusaitis, J.; Grassian, V. H., Surface reactions of carbon dioxide at the adsorbed water-iron oxide interface. *Journal of Physical Chemistry B* **2005,** 109, (25), 12227-12230.

163.   Baltrusaitis, J.; Grassian, V. H., Carbonic Acid Formation from Reaction of Carbon Dioxide and Water Coordinated to Al(OH)3: A Quantum Chemical Study. *Journal of Physical Chemistry A* **2010,** 114, (6), 2350-2356.

164.   Schuttlefield, J. D. Laboratory studies of atmospheric gases with components of mineral dust aerosol and research in chemical education. University of Iowa, 2008.

165.   Siriwardane, R. V.; Stevens, R. W., Novel Regenerable Magnesium Hydroxide Sorbents for CO2 Capture at Warm Gas Temperatures. *Industrial & Engineering Chemistry Research* **2008,** 48, (4), 2135-2141.

166.   Florin, N. H.; Harris, A. T., Screening CaO-Based sorbents for Co-2 capture in biomass gasifiers. *Energy & Fuels* **2008,** 22, (4), 2734-2742.

167.   Jarvis, K.; Carpenter, R. W.; Windman, T.; Kim, Y.; Nunez, R.; Alawneh, F., Reaction Mechanisms for Enhancing Mineral Sequestration of CO2. *Environmental Science & Technology* **2009,** 43, (16), 6314-6319.

168.   Reddy, E. P.; Smirniotis, P. G., High-Temperature Sorbents for CO2 Made of Alkali Metals Doped on CaO Supports. *The Journal of Physical Chemistry B* **2004,** 108, (23), 7794-7800.

169.   Yamauchi, M.; Ikeda, R.; Kitagawa, H.; Takata, M., Nanosize effects on hydrogen storage in palladium. *Journal of Physical Chemistry C* **2008,** 112, (9), 3294-3299.

170.   Cheon, Y. E.; Suh, M. P., Enhanced Hydrogen Storage by Palladium Nanoparticles Fabricated in a Redox-Active Metal-Organic Framework. *Angewandte Chemie-International Edition* **2009,** 48, (16), 2899-2903.

171.   Shipway, A. N.; Katz, E.; Willner, I., Nanoparticle arrays on surfaces for electronic, optical, and sensor applications. *ChemPhysChem* **2000,** 1, (1), 18-52.

172.   McFarland, A. D.; Van Duyne, R. P., Single silver nanoparticles as real-time optical sensors with zeptomole sensitivity. *Nano Letters* **2003,** 3, (8), 1057-1062.

173.   Haes, A. J.; Zou, S. L.; Schatz, G. C.; Van Duyne, R. P., A nanoscale optical biosensor: The long range distance dependence of the localized surface plasmon resonance of noble metal nanoparticles. *Journal of Physical Chemistry B* **2004,** 108, (1), 109-116.

174.   Haruta, M.; Date, M., Advances in the catalysis of Au nanoparticles. *Applied Catalysis a-General* **2001,** 222, (1-2), 427-437.

175.   Trindade, T.; O'Brien, P.; Pickett, N. L., Nanocrystalline semiconductors: Synthesis, properties, and perspectives. *Chemistry of Materials* **2001,** 13, (11), 3843-3858.

176.   Astruc, D.; Lu, F.; Aranzaes, J. R., Nanoparticles as recyclable catalysts: The frontier between homogeneous and heterogeneous catalysis. *Angewandte Chemie-International Edition* **2005,** 44, (48), 7852-7872.

177.   Grassian, V. H., When Size Really Matters: Size-Dependent Properties and Surface Chemistry of Metal and Metal Oxide Nanoparticles in Gas and Liquid Phase Environments. *Journal of Physical Chemistry C* **2008,** 112, (47), 18303-18313.

178.   Nagappa, B.; Chandrappa, G. T., Mesoporous nanocrystalline magnesium oxide for environmental remediation. *Microporous and Mesoporous Materials* **2007,** 106, (1-3), 212-218.

179.   Bian, S. W.; Baltrusaitis, J.; Galhotra, P.; Grassian, V. H., A Template-Free, Thermal Decomposition Method to Synthesize Mesoporous MgO with a Nanocrystalline Framework and Its Application in Carbon Dioxide Adsorption. *Journal of Materials Chemistry - (In Review)* **2010**.

180.   Yu, C. C.; Zhang, L. X.; Shi, J. L.; Zhao, J. J.; Gao, J. H.; Yan, D. S., A simple template-free strategy to synthesize nanoporous manganese and nickel oxides with narrow pore size distribution, and their electrochemical properties. *Advanced Functional Materials* **2008,** 18, (10), 1544-1554.

181.   Mekhemer, G. A. H.; Halawy, S. A.; Mohamed, M. A.; Zaki, M. I., Qualitative and quantitative assessments of acid and base sites exposed on polycrystalline MgO surfaces: Thermogravimetric, calorimetric, and in-situ FTIR spectroscopic study combination. *Journal of Physical Chemistry B* **2004,** 108, (35), 13379-13386.

182.   Stark, J. V.; Park, D. G.; Lagadic, I.; Klabunde, K. J., Nanoscale metal oxide particles/clusters as chemical reagents. Unique surface chemistry on magnesium oxide as shown by enhanced adsorption of acid gases (sulfur dioxide and carbon dioxide) and pressure dependence. *Chemistry of Materials* **1996,** 8, (8), 1904-1912.

183.   Bian, S. W.; Zhang, Y. L.; Li, H. L.; Yu, Y.; Song, Y. L.; Song, W. G., [gamma]-Alumina with hierarchically ordered mesopore/macropore from dual templates. *Microporous and Mesoporous Materials* 131, (1-3), 289-293.

184.   Menezes, A. O.; Silva, P. S.; Padron Hernandez, E.; Borges, L. E. P.; Fraga, M. A., Tuning Surface Basic Properties of Nanocrystalline MgO by Controlling the Preparation Conditions. *Langmuir* **2009,** 26, (5), 3382-3387.

185.   Fukuda, Y.; Tanabe, K., Infrared Study of Carbon Dioxide Adsorbed on Magnesium and Calcium Oxides. *Bulletin of the Chemical Society of Japan* **1973,** 46, (6), 1616-1619.

186.   Lercher, J. A.; Colombier, C.; Noller, H., Acid–base properties of alumina–magnesia mixed oxides. Part 4.—Infrared study of adsorption of carbon dioxide. *Journal of the Chemical Society, Faraday Transactions 1* **1984,** 80, 949 - 959.

187.   Busca, G.; Lamotte, J.; Lavalley, J. C.; Lorenzelli, V., Ft-Ir Study of the Adsorption and Transformation of Formaldehyde on Oxide Surfaces. *Journal of the American Chemical Society* **1987,** 109, (17), 5197-5202.

188.   Philipp, R.; Fujimoto, K., Ftir Spectroscopic Study of Co2 Adsorption/Desorption on Mgo/Cao Catalysts. *Journal of Physical Chemistry* **1992,** 96, (22), 9035-9038.

189.   Philipp, R.; Omata, K.; Aoki, A.; Fujimoto, K., On the Active-Site of Mgo/Cao Mixed-Oxide for Oxidative Coupling of Methane. *Journal of Catalysis* **1992,** 134, (2), 422-433.

190.   Teramura, K.; Tanaka, T.; Ishikawa, H.; Kohno, Y.; Funabiki, T., Photocatalytic reduction of CO2 to CO in the presence of H-2 or CH4 as a reductant over MgO. *Journal of Physical Chemistry B* **2004,** 108, (1), 346-354.

191.   Su, F.; Lu, C.; Kuo, S.-C.; Zeng, W., Adsorption of CO2 on Amine-Functionalized Y-Type Zeolites. *Energy & Fuels* **2010,** 24, (2), 1441–1448.

192.   Hwang, J. S.; Chang, J. S.; Park, S. E.; Ikeue, K.; Anpo, M., Photoreduction of Carbondioxide on Surface Functionalized Nanoporous Catalysts. . *Topics in Catalysis* **2005,** 35, (3-4), 311-319.

193.   Nashar, B., Barringtonite—a new hydrous magnesium carbonate from Barrington Tops. *Mineralogical Magazine* **1965,** 34, (268), 370-372.

194.   Canterford, J. H.; Tsambourakis, G., Some observations on the properties of dypingite,Mg5(C03)iOH)2 · 5H20, and related minerals. *Mineralogical Magazine* **1984,** 48, 437-442.

195.   Railsback, L., Patterns in the composition, properties and geometry of carbonate minerals. *Carbonates and evaporites* **1999,** 14, (1), 1-20.